Quantum Dynamics of Molecules with Laser as a Catalyst

A thesis submitted during 2025 to the
University of Hyderabad
in partial fulfilment of the award of a Ph.D. degree in
School of Chemistry
by

Md Alamgir
(Reg. No. 18CHPH12)

Under the supervision of

Prof. Susanta Mahapatra

School of Chemistry

University of Hyderabad

Hyderabad – 500 046

India

June-2025

CERTIFICATE

This is to certify that the thesis entitled "**Quantum dynamics of molecules with laser as a catalyst**" submitted by **Md Alamgir** bearing Registration Number **18CHPH12** in partial fulfilment of the requirements for award of Doctor of Philosophy in the School of Chemistry, University of Hyderabad is a bonafide work carried out by him under my supervision and guidance.

This thesis is free from Plagiarism and has not been submitted previously in part or in full to this or any other University or Institution for award of any degree or diploma.

Further, the student has the following publication(s) before submission of the thesis for adjudication and has produced evidence for the same in the form of acceptance letter or the reprint in the relevant area of his research: (Note: At least one publication in referred journal is required)

1. Md Alamgir and S. Mahapatra*, Optimal Control of N-H Photodissociation of Pyridinyl, *J. Chem. Phys.*, **160**, 074303, (2024) , (Chapter 3 in the Ph. D. thesis).
2. Md Alamgir and S. Mahapatra*, Control of optically dark nσ* state mediated photodissociation of thioanisole, *J. Chem. Phys.*, **162**, 154303, (2025) (Chapter 4 in the Ph. D. thesis).

and

has made presentations in the following conferences:

1. Poster presentation in 'DAE Symposium on Current Trends in Theoretical Chemistry (CTTC-2020)', Sep 2021, BARC, Mumbai, India.
2. Poster presentation in '17th Theoretical Chemistry Symposium (TCS-2021)', Dec 2021, IISER Kolkata, India.
3. Oral presentation in '21th Annual In-House Symposium CHEMFEST-2024'.
4. Poster presentation in 'Quantum System in Chemistry, Physics, and Biology (QSCP-XXVI)', Oct 2023, Ashoka University, India.
5. Poster presentation in '18th Theoretical Chemistry Symposium (TCS-2023)', Nov 2023, IIT Madras, India.

Further, the student has passed the following courses towards fulfilment of coursework requirement for Ph.D. / was exempted from doing coursework (recommended by Doctoral Committee) on the basis of the following courses passed during his M.Phil. Program and the M.Phil. Degree was awarded:

Course	Code Name	Credits	Pass/Fail
1. Molecular Spectroscopy	CY453	4	Pass
2. Chemical Binding	CY504	3	Pass
3. Research Proposal	CY801	4	Pass
4. Instrumental Methods A	CY805	4	Pass

Susanta Mahapatra
Senior Professor
School of Chemistry
University of Hyderabad
Hyderabad-500046, TS, India.

Supervisor

Head of the Department

19/6/25

Dean of School

SCHOOL OF CHEMISTRY
University of Hyderabad
Hyderabad-500 046.

DECLARATION

I **Md Alamgir** hereby Declare that this thesis entitled "**Quantum dynamics of molecules with laser as a catalyst**" Submitted by me under the guidance and supervision of **Prof. Susanta Mahapatra** is a bonafide research work. I also declare that it has not been submitted previously in part or in full to this University or any other University or Institution for the award of any degree or diploma. I hereby agree that my thesis can be deposited in Shodhganga/INFLIBNET. A report on plagiarism statistics from the University Librarian is enclosed.

Md. Alamgir

Date: 19. 06. 2025

MD ALAMGIR

Regd. No.:18CHPH12

Thesis Title: **Quantum dynamics of molecules with laser as a catalyst**

Student Regd. No.: **18CHPH12**
Supervisor: **Prof. Susanta Mahapatra**
School: **School of Chemistry**

The research presented in this thesis aligns with the **Sustainable Development Goals (SDGs)**, with primary focus on **SDG-9: Industry, Innovation, and Infrastructure**.

My research, deeply rooted in optimal control theory (OCT), particularly its emphasis on fostering innovation and enabling sustainable industrialization. By employing a Genetic Algorithm (GA) to control the photodissociation of polyatomic molecules like pyridinyl radical and thioanisole, constrained by the time-dependent Schrödinger equation, I am developing advanced mathematical and computational techniques to precisely manipulate quantum dynamics. This innovative approach allows for the maximization of desired outcomes, such as photodissociation yields or the controlled lifetime of specific molecular states. This fundamental scientific innovation is critical because it lays the groundwork for developing more efficient and environmentally sound industrial processes in the future, for instance, by enabling light-driven chemical reactions or the creation of materials with tailored properties. Thus, my work builds essential knowledge infrastructure, paving the way for the sustainable and technologically advanced industries crucial for global progress. This thesis, through its meticulous quantum control calculations on the photodissociation of pyridinyl radical and thioanisole, directly contributes to SDG-9: Industry, Innovation, and Infrastructure, primarily by bolstering the "Innovation" component and laying foundational scientific groundwork for future sustainable industries. The exploration of pyridinyl radical's N-H photodissociation, particularly its role as an intermediate in pyridine-catalyzed water splitting for hydrogen production and its potential in CO_2 reduction, directly aligns with the SDG's objective of promoting sustainable industrialization by offering pathways to cleaner energy and carbon utilization technologies. Similarly, the study of thioanisole's methyl photodissociation, given its importance in drug development, hints at future innovations in the pharmaceutical industry, potentially leading to more efficient, selective, and environmentally sound synthetic routes, thereby contributing to inclusive and sustainable industrialization. Beyond these specific applications, the very nature of the research – employing sophisticated methodologies like OCT and GA optimization to design and predict the effects of precisely tailored, chirped laser pulses – significantly enhances scientific research and technological capabilities. The detailed analysis of molecular dynamics at the quantum level, along with the development of techniques to suppress dissociation or guide reaction pathways, represents a fundamental advancement in chemical control. The assertion that the calculated laser pulses are "experimentally feasible given the present state of technology" underscores the practical relevance of this theoretical work, bridging the gap between abstract scientific inquiry and potential real-world technological implementation. This type of deep, fundamental research is crucial for the long-term upgrading of industrial processes, fostering a culture of innovation, and ultimately supporting the development of a resilient and technologically advanced infrastructure, which are all central to the goal.

ACKNOWLEDGMENTS

First of all, I am grateful to my supervisor, Prof. Susanta Mahapatra, for his constant guidance throughout my PhD days and for his hospitality. I am thankful to him in many ways, but one specific thing I have to confess that he believed me during the time when I was going through the toughest situation of my academic carrier. I also acknowledge him for his help in my research, writing the manuscripts, teaching me quantum chemistry and so on.

I thank the present and former Deans, School of chemistry for their support and giving the wonderful environment in the department during the span of PhD. I am also grateful to my doctoral committee members, Prof. D. Barik and Prof. K. V. Jovan Jose for their insightful suggestions. I would like to thank Prof. K. D. Sen for his support in many of my academic matters. Overall, I am thankful to all the faculty members of school of chemistry and special thanks to Prof. S. K. Das and Prof. V. Baskar for their research related discussion.

I am equally grateful to the chemistry department, University of Calcutta (Rajabazar Science college campus), and all the professors for teaching me chemistry in my M.Sc. degree. A special thanks to Prof. K. Bhattacharya, Prof. Swapan Chakrabarti, Prof. S. Chakravarti, Prof. Debasis Mukhopadhyay, Prof. Chaitali Mukhopadhyay, Prof. Pinaki Chaudhury, and my M.Sc. project guide Prof. Nikhil Guchhait. I would like to thank Prof. Sarika Maitra (NCL Pune), Prof. R. R. Sarkar (NCL Pune), Prof. P. K. Madhu (TIFR Hyderabad), Prof. Jagannath Mondal (TIFR Hyderabad).

I am thankful to the Chemistry department of Barasat Govt. College for teaching me the

chemistry during B.Sc. From the bottom of my heart, I am grateful to Prof. Naba Kumar Bera for teaching me physical chemistry, quantum chemistry in my graduation days and for inspiring me throughout those three years. I am also thankful to all the other professors, especially Prof. P. K. Sen, Prof. Sanjukta Muhuri.

I am indebted to those teachers who taught me in my school (Dattapukur Mahesh Vidyapith). I thank Susanta sir, Giri sir, (Late) S. N. Banik for teaching me, inspiring me. I am also thankful to all of my private tutors during my Board Exam (Sajal Da, Pronab Da, Susanta sir, Raja Da, Apu Kaku, Titu Da, Tuhin Da, Mihir Da) and in my childhood (my mother, Rebeka Fumma and Taslima Vabi).

My deepest thanks go to Ajay Rawat. He was more than just a senior lab mate; he was a true friend. His constant support, through both difficult and happy times at HCU, has been invaluable. I thank also to my another lab mate M. Rani for being always available to have tea with me and sharing lots of gossips. Without you the last couple of years in HCU would be very boring and lonely. I am very much thankful to all of my lab mates, Y. Ajay, Jansi, Shavez, Daradi, Nitai Da, Jayakrushna, Arun Da, Sreyans and all of my seniors from the lab, Dr. Sugata Goswami, Dr. Krishna Reddy, Dr. Rudraditya Sarkar, Dr. Arpita Ghosh, Prof. Rajagopal Rao. Other than my lab mates, I would like to thank all of my HCU friends, Suaman Mondal, Shubham, Soutrik, Sumanta, soumen, Anupam, Somnath, Sarada, Pritam, Sneha Banarjee, Shampita, Shyam, Satyam, Sridatri, Somdatta, Olivia, Sebanti, Arghya, Joydev, and all seniors, Moumita Di, Prachi Di, Kuntal Da, Debika Di, Arijit Da, Pabitra Da, Shubha Da, Shenha Di, Apurba Da, Tansim Di, Arijit Da (Shaoo sir lab), Alim Da, Saddam Da, Taher Da, Nurul Da, Sritam Da, Sudipta Da, and all juniors, Debu, Arunava, Avijit, Rounak, Maynak, Koushik, Soumok, Akshat, Sampurna, Sougata, Shubham, Arka, Sourav Jana, Golu Bhai, Somratan, Poushali, Koushik, Mafi, Sohel, Dipanjan, Supriya, Samapti, Atryee, Nisha, all the friends from Science college, Dibbo, Pushpendu, Soumya, Aritra, Satarupa, Sukanya, Bilkis, Ankita, Supriya Shaw, Riya, Koustav, Tathagata, Mandira. I also thank all the seniors from NCL Pune, Ujjwal Da, Aniruddha DA, Saikat DA, Manoj Da,

Atryee Di, Sayantan Da, and from TIFR, Sourav DasAdhikari, Sourav Bhakta, Avinash, George, and friends from Barasat Govt. College, Subhadeep, Shahid, Kinsuk, Debottom, Piyali, Joydeep, Subarna,

I would like to thank Rima for her love and care to me and being more than a friend to me. It is hard to express how I feel about Rima. Thank you for being with me and without you my story of my life would not be colorful.

My family, I am grateful to my parents, my brother, my sister for their love, mental support and always standing beside me. It is very hard to express my feelings in words about my family, without them I am incomplete. I indebted all my cousin brothers and sisters for their care form me. I would like to thank all the friends from my home place, Sourav Dhara, Sanoyar, Imtiaz, Toni, Roni for being part of my life.

I would like to acknowledge the funding agencies, CSIR for my Doctoral fellowship and DST-SERB for the grand during my PhD and CMSD and Translational facility UPE-II for computational facility.

Lastly, I would like to acknowledge the Almighty, the Merciful, for everything.

This thesis is dedicated to my family.

Abbreviations

BO Born-Oppenheimer

KE Kinetic Energy

PE Potential Energy

PES Potential Energy Surface

ADT Adiabatic to Diabatic Transformation

TDSE Time Dependent Schrödinger Equation

TISE Time Independent Schrödinger Equation

GP Geometric Phase

GA Genetic Algorithm

CG Conjugate Gradient

SO Split-Operator

TDM Transition Dipole Moment

FCS Fluorescence Correlation Spectroscopy

NACT Nonadiabatic Coupling Term

OCT Optimal Control Theory

IVR Intramolecular Vibrational Redistribution

MCTDH Multi-Configuration Time-Dependent Hartree

MRCI Multireference Configuration Interaction

CASSCF Complete Active Space Self-Consistent Field

CASPT2 Complete Active Space Second-Order Perturbation Theory

BCH Baker-Campbell-Hausdorff

FFT Fast Fourier Transformation

UV Ultra-Violet

FC Franck-Condon

IC Internal Conversion

WP Wave Packet

OCT-MCTDH Optimal Control Theory-Multi-Configuration Time-Dependent Hartree

Table of Contents

List of Tables

List of Figures

CHAPTER 1

Introduction

Quantum mechanics has revolutionized our understanding of the physical world, enabling the development of groundbreaking technologies such as quantum computing, quantum communication, and precision sensing. Beyond these technological applications, it has also transformed the way we understand and manipulate chemical reactions at the molecular level. A key aspect of utilizing quantum principles in chemistry lies in the ability to precisely control the behavior of quantum systems that govern reaction dynamics.

Quantum control in the context of chemical reactions focuses on steering reaction pathways and influencing outcomes by manipulating molecular interactions with external fields, such as lasers or electromagnetic fields. This control enables chemists to selectively break and form bonds, optimize reaction yields, and explore reaction mechanisms that are otherwise inaccessible. However, the complexity of molecular quantum states, coupled with challenges such as decoherence and the sensitivity of quantum systems to environmental noise, makes achieving precise control a formidable task. The ability to control chemical reactions has far-reaching implications, including the development of energy-efficient catalytic processes, novel materials, and even the manipulation of biomolecular systems for therapeutic applications. This thesis explores laser-driven control of molecular reactions,

addressing the theoretical and experimental challenges of designing robust control strategies to achieve desired reaction outcomes.

The discovery of the laser in 1960 marked a pivotal moment in science, opening up a new era in molecular spectroscopy and revolutionizing our understanding of molecular systems. Its precision and versatility have led to groundbreaking advancements, particularly in Raman spectroscopy, fluorescence correlation spectroscopy (FCS), and the study of molecular dynamics. Techniques such as optical trapping have enabled the manipulation of individual molecules or atoms, providing unprecedented insights into their behavior. Beyond its contributions to spectroscopy and molecular dynamics, the laser has emerged as a powerful tool for controlling chemical reactions. By tailoring laser pulses to selectively excite molecular vibrations or manipulate electronic states, scientists can steer reaction pathways with remarkable precision. This has profound implications for fields ranging from material synthesis to biological processes, allowing for the design of reactions that are energy-efficient, selective, and scalable.

Quantum control of chemical reactions can be simply described as the selective breaking of a specific chemical bond using an optical laser pulse, even in the presence of competing bonds that could also break. According to experimental findings by Crim et. al., exciting the $4\nu_{OH}$ (third O–H stretching overtone) of HOD and subsequently photolysis with 239.5 or 266 nm photon generates at least 15 times more OD than OH product and the bimolecular reaction, H+HOD $\rightarrow$ OD + H_2, becomes two times more efficient when the same excitation of HOD is applied [1, 2]. The limitation of this simple method stems from intramolecular vibrational redistribution (IVR), where energy disperses among various vibrational modes, resulting in a loss of selectivity [3, 4, 5, 6]. This occurs because the degrees of freedom in a polyatomic molecule are interdependent. As a result, the local vibrational mode is not an eigenstate of the system's Hamiltonian but is instead coupled to other bonds. Consequently, exciting this mode generates a diffused wave packet (WP) that spreads across these coupled modes, leading to IVR.

The quantum mechanical processes are inherently wave phenomena, subject to constructive and destructive interferences. Utilizing this interference phenomena the quantum state can be precisely manipulated, which is commonly referred to as coherent control. Laser pulses serve as an indispensable tool for implementing coherent control. By regulating parameters such as intensity, frequency, phase, polarization, spectral content, and time profile, it is possible to actively shape the interference patterns of quantum states, which is often termed as active control[7]. Mathematically, this translates into the optimization of the laser pulse properties with a motivation of achieving a target state guided by the time dependent Schrödinger equation (TDSE) and it is known as optimal control theory (OCT).

In the 1980s, the introduction of femtosecond laser pulses and the subsequent development of programmable laser pulse technologies [8, 9] enabled the proposal of many control schemes to manipulate molecular dynamics through the coherent properties of lasers. Brumer and Shapiro theoretically demonstrated that coherent control could be achieved by simultaneously exciting molecules through one- and three-photon processes, creating constructive and destructive interference between reaction pathways. This interference could be regulated by adjusting the relative phases of the laser pulses [10, 11, 12]. This theoretical framework was experimentally validated by Chen et al. and Park et al. in 1990 and 1991, respectively [13, 14]. Around the same time, Tannor et al. proposed that coherent control could also be achieved through a pump-dump pulse scheme, which they demonstrated theoretically [15, 16]. Advances in laser technologies subsequently enabled the experimental realization of this scheme by several groups [17, 18, 19, 20]. These two schemes are relatively simple where only one parameter, such as the relative phases of the multiple pulses or the time delay between the pump-dump pulses are optimized. However, for more complex systems where the modes of vibration are interdependent this one parameter optimization is not sufficient to achieve the target product or state. Thus, the design of the laser pulse is critical: the amplitudes of the different interfering vibrational modes must add up in a particular bond at a specific time after photoabsorption to cause its breakage[21]. To

determine this kind of laser pulses by the optimization of multiple parameters OCT has been used [22, 23, 24].

A general paradigm for employing theory to design an optimal laser pulse involves three steps

(1) Construction of the molecular Hamiltonian: The system Hamiltonian is composed of two components kinetic energy and potential energy. The kinetic energy is straightforward to calculate based on the system's geometry, while the potential energy is derived from electronic structure calculations. Additional molecular properties, such as dipole moment and polarizability, are required to determine the interaction energy between the laser and the molecule.

(2) Performing an appropriate calculation to achieve the desired target using TDSE as the governing dynamical constraint enabling the design of the optimal laser pulse.

(3) The optimal laser pulse design is then sent to the laboratory for implementation on the actual sample.

Although, in principle, the OCT can be applied on any kind of complex systems to shape up the optimal design of laser pulse, the computational cost becomes extremely high as the complexity of the system increases. Therefore, nowadays in experimental optimal control this paradigm is not followed, rather the closed-loop laboratory learning control is generally employed [25, 26, 27, 28, 29, 30, 31, 32, 33, 34, 35, 36, 37] which circumvents the theoretical calculations [38]. The close-loop quantum control is itself a generic method [39] which is also a suitable protocol to control the physical properties of larger systems such as biomolecules [40] and photodrugs [41].

What is the significance of OCT? Looking toward its future role, a key factor is the advancement of experimental capabilities in optimal control, particularly for conducting high-duty-cycle experiments. The primary challenge in experimental performance stems from the nature of the cost function that guides the learning algorithm.[42, 43, 44] This is because the experimental cost function has to be comprised of directly observable quantities.

It should provide adequate information to steer the experiments toward the target. At the same time, it must account for and manage competing processes that could pose obstacles to achieving the desired outcome. Therefore, optimal control calculations can give a proper cost function considering all possible physical processes during the dynamics. Theoretical calculations can offer valuable insights and justification for the mechanisms during the progression toward the target.

1.1 Thesis overview

In Chapter 3, a genetic algorithm (GA)-based quantum control study has been conducted on the N-H photodissociation of the pyridynyl radical. To investigate this, we used a three-state model (ground, $\pi\pi^*$, and $\pi\sigma^*$ states) with three modes: N-H stretching, out-of-plane bending of the H atom (b_1), and the Q_9 (a_2) normal mode. The quantum dynamics in this model were controlled by determining the optimal laser pulse to maximize the photodissociation yield, using the TDSE as the dynamic constraint. For the N-H photodissociation, the $\pi\sigma^*$ asymptote is found to be the only active channel after nonadiabatic transition at $\pi\pi$*/$\pi\sigma$* conical intersection (CI) when the optimal laser pulse excites the molecules to $\pi\pi$* state.

In Chapter 4, a quantum control study on the methyl photodissociation of thioanisole is performed. This study employed a three-state model (ground, $\pi\sigma^*$, and nσ^* states) with two vibrational modes: S-CH_3 stretching and methyl group rotation around the S-Ph bond. Using a GA-based optimal control protocol, an optimal laser pulse was designed to maximize the photodissociation yield. The approach prioritized promoting the nonadiabatic transition through the $\pi\pi^*/n\sigma^*$ CI along the S-CH_3 stretching coordinate over the transition via the rotational coordinate, which would otherwise lead to dissociation along the ground-state asymptote or relaxation to the ground-state equilibrium.

The Chapter 5 extends the work od chapter 3, employing a linearly chirped laser pulse

to control the N-H photodissociation dynamics. In this approach, the lifetime of the $\pi\pi^*$ state is maximized while minimizing dissociation through the $\pi\sigma^*$ state. The cost functional is designed with two components: the first ensures the maximization of the overlap between the $\pi\pi^*$ WP and a target vibrational wave function, while the second minimizes the flux associated with dissociation. Using a GA-based optimal control protocol, the optimal laser pulse was determined to be a downwardly chirped pulse, which effectively creates a "reflectron" state in the $\pi\pi^*$ potential, prolonging its lifetime during the dynamics.

CHAPTER 2

Theory and Methodology

2.1 Theory of molecular electronic structure

First of all, let us define a molecule which consists of some electrons of mass m and some atomic nuclei of mass M_i. The charge of each electron is e and the atomic number of i-th nucleus is Z_i. Considering the center of mass of the system as the origin, all the electronic coordinates are set to be **r** (i.e. $\mathbf{r} \equiv r_{e,i}, i = 1, 2, 3....$) and all the nuclear coordinates are set to be **R** (i.e. $\mathbf{R} \equiv R_{n,i}, i = 1, 2, 3....$).

Let us consider a bound, continuous, appropriately differentiable, and quadratically-integrable function of the dynamical variables **r** and **R**, $\Psi(\mathbf{r}, \mathbf{R})$, which is the eigenfunction of the molecular Hamiltonian, $H(\mathbf{r}, \mathbf{R})$. If the corresponding eigenvalue is E, then the eigenvalue equation can be expressed as follows

$$H(\mathbf{r}, \mathbf{R})\Psi(\mathbf{r}, \mathbf{R}) = E\Psi(\mathbf{r}, \mathbf{R}), \tag{2.1}$$

where the eigenvalue, E, represents the total energy of the molecule and it is also function of **r** and **R**, i.e. $E \equiv E(\mathbf{r}, \mathbf{R})$. The above equation is the so-called time independent

Schrödinger equation (TISE).

The full molecular Hamiltonian reads as,

$$H(\mathbf{r}, \mathbf{R}) = T_e + V_{ee}(\mathbf{r}) + T_n + V_{nn}(\mathbf{R}) + V_{en}(\mathbf{r}, \mathbf{R}), \tag{2.2}$$

where, the five terms namely are, electron kinetic energy (KE), electron-electron potential energy (PE), nuclear KE, nuclear-nuclear PE and electron-nuclear PE.

2.1.1 Adiabatic approximation

Adiabatic approximation[45] states that, since mass of the nucleus is much higher than the electron, the motion of nucleus is very slower compared to electron and, consequently, the electrons instantaneously readjust themselves to small change in the nuclear position. In other words, the electronic state remains nearly unchanged due to infinitesimal change in nuclear position. Imposing this approximation, the basis of the TISE (Eq. 2.1), $\Psi(\mathbf{r}, \mathbf{R})$, can be characterized as:

(1) A full set of orthonormal electronic functions, denoted as $\{|\psi_\alpha(\mathbf{r}; \mathbf{R})\rangle\}$, exists. Each of these functions is well-behaved, meaning it is bound, appropriately differentiable, quadratically-integrable, and continuous. They depend on both the dynamical electronic coordinates **r** and, parametrically, on the nuclear coordinates **R** (the semicolon in ψ specifically indicates this parametric dependence).

(2) There exists another distinct complete set of orthonormal nuclear functions, $\{|\chi_{\alpha k}(\mathbf{R})\rangle\}$ for each of the aforementioned electronic function $|\psi_\alpha(\mathbf{r}; \mathbf{R})\rangle$. These nuclear functions are also bound, appropriately differentiable, quadratically-integrable, and continuous function of the dynamical nuclear coordinates **R**.

(3) The adiabatic approximation is characterized by using the complete set of orthonormal functions denoted as $\{|\psi_\alpha(\mathbf{r}; \mathbf{R})\chi_{\alpha k}(\mathbf{R})\rangle\}$.

These conditions are the basic requirements for a 'physically admissible' quantum

mechanical wave function. To ensure the quadratic integrability of the wave functions few additional conditions has to be imposed:

$$\begin{aligned}
\{||\psi_\alpha(\mathbf{r};\mathbf{R})\chi_{\alpha k}(\mathbf{R})\rangle|\} &< \infty, \qquad \{\mathbf{r}\},\{\mathbf{R}\} \in \{\mathbf{r}_b,\mathbf{R}_b\},\\
\{|\nabla_e|\psi_\alpha(\mathbf{r};\mathbf{R})\chi_{\alpha k}(\mathbf{R})\rangle|\} &< \infty, \qquad \{\mathbf{r}\},\{\mathbf{R}\} \in \{\mathbf{r}_b,\mathbf{R}_b\},\\
\{|\nabla_n|\psi_\alpha(\mathbf{r};\mathbf{R})\chi_{\alpha k}(\mathbf{R})\rangle|\} &< \infty, \qquad \{\mathbf{r}\},\{\mathbf{R}\} \in \{\mathbf{r}_b,\mathbf{R}_b\},
\end{aligned} \tag{2.3}$$

and otherwise zero. Here, $\{\mathbf{r}_b,\mathbf{R}_b\}$ are the boundaries of the dynamical variables $\mathbf{r}$ and $\mathbf{R}$. Now the total wave function $\Psi(\mathbf{r},\mathbf{R})$ can be written as a linear combination of $\psi_\alpha(\mathbf{r};\mathbf{R})$

$$\Psi(\mathbf{r},\mathbf{R}) = \sum_{\alpha,k} |\chi_{\alpha k}(\mathbf{R})\psi_\alpha(\mathbf{r};\mathbf{R})\rangle. \tag{2.4}$$

Now the total Hamiltonian can be rewritten in terms of such adiabatic basis as follows (coordinate dependencies henceforth being left implicit to facilitate typographical compactness)

$$\begin{aligned}
&\sum_{\alpha,\beta,j,k} |\chi_{\beta j}\psi_\beta\rangle\langle\chi_{\beta j}\psi_\beta|H|\chi_{\alpha k}\psi_\alpha\rangle\langle\chi_{\alpha k}\psi_\alpha| = \sum_{\alpha,\beta,j,k} |\chi_{\beta j}\psi_\beta\rangle\\
&\times \langle\chi_{\beta j}\psi_\beta|\Big[H_e + T_n\Big]|\chi_{\alpha k}\psi_\alpha\rangle\langle\chi_{\alpha k}\psi_\alpha|,
\end{aligned} \tag{2.5}$$

where

$$\begin{aligned}
H_e \equiv H_e(\mathbf{r};\mathbf{R}) &= T_e + V_{ee} + V_{en} + V_{nn}\\
&= -\sum_i \frac{\hbar^2\nabla_{e,i}^2}{2m_e} + \sum_{j>i}\frac{e^2}{|r_{e,i}-r_{e,j}|} - \sum_{ij}\frac{Z_j e^2}{|r_{e,i}-R_{n,j}|} + \sum_{j>i}\frac{Z_i Z_j e^2}{|R_{n,i}-R_{n,j}|}
\end{aligned} \tag{2.6}$$

is the electronic Hamiltonian which is dependent on the nuclear coordinates, $\mathbf{R}$, parametrically. The first term is the total KE of all the electrons at a certain nuclear configuration.

The other three terms represents the electron-electron repulsion, electron-nucleus attraction, and nucleus-nucleus repulsion energies, respectively. The term T_n in Eq. 2.5 represents the KE contribution from the nuclear motion and it is expressed as

$$T_n = -\sum_i \frac{\hbar^2 \nabla_{n,i}^2}{2M_i} \tag{2.7}$$

where M_i is the mass of the ith nucleus. The electronic functions $\{|\psi_\alpha(\mathbf{r};\mathbf{R})\rangle\}$ are the eigen functions of $H_e(\mathbf{r};\mathbf{R})$ with eigenvalues $U_\alpha^{AA}(\mathbf{r};\mathbf{R})$. Imposing "$AA$" notation for the "adiabatic approximation" to the Eq. 2.5

$$\begin{aligned}\sum_{\alpha,\beta,j,k} |\chi_{\beta j}^{AA}\psi_\beta^{AA}\rangle\langle\chi_{\beta j}^{AA}\psi_\beta^{AA}|H^{AA}|\chi_{\alpha k}^{AA}\psi_\alpha^{AA}\rangle\langle\chi_{\alpha k}^{AA}\psi_\alpha^{AA}| = \sum_{\alpha,\beta,j,k} |\chi_{\beta j}^{AA}\psi_\beta^{AA}\rangle \\ \times \langle\chi_{\beta j}^{AA}\psi_\beta^{AA}|\Big[H_e^{AA} + T_n\Big]|\chi_{\alpha k}^{AA}\psi_\alpha^{AA}\rangle\langle\chi_{\alpha k}^{AA}\psi_\alpha^{AA}|.\end{aligned} \tag{2.8}$$

In the L.H.S.

$$\langle\chi_{\beta j}^{AA}\psi_\beta^{AA}|H^{AA}|\chi_{\alpha k}^{AA}\psi_\alpha^{AA}\rangle = E_{\alpha k}^{AA}\delta_{\alpha\beta}\delta_{jk}. \tag{2.9}$$

In the R.H.S.

$$\langle\psi_\beta^{AA}|H_e^{AA}|\psi_\alpha^{AA}\rangle = U_\alpha^{AA}\delta_{\alpha\beta}, \tag{2.10}$$

the eigenvalues U_α^{AA} are the so-called adiabatic electronic energy eigenvalues which dependent on the nuclear coordinates parametrically. The electronic adiabatic potential energy surfaces (PESs) are these eigenvalues at different nuclear configurations. To satisfy Eq. 2.9, these eigenvalues has to obey the following relation

$$\langle\chi_{\alpha j}^{AA}|T_n + U_\alpha^{AA}|\chi_{\alpha k}\rangle = E_{\alpha k}^{AA}\delta_{jk}, \tag{2.11}$$

which is the TISE to obtain the vibrational eigenvalues and eigenfunctions associated with the adiabatic PESs of electronic states.

Born-Oppenheimer approximation

Born-Oppenheimer (BO) approximation[46, 47] states that the mass of the proton and essentially the nuclei are several times heavier than the electrons, therefore, the nuclei move so slowly compared to the electrons that the nuclei remain almost static with respect to electrons. Consequently, the contribution of the nuclear KE in the electronic energy adiabatic energy will be zero. Under this approximation the Eq. 2.10 can be rewritten as follows

$$\langle \psi_{\beta}^{BO} | H_e | \psi_{\alpha}^{BO} \rangle = U_{\alpha}^{BO} \delta_{\alpha\beta}, \tag{2.12}$$

the eigenvalue U_{α}^{BO} being the nuclear coordinate dependent electronic energy, the BO nuclear energy eigenfunctions can be determined as

$$\langle \chi_{\alpha j}^{BO} | T_n + U_{\alpha}^{BO} | \chi_{\alpha k} \rangle = E_{\alpha k}^{BO} \delta_{jk}. \tag{2.13}$$

$E_{\alpha k}^{BO}$ represents the total adiabatic energies of the molecular system in the BO approximation.

So, considering Eq. 2.13 and 2.12, the total adiabatic molecular TISE can be expressed as

$$\langle \psi_{\beta}^{BO} \chi_{\beta j}^{BO} | H_e + T_n | \psi_{\alpha}^{BO} \chi_{\alpha k}^{BO} \rangle = E_{\alpha k}^{BO} \delta_{\alpha\beta} \delta_{jk}. \tag{2.14}$$

After substituting the momentum operator in the coordinate representation in the Eq. 2.7 the nuclear KE, $T_n = -\sum_i \frac{\hbar^2 \nabla_{n,i}^2}{2M_i}$. The Eq. 2.14 is simplified as follows (see APPENDIX-A)

$$\begin{aligned} &\langle \psi_{\beta}^{BO} \chi_{\beta j}^{BO} | H_e | \psi_{\alpha}^{BO} \chi_{\alpha k}^{BO} \rangle + \delta_{\alpha\beta} \langle \chi_{\beta j}^{BO} | T_n | \chi_{\alpha k}^{BO} \rangle \\ &+ 2 \langle \chi_{\beta j}^{BO} | \sum_i \frac{-\hbar^2}{2M_i} d_i^{\beta\alpha} \cdot \nabla_{n,i} | \chi_{\alpha k}^{BO} \rangle + \langle \chi_{\beta j}^{BO} | \sum_i \frac{-\hbar^2}{2M_i} D_i^{\beta\alpha} | \chi_{\alpha k}^{BO} \rangle = E_{\alpha k}^{BO} \delta_{\alpha\beta} \delta_{jk}, \end{aligned} \tag{2.15}$$

where, the derivative coupling, $d_i^{\beta\alpha}$, and scalar coupling, $D_i^{\beta\alpha}$ is defined as

$$\begin{aligned} d_i^{\beta\alpha} &= \langle \psi_\beta^{BO} | \nabla_{n,i} | \psi_\alpha^{BO} \rangle \\ D_i^{\beta\alpha} &= \langle \psi_\beta^{BO} | \nabla_{n,i}^2 | \psi_\alpha^{BO} \rangle. \end{aligned} \tag{2.16}$$

According to the BO approximation the last two terms in Eq. 2.15 are so small compared to the adiabatic total electronic energy that it can be neglected. A qualitative justification can be given by choosing a small parameter ξ, which is defined as

$$\xi = (m_e/M)^{\frac{1}{4}}. \tag{2.17}$$

where M being a typical nuclear mass and m_e being the mass of electron, which is taken to be unity. For a general molecular systems, for instance, a diatomic molecule which is vibrating near minimum, the internuclear separation is expressed as

$$R = R_0 + \xi u, \tag{2.18}$$

where the reduced distance u is of the order of unity i.e. same as R_0.[48] With these facts, it can be shown that the derivative and scalar coupling terms of Eq. 2.15 are proportional to ξ^3 and ξ^4. If we consider mass of nucleus M is of the order of $10^4 m_e$, then ξ will be of the order of 0.1. The electronic energy correction from the scalar coupling term, $d_i^{\alpha\alpha}$, will be of the order of 10^4, which is also of the order of rotational energy (rotational energy $\propto \frac{1}{MR_0^2} \propto \xi^4$). The off-diagonal terms of the derivative and scalar coupling represents the mixing of two electronic states, α and β. Mixing of two electronic states are proportional to the squares of the two terms, i.e. ξ^6 and ξ^8, respectively. So the correction from the derivative and scalar coupling terms to the electronic energy (or more specifically electronic PES) is so small in general that it can be neglected without loosing any substantial information except some special cases like, construction of a PES for the quantum dynamics calculation of reactive

scattering in the ultra-cold region where the diatomic rotation plays an important role [49], a region of PES where it gets energetically very close another excited state [50], so on.

2.1.2 Nonadiabatic effects

Nonadiabatic effects are incorporated in the electronic energy calculation or more specifically electronic PES construction by the aforementioned two terms which is neglected in the BO approximation. Those two terms are referred to as nonadiabatic coupling terms (NACTs) which are essentially associated with multiple electronic states. In other words the NACTs couple multiple electronic states through nuclear motions. This effect of the electronic states on the other electronic states despite of no apparent interactions, i.e. no energetically closeness, between them is purely a quantum phenomenon. In order to reckon this fact, let us rewrite the Eq. 2.15

$$\Big\{U_{\alpha}^{BO} + T_n - E_{\alpha k}^{BO}\Big\}|\chi_{\alpha k}^{BO}\rangle = -\sum_{\beta}\Big\{\sum_{i}\frac{-\hbar^2}{2M_i}\Big(2d_i^{\beta\alpha}\cdot\nabla_{n,i} + D_i^{\beta\alpha}\Big)\Big\}|\chi_{\beta k}^{BO}\rangle, \quad (2.19)$$

where the right hand side of the equation represents a summation over all the electronic states which indicates that all the electronic states are dependent on all other states through nonadiabatic coupling. The term, U_{α}^{BO} comes from the first term, $\langle\psi_{\beta}^{BO}\chi_{\beta j}^{BO}|H_e|\psi_{\alpha}^{BO}\chi_{\alpha k}^{BO}\rangle$ in Eq. 2.15.

Since the right hand side of Eq. 2.19 is a small quantity, it can be considered as perturbation to the following eigenvalue equation[51]

$$\Big\{E_{\alpha}^{e} + T_n\Big\}|\chi_{\alpha k}^{0}\rangle = E_{\alpha k}^{0}|\chi_{\alpha k}^{0}\rangle. \quad (2.20)$$

Here, $E_{\alpha}^{e} = U_{\alpha}^{BO}$ is the adiabatic PE of α^{th} electronic state and it is defined by equation: $H_e|\psi_{\alpha}^{BO}\rangle = E_{\alpha}^{e}|\psi_{\alpha}^{BO}\rangle$. The terms $E_{\alpha k}^{0}$ and $|\chi_{\alpha k}^{0}\rangle$, represent the eigenenergy and eigenfunction, respectively, of k^{th} vibrational level associated with the corresponding adiabatic

potential of the α^{th} electronic state.

2.1.3 Diabatic representation

There are some basic difficulties to perform any quantum dynamical calculation within adiabatic representation due to the presence of the two derivative coupling terms in the Hamiltonian. Let us apply the Hellmann-Feynman theorem to the derivative coupling term presented in Eq. 2.16

$$d_i^{\beta\alpha} = \frac{\langle \psi_\beta^{BO} | \nabla_{n,i} H_e | \psi_\alpha^{BO} \rangle}{E_\beta^e - E_\alpha^e}. \tag{2.21}$$

The equation indicates that the derivative coupling diverges to infinity when electronic states become degenerate in configuration space. Consequently, the wave function also exhibits singularity at the point of degeneracy, violating fundamental postulates of quantum mechanics. Moreover, adiabatic PES can not be expressed by analytical function because of the presence of singularity and changing character of electronic state at the point of degeneracy.

The total wave function in the diabatic representation is written as

$$\Psi^{DA}(\mathbf{r}, \mathbf{R}) = \sum_{\alpha,k} |\chi_{\alpha k}^{DA}(\mathbf{R}) \psi_\alpha^{DA}(\mathbf{r}; \mathbf{R}_0)\rangle, \tag{2.22}$$

where $\mathbf{R}_0$ represents the reference nuclear geometry and $\psi_\alpha^{DA}(\mathbf{r}; \mathbf{R}_0)$ is the electronic wave function at the reference geometry. Now the electronic Schrödinger equation in the diabatic basis can be expressed as

$$\langle \psi_\beta^{DA}(\mathbf{r}; \mathbf{R}_0) | H_e(\mathbf{r}; \mathbf{R}_0) | \psi_\alpha^{DA}(\mathbf{r}; \mathbf{R}_0) \rangle = U_\alpha^{DA}(\mathbf{r}; \mathbf{R}_0) \delta_{\alpha\beta}, \tag{2.23}$$

where $U_\alpha^{(0)}(\mathbf{r}; \mathbf{R}_0)$ is the diabatic electronic energy at the reference geometry. In the

diabatic representation the equation 2.14 reads as

$$\langle \psi_\beta^{DA} \chi_{\beta j}^{DA} | H_e + T_n | \psi_\alpha^{DA} \chi_{\alpha k}^{DA} \rangle = E_{\alpha k}^{DA} \delta_{\alpha\beta} \delta_{jk}. \tag{2.24}$$

This equation is simplified into

$$H_{\alpha\beta}\delta_{ij} + \langle \chi_{\beta j} | T_n | \chi_{\alpha i} \rangle \delta_{\alpha\beta} = E_{\alpha\beta}^{DA} \delta_{\alpha\beta} \delta_{ij} \tag{2.25}$$

where

$$H_{\alpha\beta} = \langle \psi_\beta^{DA}(\mathbf{r}; \mathbf{R}_0) | H_e(\mathbf{r}; \mathbf{R}) | \psi_\alpha^{DA}(\mathbf{r}; \mathbf{R}_0) \rangle. \tag{2.26}$$

Considering the Eq. 2.17 and 2.18 the Hamiltonian $H_e(\mathbf{r}; \mathbf{R})$ can be written as

$$H_e(\mathbf{r}; \mathbf{R}) = H_e(\mathbf{r}; \mathbf{R}_0) + \Delta H. \tag{2.27}$$

The quantity ΔH is a function of ξ which is it self a very small quantity, consequently, ΔH is also a small quantity. Therefore, ΔH can be considered as small perturbation to the $H_e(\mathbf{r}; \mathbf{R}_0)$. Then, the Eq. 2.26 recasts into

$$H_{\alpha\beta} = U_{\alpha\alpha}^{DA}(\mathbf{r}; \mathbf{R}_0) + \Delta H_{\alpha\beta}. \tag{2.28}$$

In the diabatic representation of electronic Hamiltonian U_α^{DA} appears as the diagonal elements, which is the so-called diabatic PES, and $\Delta H_{\alpha\beta}$ is the inter-state diabatic coupling term which are function of coordinates. The major advantages of the diabatic representation are the KE operator remain no longer off-diagonal and the electronic Hamiltonian is no more involved with the derivative coupling elements which was the bottleneck in the adiabatic representation (see Eq. 2.15).

2.1.4 Adiabatic to diabatic transformation

The transformation of adiabatic electronic basis to diabatic basis should be executed by an unitary transformation so that physical significance of the two electronic basis do not change. Following this philosophy we can build up a relation between the two representations as follows: the total wave function is

$$\Psi(\mathbf{r},\mathbf{R}) = \sum_{\alpha,k} |\chi^{AA}_{\alpha k}(\mathbf{R})\psi^{AA}_{\alpha}(\mathbf{r};\mathbf{R})\rangle \tag{2.29}$$

$$\begin{aligned}\Psi(\mathbf{r},\mathbf{R}) &= \sum_{\alpha,k} |\chi^{DA}_{\alpha k}(\mathbf{R})\psi^{DA}_{\alpha}(\mathbf{r};\mathbf{R}_0)\rangle \\ &= \sum_{\alpha,k} |\chi^{AA}_{\alpha k}(\mathbf{R})a^{*}_{\alpha\beta}(\mathbf{R})a_{\alpha\beta}(\mathbf{R})\psi^{AA}_{\alpha}(\mathbf{r};\mathbf{R})\rangle.\end{aligned} \tag{2.30}$$

Therefore, the diabatic and adiabatic electronic wavefunctions are related by the following equation (in matrix formalism)

$$\boldsymbol{\psi}^{DA} = \mathbf{A}\boldsymbol{\psi}^{AA}, \qquad \& \qquad \boldsymbol{\chi}^{DA} = \mathbf{A}^{\dagger}\boldsymbol{\chi}^{AA} \tag{2.31}$$

where $\mathbf{A}$ is the unitary matrix which is known as adiabatic to diabatic transformation (ADT) matrix and its elements are $a_{\alpha\beta}$. In order to minimize the nonadiabatic terms present in the adiabatic representation, the ADT matrix has to satisfy the following two conditions (see APPENDIX-B)

$$\sum_{i} \nabla_{n,i}\mathbf{A} + \mathbf{d}_i\mathbf{A} = \mathbf{0}, \tag{2.32}$$

and

$$\sum_{i} \nabla^2_{n,i}\mathbf{A} + 2\mathbf{d}_i \cdot \nabla_{n,i}\mathbf{A} + \mathbf{D}_i\mathbf{A} = \mathbf{0}, \tag{2.33}$$

where the elements of the operators $\mathbf{d}_i$ and $\mathbf{D}_i$ are defined in Eq. 2.16. Implementing these

two conditions, the nuclear TISE in diabatic representation can be simplified into

$$\sum_i -\frac{\hbar^2}{2M_i}\nabla^2_{n,i}\boldsymbol{\chi}^{DA} + (\mathbf{U}^{DA} - \mathbf{E}^{DA})\boldsymbol{\chi}^{DA} = \mathbf{0}. \tag{2.34}$$

The diabatic PE matrix $\mathbf{U}^{DA}$ is related to the adiabatic PE matrix by the following equation

$$\mathbf{U}^{DA} = \mathbf{A}^{\dagger}\mathbf{U}^{AA}\mathbf{A}. \tag{2.35}$$

The necessary condition to solve Eq. 2.32 is the so-called "curl condition" [52, 53, 54]

$$\sum_i \nabla_{n,i} \times \sum_i \mathbf{d}_i\mathbf{A} = 0. \tag{2.36}$$

The calculation of ADT matrix $\mathbf{A}$ utilizing this equation is very tedious because of large size of matrix $\mathbf{A}$ specifically for polyatomic molecules. To avoid the computational struggle for diabatization by this method a computationally inexpensive but effective scheme is generally used where a model diabatic Hamiltonian is constructed using a prescribed method and then the adiabatic Hamiltonian is obtained by the diagonalization of the diabatic Hamiltonian. Now the unknown coefficients present in the adiabatic Hamiltonian is determined by fitting it with the adiabatic energies calculated from the electronic TISE at different geometries.

In this formalism of adiabatic to diabatic transformation one has to calculate the ADT matrix, $\mathbf{A}$ implementing the condition described in Eq. 2.32. Therefore, calculation of the nonadiabtic coupling matrix, $\mathbf{d}_i$, is the crucial part in this formalism. There are plenty of software (MOLPRO, GAMESS) available for the calculation of nonadiabatic coupling matrix at some level of theory (MRCI, CASSCF). Then the mathematical formula of ADT matrix is assumed to be (considering a two state system and without loosing any generality of the ADT matrix which should be an unitary matrix)

$$\mathbf{A} = \begin{pmatrix} \cos(\Theta) & -\sin(\Theta) \\ \sin(\Theta) & \cos(\Theta) \end{pmatrix} \tag{2.37}$$

where the angle Θ is the mixing angle. Now, the mixing angles are calculated from the Eq. 2.32 and the matrix **A** is obtained and from Eq. 2.35 the diabatic PE calculate. In principle this rigorous formalism can be implemented all the molecular systems but this becomes very tedious for polyatomic systems containing more than 3 atoms because the accurate calculation of nonadiabatic coupling matrix becomes very challenging and time consuming. Therefore, to avoid the calculation of *ab initio* nonadiabatic coupling matrix a quasi-diabatization scheme was proposed.

The $U^{DA}_{\alpha\alpha}$ and $\Delta H_{\alpha\beta}$ in Eq. 2.28 can be expanded using Taylor series as

$$\begin{aligned} U^{DA}_{\alpha\alpha} =& E^0_{\alpha\alpha} + \sum_t \kappa^{\alpha\alpha}_t Q_t + \frac{1}{2}\sum_t \omega^{\alpha}_t Q^2_t + \frac{1}{2}\sum_c \omega^{\alpha}_c Q^2_c + \sum_{m,m'} \gamma^{\alpha\alpha}_{m,m'=t,c} Q_m Q_{m'} \\ \Delta H_{\alpha\beta} =& \sum_c \lambda^{\alpha\beta}_c Q_c, \qquad\qquad \alpha \neq \beta. \end{aligned} \tag{2.38}$$

The $\kappa^{\alpha\alpha}_t$ represent the PE gradients at the reference geometry for α electronic state. The term Q_t are the tuning modes which tunes energy gap between the electronic states [55, 56]. The quantity $\lambda^{\alpha\beta}_c$ represents the first-order inter-state vibronic coupling constant for α-β states and the associated modes Q_c are called coupling modes [55, 56]. The terms $\gamma^{\alpha\alpha}_{m,m'}$ are the intra-state bilinear coupling constants.[55, 56, 57]

The eigenvalues of $H_{\alpha\beta}$ matrix are (cf. Eq. 2.28)

$$E_{\pm} = \frac{1}{2}(U^{DA}_{\alpha\alpha} + U^{DA}_{\beta\beta}) \pm \frac{1}{2}\sqrt{(U^{DA}_{\alpha\alpha} - U^{DA}_{\beta\beta})^2 + 4|\Delta H_{\alpha\beta}|^2} \tag{2.39}$$

where $E_{\pm}$ are the adiabatic energies. The inter-state coupling constant $\lambda^{\alpha\beta}_c$ is calculated by

the following relation [58]

$$\lambda_c^{\alpha\beta} = \left[\frac{1}{8}\frac{\partial^2}{\partial Q_c^2}(E_+ - E_-)^2\Big|_{\mathbf{Q}=0}\right]^{\frac{1}{2}}. \tag{2.40}$$

So in this formalism the inter-state coupling can be calculated by Eq. 2.40 directly from the adiabatic energies and the diabatic PES are obtained by the Eq. 2.39. The mixing angle in Eq. 2.37 is related to the diabatic energies $U_{\alpha\alpha}^{DA}$, $U_{\beta\beta}^{DA}$, and diabatic coupling, $\Delta H_{\alpha\beta}$, by following equation

$$\Theta = \frac{1}{2}\tan^{-1}\Big[\frac{2\Delta H_{\alpha\beta}}{(U_{\beta\beta}^{DA} - U_{\alpha\alpha}^{DA})}\Big]. \tag{2.41}$$

The quasi-diabatization also has drawbacks. The equation which calculates the inter-state coupling, $\lambda_c^{\alpha\beta}$ (Eq. 2.40), is formulated within the limit of linear vibronic coupling (LVC) approximation. The accuracy of this formalism is limited to cases where the molecular Hamiltonian is represented in mass-weighted normal modes and where the displacement from equilibrium is not substantial enough to induce molecular fragmentation, such as in scattering of atom-molecule systems. Thus, it is well-suited for the calculation of the vibronic coupling Hamiltonian. Yet, this formalism is incapable of diabatizing between states of the same symmetry in vibronic coupling Hamiltonian. For the diabatization of same symmetry states four-fold diabatization scheme is generally used developed by Truhlar and coworkers[59, 60, 61, 62, 63, 64]. To study the potodissociation or scattering processes the Hamiltonian has to be represented in Jacobi or internal coordinates.

2.1.5 Conical intersection

To begin the discussion of CI, let us start with the rules and regulations for crossing two PE curves. In 1927 Hund proposed a qualitative characterization of the conditions for crossing two PE curves which was further mathematically proved in 1929 by Neumann and Wigner.[65, 66]

To establish the conditions for crossing two PE curves mathematically, we adopted the

formulation given by E. Teller in Ref. [67]. For a given system, if all the electronic wave functions are known to us except the two whose corresponding curves cross each other, then the wave functions of those two states can be expressed as

$$\psi = c_1\phi_1 + c_2\phi_2, \tag{2.42}$$

where ϕ_1 and ϕ_2 are the two arbitrary wave functions which are orthogonal two each other as well as the other known electronic wave functions. Now the characteristic equation will determine the PESs as follows

$$\begin{vmatrix} H_{11} - E & H_{12} \\ H_{21} & H_{22} - E \end{vmatrix} = 0, \tag{2.43}$$

and the coefficients c_1 and c_2 are determined by

$$\begin{pmatrix} H_{11} - E & H_{12} \\ H_{21} & H_{22} - E \end{pmatrix} \begin{pmatrix} c_1 \\ c_2 \end{pmatrix} = 0. \tag{2.44}$$

If in our problem the spin-orbit coupling is negligible, then the off-diagonal elements H_{12} and H_{21} are real valued. The eigenvalues of Eq. 2.43 are

$$E_{\pm} = \frac{H_{11} + H_{22}}{2} \pm \frac{1}{2}\sqrt{(H_{11} - H_{22})^2 + 4|H_{12}|^2}. \tag{2.45}$$

These two eigenvalues $E_{\pm}$ represents the two adiabatic PE curves which cross each other. Now, consider the separation between these two potentials

$$\Delta H = \sqrt{(H_{11} - H_{22})^2 + 4|H_{12}|^2}. \tag{2.46}$$

At the intersection of the two energy curves $\Delta H = 0$ and the necessary and sufficient

conditions are

$$H_{11} = H_{22} \qquad \& \qquad H_{12} = 0. \tag{2.47}$$

These two conditions represent two independent equations which can only be satisfied simultaneously if and only if H_{11}/H_{22} and H_{12} depend on two independent variables or coordinates, respectively. In the case of diatomic molecules only one independent coordinate is possible therefore the two conditions can not be satisfies and two PE curves never cross each other and this is the so-called "non-crossing rule". On the other hand, for polyatomic molecules there are enough independent variable are available which can satisfy the two conditions simultaneously. Therefore, surface crossings or degeneracies are quite typical.

Suppose for a polyatomic molecule the two independent variables are x and y, and the origin is at the point where the surface intersect. Then the first order Taylor series expansion of the Hamiltonian leads to

$$\begin{vmatrix} H_0 + h_1 x - E & ly \\ ly & H_0 + h_2 x - E \end{vmatrix} = 0, \tag{2.48}$$

and the eigenvalues are

$$E_{\pm} = H_0 + mx \pm \sqrt{k^2 x^2 + l^2 y^2}, \tag{2.49}$$

where $m = \frac{1}{2}(h_1 + h_2)$ and $k = \frac{1}{2}(h_1 - h_2)$. In this (x,y) coordinate space, the gap between the two eigenvalues (adiabatic PESs) is

$$E_+ - E_- = 2\sqrt{k^2 x^2 + l^2 y^2} \tag{2.50}$$

A CI is what we call this surface crossing, as this mathematical expression reveals that the PESs form a double cone with its vertex at the origin.[56, 68]. We call the (x,y) coordinate space the branching space, with its (N-2)-dimensional complement forming the CI seam.

2.1.6 Geometrical phase factor

The adiabatic electronic wave function is expressed by, $\boldsymbol{\psi}^{AA} = \mathbf{A}^{\dagger}\boldsymbol{\psi}^{DA}$, where $\mathbf{A}$ is defined by Eq. 2.37 and the mixing angle, Θ, is defined by Eq. 2.41. This general expression of Θ recasts in the branching space (x,y) (as mentioned in the previous section) as

$$\Theta = \frac{1}{2}\tan^{-1}\left[\frac{\gamma y}{x}\right], \qquad \text{where} \qquad \gamma = \frac{k}{l}. \tag{2.51}$$

On the other hand, the geometric angle in the branching space (x,y) reads as

$$\theta = \tan^{-1}\left[\frac{y}{x}\right], \tag{2.52}$$

therefore, when the electronic wave function encircles around the CI by a circular path the geometric angle completes a 2π rotation whereas the mixing angle completes a rotation of π only. Now the status of ADT matrix $\mathbf{A}$ at $\Theta = \pi$ is

$$\mathbf{A}(\Theta = \pi) = \begin{pmatrix} \cos(\pi) & -\sin(\pi) \\ \sin(\pi) & \cos(\pi) \end{pmatrix} = \begin{pmatrix} -1 & 0 \\ 0 & -1 \end{pmatrix} = -\mathbf{A}(\Theta = 0). \tag{2.53}$$

Thus, a key result of CIs is the occurrence of very fast nonadiabatic transitions between electronic states, alongside the geometric phase (GP) effect.[69, 70] Expanding on the idea of the GP effect, this implies that when an adiabatic electronic wavefunction traces a 2π loop around a CI, it undergoes a phase shift of π. This sign change makes the electronic wavefunction "non-single-valued" in that coordinate space (cf. Eq. 2.53).[71, 72] In essence, to ensure the total molecular wavefunction remains single-valued despite the GP effect, the nuclear wavefunction must also acquire a π phase shift when encircling a CI. The transformation to a diabatic basis is a well-suited approach to handle this inherent discontinuity, as it provides a representation where the electronic states and their couplings

are smooth functions of the nuclear coordinates. This circumvents the complexities arising from the non-single-valued nature of adiabatic electronic wavefunctions in the vicinity of a CI. This means that when we analyze the molecular dynamics using a diabatic representation, the GP effect is inherently accounted for. This is because the diabatic approach naturally satisfies the correct boundary conditions when the system effectively "circles" a CI. Within this representation, the GP effect reveals itself clearly through a distinct change in the nodal pattern of the nuclear wavefunction along a coupling coordinate, particularly when a diabatic transfer occurs in the presence of a CI.[73] This observation stems from the nature of the diabatic coupling element within the diabatic PE matrix. Specifically, this coupling element is an odd function of the coupling coordinate (in a first-order approximation). This odd symmetry of the coupling is what mathematically enforces the phase change in the nuclear wavefunction, leading to the observed alteration in the nodal pattern when encircling a CI during diabatic transfer (see Chap. 3 and Chap. 4).

2.2 Optimal control theory

The OCT is a branch of mathematics where optimization of a target function or functional is optimized using some optimization tools like conjugate-gradient method, GA etc. When these mathematical frameworks are applied on the quantum systems, like atom or molecule, to control its internal dynamics which is governed by a time evolution operator following the basic principles of quantum mechanics, it is generally termed as quantum control (herein after the term 'OCT' and 'quantum control' will be used for the same purpose). The major goal in OCT is the determination of best or optimal values of external parameters on which the dynamics of the quantum system explicitly depends. The most suitable external parameters are selected by judging the corresponding cost functional values. The functional depends on the control variables and some physical observables whose fate is determined by time dependent external control.

This work applies OCT to determine the optimal shape of laser pulse(s). These precisely sculpted pulses guide a molecular system from its initial state to a specific target state. The underlying principle is simple: the electric field of the optimal laser pulse interacts with the molecule's permanent dipole moment, steering it toward the desired final configuration. The TDSE in presence of laser field can be written as follows

$$i\hbar\frac{\partial}{\partial t}\psi(x,t) = [\mathbf{H} - \overrightarrow{\mu}\cdot\overrightarrow{\epsilon}(t)]\psi(x,t), \tag{2.54}$$

where **H** represents the system Hamiltonian, $\overrightarrow{\mu}$ and $\overrightarrow{\epsilon}$ are the dipole moment of the system and electric field of the laser pulse, respectively. Hence, the OCT is a fusion of the TDSE within dipole moment approximation and mathematical tools which modulates the spectral and temporal profiles of laser during the dynamics to explore all the possible pathways encompassing the electronic or vibronic excitations and their time evolutions. Ultimately, the quantum mechanical interferences among these numerous pathways become crucial in successfully steering the system towards its desired target state. The constructive interferences lead to the desired target whereas destructive interference, not. A detail mathematical formulation of OCT is given below.

2.2.1 Formulation

The major aim of OCT is to come up with the best combination of laser-parameter values, which decides its spectral and temporal profile, to maximize the expectation values of specific physically observable operators, $\hat{O}$, within a desired target state, $\psi(T)$, or along a particular reaction channel. This optimal laser pulse design is achieved by formulating the problem in terms of a "cost functional," $J[\epsilon(t)]$. It consists of three parts,

$$J[\epsilon(t)] = J_o + J_p + J_c. \tag{2.55}$$

The first term, J_o, is the expectation of physical observable which is known as objective

term. Generally, it is expressed as $\left|\left\langle\psi(T)\middle|\hat{O}\middle|\psi(T)\right\rangle\right|$. The second term, J_p, contains the mathematical expression of the laser field and a Lagrangian multiplier which is termed as penalty factor and is independent of laser parameters. This penalty factor is crucial; it helps prevent the occurrence of undesirable physical processes. The third term, J_c, ensures the system's evolution adheres to the TDSE, acting as a dynamic constraint throughout the controlled process.

The formulation of objective term depends of the given problem. The objective terms can be categorized into two types, time-dependent and time-independent. The time-dependent objective term should be constructed in a way such that the expectation value of the operator, $\hat{O}$, has to be optimized at each of the time steps during the dynamics. For instance, this could involve maximizing the outgoing dissociative flux across a dividing line at each discrete time interval. On the other hand, the time-independent objective has to be optimized at the target state, $\psi(T)$, at time T from its initial state $\psi(0) = \phi_i$. For instance, maximization of the projection of the wave function with predefined vibrational state. The specific objective function chosen is always tailored to the precise nature of the problem being tackled. Therefore, within this thesis, the detailed descriptions of the particular objective functions selected for their suitability in each scenario, presented in the relevant working chapters.

The second term, J_p, represents the electric field which is employed externally to the system of interest. The mathematical form of it is

$$J_p = -a_0 \int_0^T dt\left|\epsilon(t)\right|^2. \tag{2.56}$$

This formulation represents the fluence of the laser pulse. The penalty factor, a_0, is a crucial positive scalar. It's what precisely determines the weight of the fluence term within the functional, thereby controlling its influence on the overall optimization process. The negative sign in this term assures that, if the cost functional gets maximized, this penalty term gets minimized.

The third term, J_c, represents the dynamical constraint. Therefore, the evolution of the system has to endure the TDSE in Eq. 2.54.

At this stage, we can write the cost functional explicitly [74, 75] as follows

$$\begin{aligned} J[\epsilon(t)] = \lim_{T\to\infty} \big|\big\langle\psi(T)\big|\hat{O}\big|\psi(T)\big\rangle\big| - a_0 \int_0^T dt\big|\epsilon(t)\big|^2 \\ - 2Re\big[\int_0^T \big\langle\chi(t)\big|\frac{\partial}{\partial t} + i\hat{H}\big|\psi(t)\big\rangle\big]. \end{aligned} \tag{2.57}$$

Here, $\chi(t)$ serves as a Lagrange multiplier. This mathematical tool is introduced specifically to incorporate the system's dynamic constraints directly into the cost functional, ensuring that the optimized evolution strictly adheres to the governing equations of motion.

In order to find out the working equations for the calculation of the optimal laser pulse shape, the first order derivative of the cost functional with respect to $\psi(t)$, $\chi(t)$ and $\epsilon(t)$ is derived

$$\begin{aligned} \frac{\partial J}{\partial\psi(t)} = 0 \Rightarrow & i\frac{\partial\psi(t)}{\partial t} = \hat{H}\psi(t), \psi(t=0) = \psi(0), \\ \frac{\partial J}{\partial\chi(t)} = 0 \Rightarrow & i\frac{\partial\chi(t)}{\partial t} = \hat{H}\chi(t), \chi(T) = \hat{O}\psi(T), \\ \frac{\partial J}{\partial\epsilon^*(t)} = 0 \Rightarrow & \epsilon(t) = \frac{i}{\alpha_0}[\big\langle\chi_e(t)\big|\mu\big|\psi_g(t)\big\rangle - \big\langle\psi_e(t)\big|\mu\big|\chi_g(t)\big\rangle]. \end{aligned} \tag{2.58}$$

These three equations are solved iteratively in the OCT calculations. There are various methods available for the numerical evaluations of these three equations. However, a common challenge with these methods is their generally slow convergence towards an optimal (though often local) solution, which also entails significant computational complexity. To avoid these complexity the optimization protocols, such as conjugate gradient (CG) method [76, 77, 78, 79] and GA, are generally employed in OCT. The CG method is a gradient-based search algorithm that centers its optimization around the gradient of the

cost functional with respect to the laser field whereas the GA method based on biological evolution strategies where the optimal value of cost functional is reached by judging the fitness function iteratively. The GA is often favored in optimization due to its flexibility and ability to explore large solution spaces efficiently, especially in complex, non-linear, or multi-modal problems where traditional methods may struggle. Compared to CG, GAs are less prone to getting trapped in local minima and are particularly useful when the problem space isn't smooth or differentiable, which may impact CG's performance. Therefore, the GA is chosen as the optimization tool for all the projects in the present thesis due to its effective approach to finding optimal solutions and its improved accuracy compared to CG.

Genetic algorithm

In GA, the laser pulse is implemented by the following general expression

$$\epsilon_{ga}(t) = \epsilon_g(t) + \epsilon_r(t). \tag{2.59}$$

In this thesis work, $\epsilon_g(t)$ is set to zero, but generally, it is a light wave which represents a constant laser pulse or a initial lase pulse. The term $\epsilon_r(t)$ is represented as a product of envelop function, $S(t)$ and sinusoidal wave function with frequency, ω, as shown below

$$\epsilon_r(t) = \sum_{i=1}^{n} E_0^i \sin(\omega^i t) S(t), \tag{2.60}$$

where E_0 is the amplitude of the laser pulse. For a multi-frequency calculation n is greater than 1, so E_i and ω_i are the amplitude and frequency, respectively, of i-th component of electromagnetic wave.[80] Most of the works in the present thesis is done considering single frequency laser pulse only. The amplitude, E_0, is determined by the pulse area theorem.[81] The frequency ω is utilized as the frequency for the transition between the states. The envelope function, $S(t)$, is a mathematical tool that shapes a laser pulse. It needs to start at zero, gradually increase to a peak, and then smoothly return to zero. Various mathematical

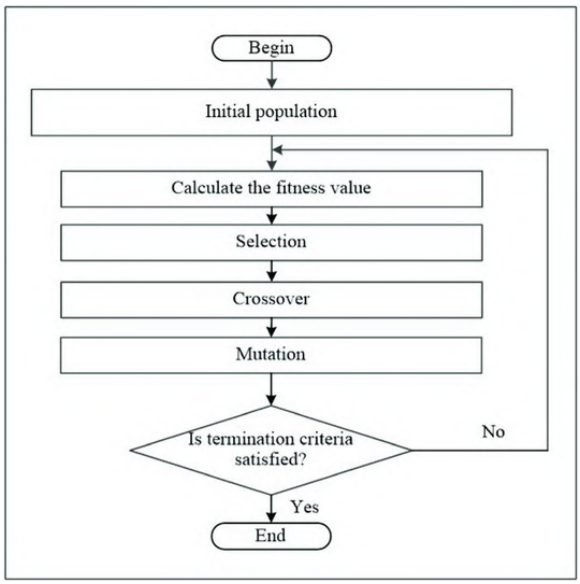

Figure 2.1: An outline of GA.

expressions can be used for $S(t)$ depending on the specific problem, and the forms used in this thesis are detailed in the working chapters.

Using GA, diverse combinations of frequency (ω), time parameters, and amplitude (E) are explored with the goal of identifying the best values of these parameters among all possible permutations. Each set of these parameters is referred to as an "individual" in GA. To find the optimal solution, a population of individuals is initially generated by randomly drawing parameter sets from the parameter space. Each parameter set is encoded as a "chromosome" in binary format. These randomly chosen individuals are then subjected to optimization to pinpoint the best solution that maximizes the cost functional. The overall optimization process is depicted in Fig. 2.1.

.

2.2.2 Time evolution

It is well understood that any quantum mechanical system can be fully described by the wave function, $\psi(x,t)$, where x and t represent the spatial and temporal coordinates, respectively. The governing equation of it is the TDSE

$$i\hbar\frac{\partial}{\partial t}\psi(x,t) = \hat{H}(x)\psi(x,t), \tag{2.61}$$

with the initial condition given by $\psi(x, t = 0) = \psi_0$, representing the wave function at time $t = 0$. As the Hamiltonian is time independent, the general solution of the TDSE is

$$\psi(x,t) = \exp\Big[-\frac{i\hat{H}t}{\hbar}\Big]\psi(x,0). \tag{2.62}$$

If we are concerned with the state of the system after an infinitesimal time increment, dt, from $t = 0$, such that the Hamiltonian $H(x)$ remains approximately constant, then Eq. 2.62 transforms into

$$\psi(x,dt) \approx \exp\Big[-\frac{i\hat{H}dt}{\hbar}\Big]\psi(x,0). \tag{2.63}$$

The total time tt can be represented as a sum of increments dt, such that $t = Ndt$. Likewise, the time $t + dt$ can be written as $t + dt = (N + 1)dt$. So the wave function at t and $t + dt$ can be written as

$$\begin{aligned}\psi(x,t) &\approx \exp\Big[-\frac{i\hat{H}Ndt}{\hbar}\Big]\psi(x,0)\\ \psi(x,t+dt) &\approx \exp\Big[-\frac{i\hat{H}(N+1)dt}{\hbar}\Big]\psi(x,0).\end{aligned} \tag{2.64}$$

This two equations leads to

$$\psi(x,t+dt) \approx \exp\Big[-\frac{i\hat{H}dt}{\hbar}\Big]\psi(x,t). \tag{2.65}$$

The the quantity, $\exp\Big[-\frac{i\hat{H}dt}{\hbar}\Big]$, is acting as the time propagation operator. The accuracy of the propagation depends on the size of the time interval dt; as dt becomes smaller, the accuracy increases.

The time propagation operator is an unitary operator. Its generally defined as $U(t)$

$$\begin{aligned} U(dt) &= \exp\Big[-\frac{i\hat{H}dt}{\hbar}\Big] \\ &= \exp\Big[-\frac{i[\hat{T}+\hat{V}]dt}{\hbar}\Big] \end{aligned} \tag{2.66}$$

where $\hat{T}$ and $\hat{V}$ are the KE and PE operator, respectively. At this stage, it is important to note the distinct characteristics of the two operators, $\hat{T}$ and $\hat{V}$. In coordinate space, $\hat{T}$ is non-local, while $\hat{V}$ is local. However, in momentum space, this relationship is reversed: $\hat{T}$ becomes local, and $\hat{V}$ becomes non-local. As a result, the operators do not commute, meaning $[\hat{T},\hat{V}] \neq 0$. Consequently, we have $\exp\Big[-\frac{i[\hat{T}+\hat{V}]dt}{\hbar}\Big] \neq \exp\Big[-\frac{i\hat{T}dt}{\hbar}\Big]\exp\Big[-\frac{i\hat{V}dt}{\hbar}\Big]$. Instead, we can expand it using Baker-Campbell-Hausdorff (BCH) formula [82] as

$$\begin{aligned} \exp\Big[-\frac{i[\hat{T}+\hat{V}]dt}{\hbar}\Big] = &\exp\Big[-\frac{i\hat{T}dt}{\hbar}\Big]\exp\Big[-\frac{i\hat{V}dt}{\hbar}\Big]\exp\Big[\frac{i[\hat{T},\hat{V}]dt}{2\hbar}\Big] \\ &\exp\Big[-\frac{i[\hat{T},[\hat{T},\hat{V}]]+[\hat{V},[\hat{V},\hat{T}]]dt}{12\hbar}\Big] \end{aligned} \tag{2.67}$$

To get rid of the commutator of $\hat{T}$ and $\hat{V}$, we can utilize Trotter-Suzuki decomposition technique

$$\exp\Big[-\frac{i[\hat{T}+\hat{V}]dt}{\hbar}\Big] = \lim_{n\to\infty}\left(\exp\Big[-\frac{i\hat{T}dt}{n\hbar}\Big]\exp\Big[-\frac{i\hat{V}dt}{n\hbar}\Big]\right)^n. \tag{2.68}$$

It is the first order decomposition and for finite n, this is an approximation with an error that decreases as n increases. To improve the accuracy second or higher Trotter-Suzuki decomposition technique can be implemented. In this thesis, the second-order expansion is applied, which is sufficiently accurate for the type of work presented across all projects.

The second-order expansion is given by

$$\exp\Big[-\frac{i[\hat{T}+\hat{V}]dt}{\hbar}\Big] \approx \exp\Big[-\frac{i\hat{V}dt}{2\hbar}\Big]\exp\Big[-\frac{i\hat{T}dt}{\hbar}\Big]\exp\Big[-\frac{i\hat{V}dt}{2\hbar}\Big]$$
$$\text{or} \tag{2.69}$$
$$\approx \exp\Big[-\frac{i\hat{T}dt}{2\hbar}\Big]\exp\Big[-\frac{i\hat{V}dt}{\hbar}\Big]\exp\Big[-\frac{i\hat{T}dt}{2\hbar}\Big].$$

The accuracy limit of these two decomposition methods is $\mathcal{O}(\{[\hat{T},\hat{V}]dt\}^3)$. Between the two, the first decomposition is comparatively faster than the second. The reason for this will become clearer as the discussion progresses.

If we consider the given Hamiltonian is in diabatic representation, then the KE operator $\hat{T}$ and PE operator $\hat{V}$ are diagonal and off-diagonal square matrix, respectively. The operators we get after the decompositions will act on the wave function $\psi(x,t)$ following some mathematical prescriptions. Let us consider a system of two electronic states, then the wave function of it is expressed as (in one dimensional space)

$$\boldsymbol{\psi}(x,t) = \begin{pmatrix} \psi_1(x,t) \\ \psi_2(x,t) \end{pmatrix}, \tag{2.70}$$

and the diabatic molecular Hamiltonian is expressed as

$$\hat{\boldsymbol{H}} = \hat{T}_x\mathbf{I}_2 + \begin{pmatrix} V_{11} & V_{12} \\ V_{21} & V_{22} \end{pmatrix}. \tag{2.71}$$

The PE part of the split-operator (SO) $\exp\Big[-\frac{i\hat{\mathbf{V}}dt}{2\hbar}\Big]$ can act on $\boldsymbol{\psi}$ following these steps:
(1) **Diagonalize the PE matrix:** Begin by diagonalizing the PE matrix $\mathbf{V}$ to obtain the transformation matrix $\mathbf{S}$ such that

$$\mathbf{V} = \mathbf{S}^\dagger\mathbf{V}_{diag}\mathbf{S}, \tag{2.72}$$

where $\mathbf{V}_{diag}$ is a diagonal matrix containing the eigenvalues of $\mathbf{V}$. Here, $\mathbf{V}_{diag}$ represents the adiabatic PE matrix, and $\mathbf{S}$ is the diabatic-to-adiabatic transformation matrix.

(2) **Rewrite the PE operator:** The PE operator can then be expressed as

$$\exp\Big[-\frac{i\hat{\mathbf{V}}dt}{2\hbar}\Big] = \mathbf{S}^{\dagger}\exp\Big[-\frac{i\hat{\mathbf{V}}_{diag}dt}{2\hbar}\Big]\mathbf{S}. \tag{2.73}$$

(3) **Simplify the operator in the diagonal basis:** The operator sandwiched between the two $\mathbf{S}$ matrices simplifies to

$$\exp\Big[-\frac{i\hat{\mathbf{V}}_{diag}dt}{2\hbar}\Big] = \begin{pmatrix} \exp\Big[-\frac{i\hat{\mathbf{V}}_{+}dt}{2\hbar}\Big] & 0 \\ 0 & \exp\Big[-\frac{i\hat{\mathbf{V}}_{-}dt}{2\hbar}\Big] \end{pmatrix}. \tag{2.74}$$

Although the KE operator $\hat{T}$ is a diagonal matrix in diabatic representation, the KE part of the SO, $\exp\Big[-\frac{i\hat{T}dt}{\hbar}\Big]$, cannot act directly on $\boldsymbol{\psi}$ in the coordinate space like the PE operator dose, because $\hat{T}$ is non-local in coordinate space. However, since $\hat{T}$ is local in momentum space, this operator can be applied by following these steps:

(1) **Fourier transformation of wave function:** At first, Fourier transform the wave function, $\boldsymbol{\psi}(x,t)$, to its momentum space representation, $\boldsymbol{\psi}(k,t)$, using fast Fourier transformation (FFT). Then, multiply it by the KE component of the SO in its momentum space, i.e. $\exp\Big[-\frac{i\hbar^2k^2}{2m}\frac{dt}{\hbar}\Big]$ at each grid point:

$$\exp\Big[-\frac{i\hbar^2k^2}{2m}\frac{dt}{\hbar}\Big] \times \mathbf{FFT}\{\boldsymbol{\psi}(k,t)\}. \tag{2.75}$$

(2) **Inverse Fourier transformation:** Then, Fourier transform this quantity back from momentum space to coordinate space to obtain the updated wave function in coordinate space:

$$\mathbf{FFT}^{-1}\Big\{\exp\Big[-\frac{i\hbar^2k^2}{2m}\frac{dt}{\hbar}\Big] \times \mathbf{FFT}\{\boldsymbol{\psi}(k,t)\}\Big\} \tag{2.76}$$

The Fourier transformation using the FFT method becomes computationally expensive as the

dimensionality of the coordinate space increases. Therefore, among the two decompositions shown in Eq. 2.69, the first one performs the FFT operation only two times per time step, whereas the second requires four FFT operations. To reduce computational load and save time, this thesis adopts the first type of decomposition.

The SO method is well-suited for propagating wavefunctions through time, especially when they evolve across multiple electronic states. This is because the SO method inherently preserves the unitary nature of the evolution operator. The coupling between these electronic states can stem from two main sources: nonadiabatic interactions, which are time-independent, or interactions with light through the transition dipole moment (TDM), which are time-dependent.

CHAPTER 3

Optimal Control of N-H Photodissociation of Pyridinyl

3.1 Introduction

Quantum control of chemical processes like photodissociation, photoinduced intramolecular H-transfer, cis-trans photoisomerisation etc. by tailored laser pulse has been pursued over a long time.[83] The evolution of the molecular system towards a desired target state can be monitored by modulating the parameters associated with the laser field viz. frequency, amplitude, phase, shape and delay time between pump-dump pulses etc. There are several algorithms by which one can determine the optimal parameters of the laser pulse. The GA is one of them and emerged as one of the useful stochastic optimization algorithm. Within a given parameter range the GA efficiently drives the process to the optimal outcome.

There are many different ways to choose the parameters for a specific desired objective to be controlled for different processes depending upon the topography of the PESs of the system. For example, for a PES where two exit channels are degenerate, one can modulate the phases of the pump-dump pulses in a way that the product branching ratios can be

controlled by constructive or destructive interferences of the wave functions.[10, 11, 84, 85] Tannor and Rice[16], and Tannor, Kosloff and Rice[21] have shown that the delay time between pump-dump pulses can be tuned to manipulate the product formation in the ground electronic state. Serrano-Jiménez *et al.* [86] have suggested a pump-dump scheme to coherent control product branching ratios of CH_3I photodissociation in the weak field regime. It is also possible to monitor the photodissociation product branching ratio using a single ultrashort laser pulse, regulating the frequency, amplitude, and shape within the OCT framework.[80, 87, 88]

Pyridinyl ($PyH^{\cdot}$) radical is one of the simplest hypervalent aromatic radical which appears as an intermediate in the reaction of water splitting where pyridine acts as a photocatalyst.[89] Pyridine is not a good chromophore itself in this solar water splitting, it absorbs rather in the far UV region, whereas $PyH^{\cdot}$ absorbs in the UV region. The $\pi\pi^*$ excitation ($\sim$4.8 eV) of Py-H_2O complex leads to the production of $PyH^{\cdot}$ and $^{\cdot}OH$.[90] $PyH^{\cdot}$ is an intermediate which dissociates into Py and $H^{\cdot}$ following electronic excitation by visible light ($\sim$600 nm, $\sim$2 eV).[91]

Ehrmaier *et al.*[92] have carried out detailed electronic structure calculations and also studied field free dynamics on the $\pi\sigma^*$ electronic state of $PyH^{\cdot}$. The ground-state equilibrium geometry of pyridinyl radical was calculated at the unrestricted Møller-Plesset second-order perturbation (UMP2) theory level using correlation consistent double-ζ basis set (cc-pVDZ) of Dunning.[93] It was found from the CASSCF calculation that the highest occupied molecular orbital (HOMO) is $3b_1$ which is singly occupied. The lowest unoccupied molecular orbital (LUMO) and LUMO+1 are σ^* and π^* orbitals of $12a_1$ and $2a_2$ symmetry, respectively. However, CASPT2 calculation revealed that the π^* orbital is energetically lower than the σ^* orbital [see Table I in ref. 14]. The first (D_1) and second (D_2) excited adiabatic electronic states are dominated by the configurations of singly occupied $2a_2$ and $12a_1$ MOs, respectively. The PESs of the ground and the two low-lying excited states ($\pi\pi^*$ and $\pi\sigma^*$) were calculated using CASSCF/CASPT2 methods employing aug-cc-pVDZ basis

set. The active space for the CASSCF calculation includes the $\sigma(a_1)$ and $\sigma^*(a_1)$ orbitals of the N-H bond and three ring-centered π (two b_1 and one a_2) and π^* (one b_1 and two a_2) orbitals. The interstate coupling parameters along the coupling vibrational normal modes at the two CIs revealed that the $Q_7(b_1)$, $Q_8(b_1)$ and $Q_9(a_2)$ are the most relevant coupling modes (see Table II and III of ref. 14).

Field free nonadiabatic quantum dynamics has been investigated on coupled three dimensional PESs using the multi-configuration time-dependent Hartree (MCTDH) method.[92] An explicit dependence of the N-H dissociation yield on the initial vibrational excitation along N-H stretching and coupling coordinates was found from these calculations. The initial excitation along the N-H stretching coordinate facilitate the hydrogen abstraction. The photodissociation is also sensitive to the initial vibrational excitation along the coupling coordinates.

In the present work, the photoinduced N-H bond photodissociation dynamics is investigated within the mathematical framework of OCT employing the GA as an optimization tool where maximization of N-H dissociation yield is the target. A single UV laser pulse of a few femtosecond time period is optimized in terms of frequency, amplitude and the shape of the pulse as parameter. The considered laser pulses are in the strong field regime which is suitable for the present PES model, where the energy difference between the ground state and excited state in the asymptotic region is large and there is very low probability of dissociation through the excited state.

3.2 Theory and methodology

A three-states and three-modes model Hamiltonian is constructed in the present quantum dynamics investigation of the N-H photodissociation of pyridinyl molecule. In this model Hamiltonian, the distance between the center-of-mass of pyridine residue and the H-atom *i.e.* referred as the Jacobi distance, *R* (a_1 symmetry) [cf., Fig. 3.1(a)] is the reaction

coordinate. The out-of-plane bending coordinate, represented by jacobi angle of H-atom, Θ (b_1 symmetry) [cf., Fig. 3.1(a)] and the normal vibrational coordinate, Q_9 (a_2 symmetry) [cf., Fig. 3.1(b)] are taken as the two coupling coordinates. Three electronic states in a diabatic representation are designated as ground state ($3b_1$), $\pi\pi^*$ ($2a_2$) and $\pi\sigma^*$ ($12a_1$). In the adiabatic representation they are designated as D_0, D_1 and D_2. D_0/D_1 and D_1/D_2 CIs due to crossing of $12a_1$-$3b_1$ and $12a_1$-$2a_2$, are located at $R = 5.37$ a.u. and $R = 5.03$ a.u., respectively [cf., Fig. 3.2]. Coordinates Θ and Q_9 are the most important ones to couple the D_0-D_1 and D_1-D_2 electronic states, respectively.

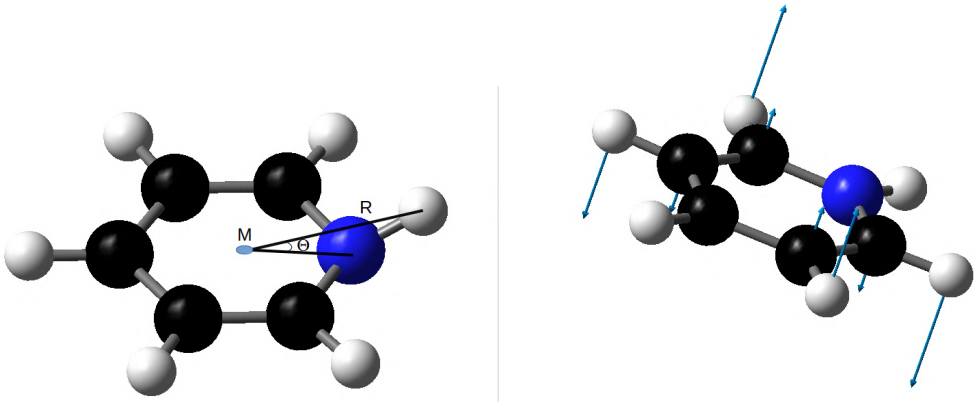

(a) (b)

Figure 3.1: (a)Jacobi coordinates R and Θ. M is the center of mass of the pyridine residue. (b) Nuclear displacement vectors for Q_9 vibrational mode.

Quantum dynamics calculations are carried out by solving the TDSE on the nonadiabatically coupled three electronic states. In a diabatic electronic representation the Hamiltonian

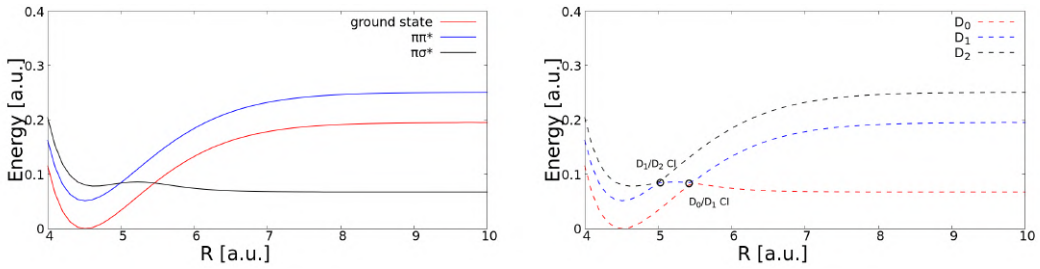

(a) (b)

Figure 3.2: (a) and (b) are diabatic and adiabatic energy curves of the three energetically lowest electronic states of pyridinyl along the Jacobi coordinate *R*, respectively.

reads

$$\boldsymbol{H} = \boldsymbol{T}_N \boldsymbol{I}_3 + \boldsymbol{V}, \tag{3.1}$$

where $\boldsymbol{I}_3$ is a 3×3 diagonal unit matrix and KE operator T_N reads (in atomic units)

$$\boldsymbol{T}_N = -\frac{1}{2\mu}\frac{\partial^2}{\partial R^2} - \frac{1}{2}\omega_9 \frac{\partial^2}{\partial Q_9^2} - \frac{1}{2I}\frac{\partial^2}{\partial \Theta^2}. \tag{3.2}$$

Here μ and I are the reduced mass along reaction coordinate and moment-of-inertia along Θ coordinate, respectively [cf., eq. 8-11 in Ref. 15]. ω_9 is the harmonic frequency of the Q_9 normal mode.

The diabatic potential matrix is given by

$$\boldsymbol{V} = \begin{pmatrix} V_{00} & V_{01} & V_{02} \\ V_{01} & V_{11} & V_{12} \\ V_{02} & V_{12} & V_{22} \end{pmatrix}, \tag{3.3}$$

The diagonal terms of $\boldsymbol{V}$ are the diabatic potential energies of the three electronic states which are functions of R, Θ and Q_9. The off-diagonal terms define the diabatic coupling potential. The $\pi\sigma^*$ ($12a_1$) state is coupled to the $\pi\pi^*$ ($2a_2$) and ground state ($3b_1$) therefore, V_{02} and V_{12} are non-zero, whereas V_{01} is zero. The PE matrix is constructed from the fitted equations given in APPENDIX A of Ref. 15. It is worthwhile to mention here that there is a typo in Eq. (A8) where the exponential function should be $e^{(-l_2(R-R_5))}$ instead of $e^{(-l_2(R-R_5)^2)}$ which is unfortunately overlooked by the authors. The diagonal (V_{00}, V_{11}, V_{22}) and off-diagonal (V_{02} and V_{12}) elements of the diabatic PES matrix are presented in Fig. 3.3. The interaction potential for $\pi\pi^*$ excitation from the ground state by the continuous laser pulse is, $-\mu_{01}.E(t)$. The latter is added to the diabatic coupling potentials introduced above. The quantity μ_{01} is the TDM between ground and $\pi\pi^*$ electronic state, and $E(t)$ is the time dependent electric field of the laser pulse. The $\pi\sigma^*$ state is optically dark and,

Table 3.1: Energy eigenvalues [in cm^{-1}] of the vibrational wave functions of the electronic ground state of pyridinyl.

$\|n_R, n_\Theta, n_{Q_9}\rangle$	**Eigenvalue**	previous results[92]
$\|0,0,0\rangle$	2467	2376
$\|0,0,1\rangle$	2912	2811
$\|0,1,0\rangle$	3357	3241
$\|0,1,1\rangle$	3804	3676

it is unlikely that it is directly populated by light absorption from the electronic ground state.[92] Therefore, the TDM, μ_{02}, is taken as zero. The only optically bright excited electronic state present in this system is the $\pi\pi^*$ state and the corresponding transition moment, μ_{01}, is taken constant (unity). This constant dipole moment approximation is a valid approximation in a diabatic electronic basis as the electronic character of the states remains unchanged throughout the nuclear coordinate space in this basis.[94] This is also verified in our recent studies on the photodissociation of pyrrole and photoinduced H-transfer in malonaldehyde.[87, 95, 96]

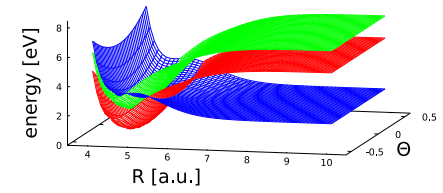

(a) V_{00},V_{11},V_{22} in R and Θ space.

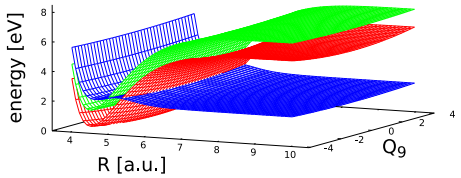

(b) V_{00},V_{11},V_{22} in R and Q_9 space.

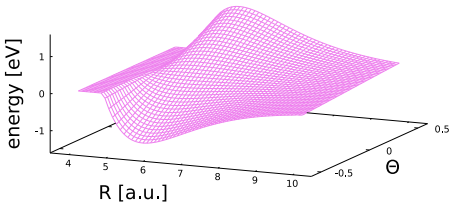

(c) V_{02}

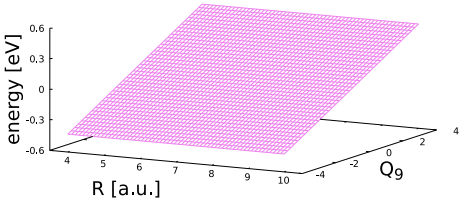

(d) V_{12}

Figure 3.3: Diabatic PESs and the coupling potential energies (c and d) as function of R, Θ and Q_9 coordinates.

The photoinduced dissociation of N-H bond of pyridinyl molecule is investigated by

numerically solving the TDSE using the model Hamiltonian [cf., Eq.(3.1-3.3)] within a semi-classical dipole approximation [97, 98] on a three dimensional grid points with $3.5 \leq R \leq 12.0$ (bohr), $-1.5 \leq \Theta \leq 1.5$ (rad.) and $-20.0 \leq Q_9 \leq 20.0$ (in dimensionless unit). For the propagation of the WP in time a second order SO method is employed[99, 100] to three coupled electronic states.[101, 102] The vibronic wave functions of the diabatic ground electronic state are considered as the initial condition to solve the TDSE. These wave functions are calculated by a pseudospectral method (see APPENDIX D) and they are designated as $|n_R, n_\Theta, n_{Q_9}\rangle$ where n_R, n_Θ and n_{Q_9} are the number of nodes of the wave function along these coordinates. Some of the wave functions are shown in Fig. 3.4. A few energy eigenvalues of the ground electronic state are given in Table 3.1. The initial WP prepared on the ground electronic state is gradually pumped to the excited $\pi\pi^*$ electronic state by a time-dependent laser pulse.

The TDSE of the coupled manifold three electronic states reads (in atomic units)

$$i\frac{\partial}{\partial t}\begin{pmatrix}|\psi_0\rangle\\|\psi_1\rangle\\|\psi_2\rangle\end{pmatrix} = \mathbf{H}\begin{pmatrix}|\psi_0\rangle\\|\psi_1\rangle\\|\psi_2\rangle\end{pmatrix}, \tag{3.4}$$

To avoid reflection of the WP components from the grid boundary it is multiplied with a sine type of damping function in the asymptotic region of the reaction coordinate[103]. The damping function reads

$$f(R_i) = \sin\left[\frac{\pi}{2}\frac{(R_{mask} + \Delta R_{mask} - R_i)}{\Delta R_{mask}}\right], \qquad R_i \geq R_{mask}, \tag{3.5}$$

here $R = R_{mask}$ is the point where damping is activated and its value is 1.0 up to this point. It gradually decreases to zero at the grid edge. The dissociation yield is calculated as the time accumulated flux on a dividing surface located at $R = R_{flux}$ in the asymptotic region of the product channels. The time accumulated flux on the i-th electronic state in

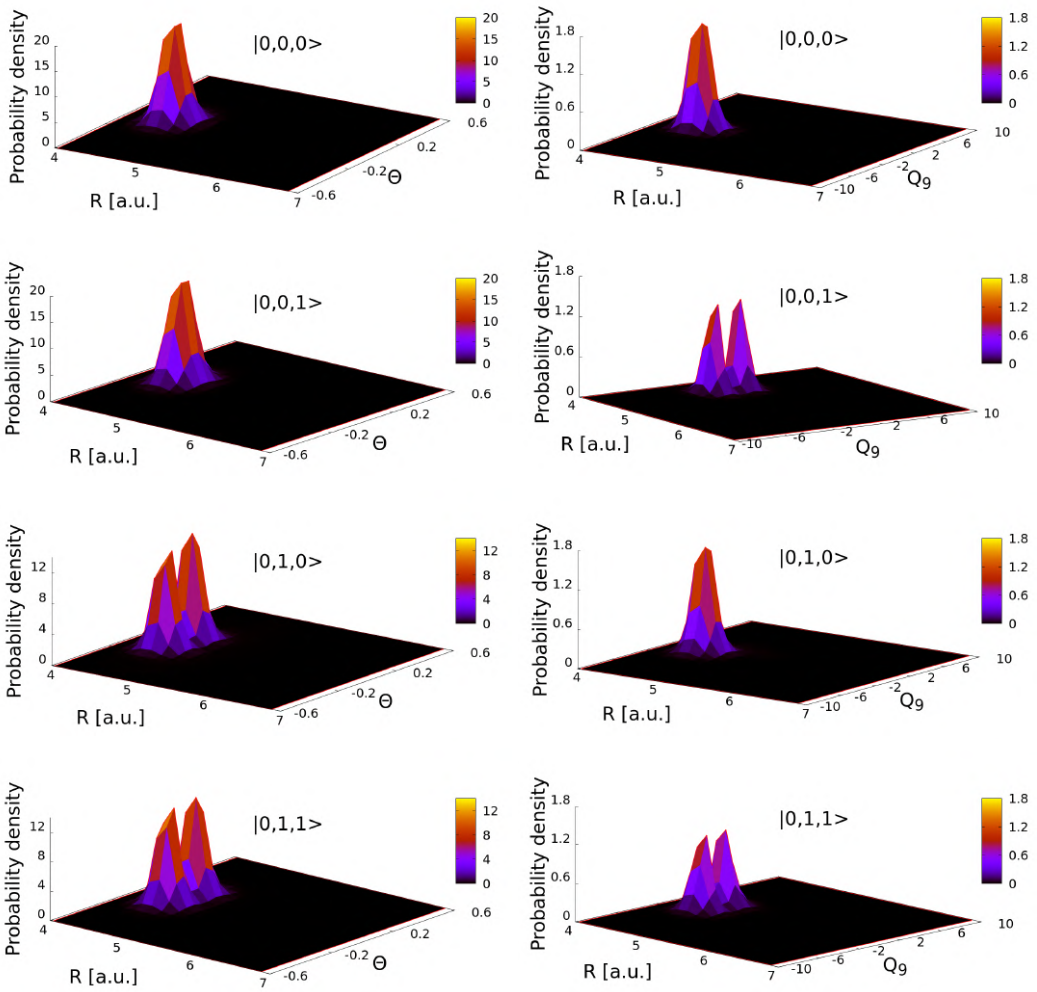

Figure 3.4: The probability density of $|0,0,0\rangle$, $|0,0,1\rangle$, $|0,1,0\rangle$ and $|0,1,1\rangle$ vibrational wave functions of the electronic ground state calculated by the pseudo spectral method. The wave function probability densities are plotted in $R-\Theta$ and $R-Q_9$ space.

diabatic(d)/adiabatic(a) representation is given by (in atomic units)

$$\Phi_i^{d/a}(t) = \frac{1}{\mu}\int_{t=0}^{t} Im\left[\iint (\psi_i^{d/a}(R,\Theta,Q_9,\tau))^* \frac{\partial \psi_i^{d/a}(R,\Theta,Q_9,\tau)}{\partial R}\bigg|_{R=R_{flux}} d\Theta\, dQ_9\right] d\tau. \tag{3.6}$$

and the total flux for the dissociation on the three electronic states is

$$\Phi^{d/a} = \sum_{i=1}^{3} \Phi_i^{d/a}. \tag{3.7}$$

The diabatic and adiabatic electronic populations of a given state are calculated by, [104]

$$\begin{aligned} P_i^d(t) &= \iiint_V (\psi_i^d(R,\Theta,Q_9,t))^* \psi_i^d(R,\Theta,Q_9,t)\, dR\, d\Theta\, dQ_9, i = 0,1,2 \\ P_i^a(t) &= \iiint_V (\psi_i^a(R,\Theta,Q_9,t))^* \psi_i^a(R,\Theta,Q_9,t)\, dR\, d\Theta\, dQ_9, i = 0,1,2 \end{aligned} \tag{3.8}$$

A laser field dependent cost functional, $J[E(t)]$, is constructed which includes the total flux Φ^d as the target and time-integrated intensity of the pulse (*i.e.* energy associated with the laser pulse). The target is the maximization of the total time accumulated flux with a simultaneous minimization of energy associated with the pulse. The cost functional for a laser pulse of duration *T* is given by

$$J[E(t)] = \Phi^d - \alpha_0 \int_0^T [E(t)]^2 dt. \tag{3.9}$$

In the above equation α_0 is a Lagrange multiplier which is independent of all laser parameters, designated as a penalty factor. For the present application, it is fixed at 0.001 a.u.. The functional in Eq.(3.9) is maximized using the GA (in particular micro-GA) subjected to the systems dynamics to follow the TDSE. [38, 105]

The mathematical construction of the laser pulse considered in this work is given by

$$E(t) = \{E_0 \sin \omega t\}.S(t), \tag{3.10}$$

where

$$S(t) = \begin{cases} \sin^2[\frac{\pi}{2}(\frac{t-t_0}{t_1-t_0})] & t_0 \le t \le t_1 \\ 1.0 & t_1 \le t \le t_2 \\ \sin^2[\frac{\pi}{2}(\frac{t_3-t}{t_3-t_2})] & t_2 \le t \le t_3 = T. \end{cases} \tag{3.11}$$

In Eq. 3.10 E_0 and ω are the amplitude and frequency of the pulse. The envelope

function $S(t)$ [cf., Eq. 4.13] determines the shape of the pulse by modulating t_0, t_1, t_2 and T, where $t_0 = 0 < t_1 \leq t_2 < t_3 = T$. The time period from t_0 to t_1 is the rise time of the pulse, t_2 to t_3, is the switch off period and in the intermediate section, t_1 to t_2, the envelop takes the value of unity giving rise to a plateau. The total time duration, T, of 30000 a.u. is considered. The optimal pulse shape is calculated using the GA based optimization method which gives the best combination of the four laser parameters *i.e.*, E_0, ω and two time parameters t_1 and t_2 to maximize $J[E(t)]$. We fixed a search space or parameter range [cf., Table 3.2] within which the GA finds the best solution.

Table 3.2: Laser parameter ranges for the optimization of the pulse by the GA.

Laser parameter	**Parameter range** [a.u.]
Amplitude, E_0	0.0-0.07
Frequency, ω	0.0536-0.1236
t_1	$0.2 \times T - T$
t_2	$T - 0.8 \times T$

GA is an adaptive heuristic search method for optimization of a function using the phenomenon of natural selection and principles of genetics. [105] In each of the generation in GA, a certain number, *N*, of individuals (a set of values of the parameters, here it is E_0, ω, t_1 and t_2) are randomly selected within the given parameter space [cf., Table 3.2]. The evaluation of these individuals are performed by calculating the cost functional $J[E(t)]$, the corresponding individual of the best value survives for the next generation. The elements of the natural selection process such as inheritance, mutation, selection, and crossover are included in the algorithm for the preparation of the individuals in the next generation. The values of the individuals are generated in binary numbers *i.e.* a string of 0s and 1s of a particular length (in our case 10) represents a possible value of a parameter set. A string of this binary numbers of all parameters is called a chromosome. In our work a chromosome is made up of length 40 with the 4 parameters stated above. The chromosome can have 2^{40} possible permutations of laser parameters.[80] GA finds out the best solution among these

possibilities.

3.3 RESULTS and DISCUSSION

3.3.1 Quantum dynamics within OCT framework

The vibrational wave function $|0,0,0\rangle$ of the diabatic ground electronic state is taken as the initial condition. It is excited to the $\pi\pi^*$ state by applying continuous pulse [cf., Fig. 3.5(a)] . The optimized frequency of the pulse determined from the GA is 17183 cm^{-1} (0.07829 a.u.) [cf., Fig. 3.5(b)]. The N-H dissociation process starts followed by the gradual $\pi\pi^*$ excitation and aided by the nonadiabatic transition through the two CIs (D_0/D_1 and D_1/D_2). Figs. 3.5(c) and 3.5(d) portray the time-dependence of diabatic and adiabatic electronic populations on the three electronic states during the action of the optimal pulse. Also the time accumulated fluxes at the asymptotes of three electronic states are calculated which show that almost entire dissociation occurs via the repulsive $\pi\sigma^*$ state [cf., Fig. 3.5(e)].

The $|0,0,0\rangle$ WP is gradually excited to the $\pi\pi^*$ state in the Franck-Condon (FC) region. It can be seen from fig. 3.5(c) that diabatic electronic population on the electronic ground state starts decreasing with an increase of the laser pulse amplitude [cf. fig. 3.5(a)]. Within $\sim$430 fs almost 90% of the ground state population is transferred to the $\pi\sigma^*$ state. The $\pi\pi^*$ state population increases up to $\sim$150 fs but due to the presence of D_1/D_2 CI, population flows to the $\pi\sigma^*$ state, and therefore, the population of the $\pi\pi^*$ state decreases. In case of adiabatic population [cf. fig. 3.5(d)], $\sim$40% of the ground state population initially (within 150 fs) transferred to the excited state but after $\sim$200 fs all the populations comes back to the asymptotic region of the adiabatic ground state via nonadiabatic passage of the WP through two successive CIs. It can be seen from the time accumulated flux plotted in fig. 3.5(e) that at the end of the optimal pulse duration $\sim$92% of the population arrives at the analysis surface in the asymptotic region of the $\pi\sigma^*$ state. The other dissociation channels

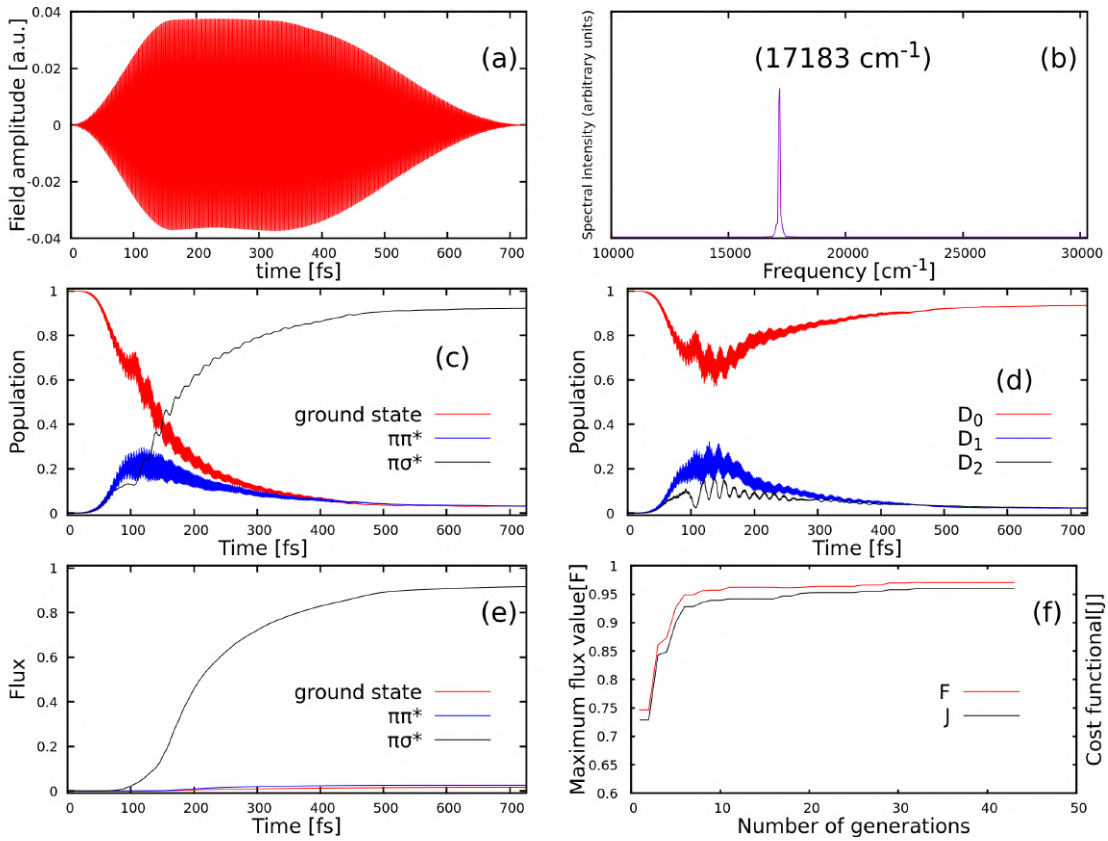

Figure 3.5: (0,0,0) initial condition: (a) to (f) are optimized pulse, frequency spectrum, adiabatic population dynamics, diabatic population dynamics, time-integrated flux and the convergence behaviour of cost functional (J) and total flux (F), respectively.

i.e. ground state and $\pi\pi^*$ state asymptotes remain inaccessible due to large energy difference in the asymptotic region of the PESs [cf., Fig. 3.2]. The frequency of the optimal pulse [cf., Fig. 3.5(b)] is 17183.0 cm^{-1} (2.13 eV) which is close to the $\pi\sigma^*$ excitation energy in the FC region.

The results of similar OCT calculations with three vibrationally excited WPs, $|0,0,1\rangle$, $|0,1,0\rangle$, $|0,1,1\rangle$ [cf., Fig. 3.4] as initial condition in the light driven dynamics are shown in Fig. 3.6. The diabatic populations of $|0,0,1\rangle$ WP show a similar time-dependence as $|0,0,0\rangle$ [cf., Fig. 3.6]. However, the ground state population decreases at somewhat faster rate than the latter case. This is because the initial WP has extra one quantum of energy along Q_9 mode, which assists the internal conversion (IC) between the $\pi\pi^*$ and $\pi\sigma^*$ state. A similar population dynamics is observed in case of $|0,1,1\rangle$ initial WP. Initial excitation

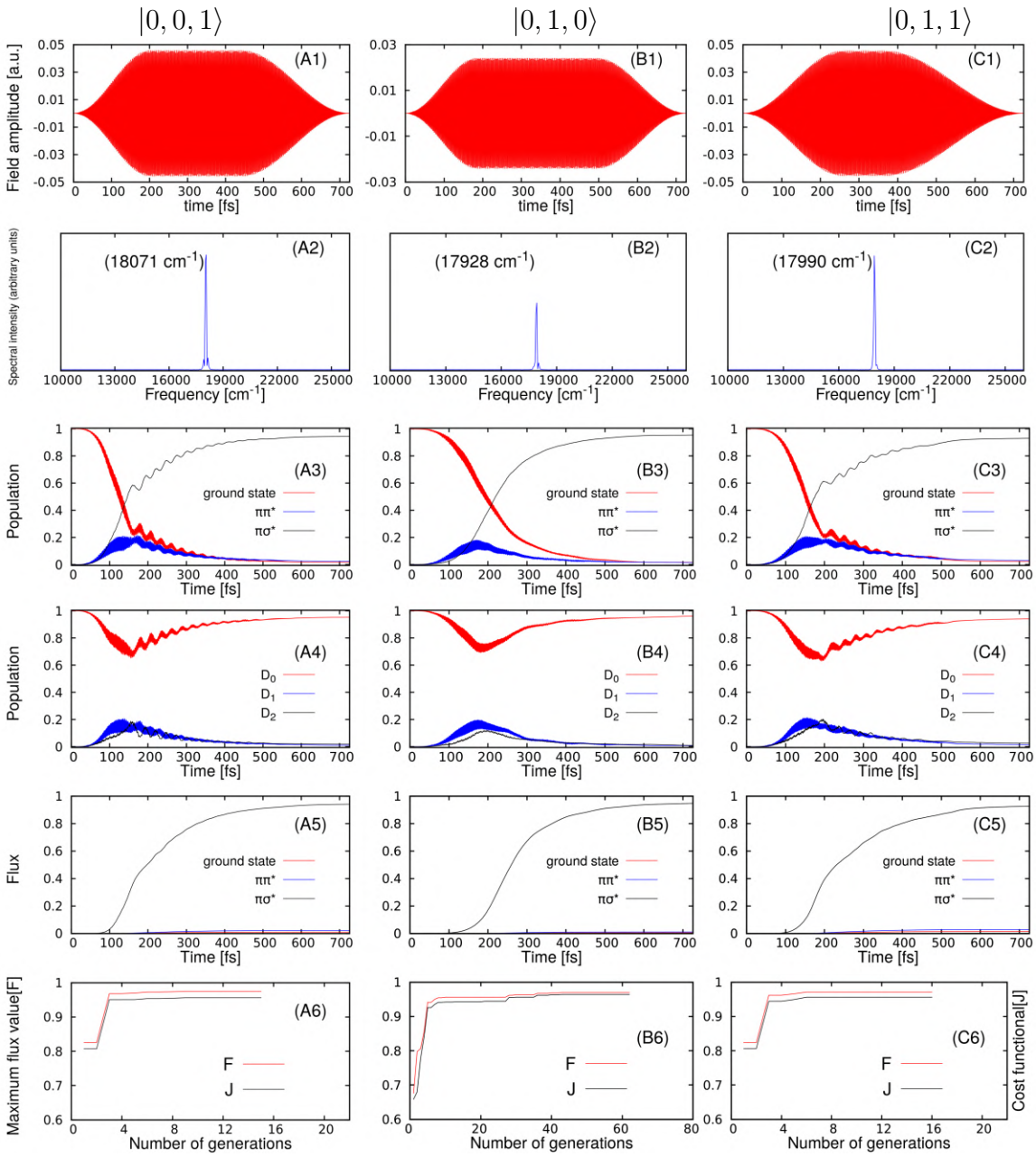

Figure 3.6: (A1,B1,C1) is the optimal laser pulse shape in time domain and (A2,B2,C2) is the carrier frequency of the pulse. (A3,B3,C3) and (A4,B4,C4) are the time dependent diabatic and adiabatic population dynamics on the ground, $\pi\pi^*$ and $\pi\sigma^*$ electronic states. (A5,B5,C5) is the dissociation yields through the three electronic state asymptotes. (A6,B6,C6) is the convergence behavior of the cost functional (J) and total-flux (F).

along the out-of-plane bending coordinate has an adverse effect in the dynamics. The ground state gets depopulated at a slower rate than in the $|0,0,0\rangle$ case and also gain in the $\pi\sigma$* state population is relatively smaller in the initial duration of the pulse. It seems that the out-of-plane bending motion of the H-atom, which has b_1 symmetry, does not assist the IC between the $\pi\pi$* ($2a_2$) and $\pi\sigma$* ($12a_1$) states because $a_2 \otimes b_1 \otimes a_1 (\not\supseteq a_1)$ does not satisfy the symmetry selection rule.[92] The optimal pulses are quite different for different initial conditions. These pulses are obtained starting from the same shape of pulse as the initial guess in the GA. From the frequency spectrum [cf. (A2,B2,C2) in Fig. 3.6] it is clear that all pulses have a well defined frequency. For all initial conditions the dissociation yields through the three channels are almost similar to $|0,0,0\rangle$ condition. In all cases only $\pi\sigma$* dissociation channel gets activated. This is because in the asymptotic region, the energy difference between $\pi\sigma$* asymptote and the other excited state asymptotes is larger than the energy associated with the pulses. Therefore, the branching ratios are almost the same in each case. However, there is a difference in the dissociation yield during the early time (≤ 250.0 fs) of the pulses. For the $|0,0,1\rangle$ and $|0,1,1\rangle$ initial conditions the dissociation starts somewhat earlier than the $|0,1,0\rangle$ case.

The three panels (A6,B6,C6) of fig. 3.6, represents the convergence behavior of the cost functional (*J*) and the total dissociation yield (*F*) with respect to the number of generations. In all cases the *J* and *F* increases with the number of generations passed in the GA until it converges to the maximum value. For all initial conditions the maximum value of these quantities is almost same and the achieved dissociation yields are more than 90%. In all cases the GA gives a good convergence behavior.

OCT calculations are also performed with a 200 fs pulse. Fig. 3.7 portrays the results of the OCT calculations using the GA where (0,0,0) vibrational wave function of ground electronic state was used as the initial condition to solve the TDSE. The diabatic electronic population dynamics in panel (c) shows that ground electronic state population decreases more rapidly than in the previous case [cf. Fig., 3.5]. In this case the ground electronic state

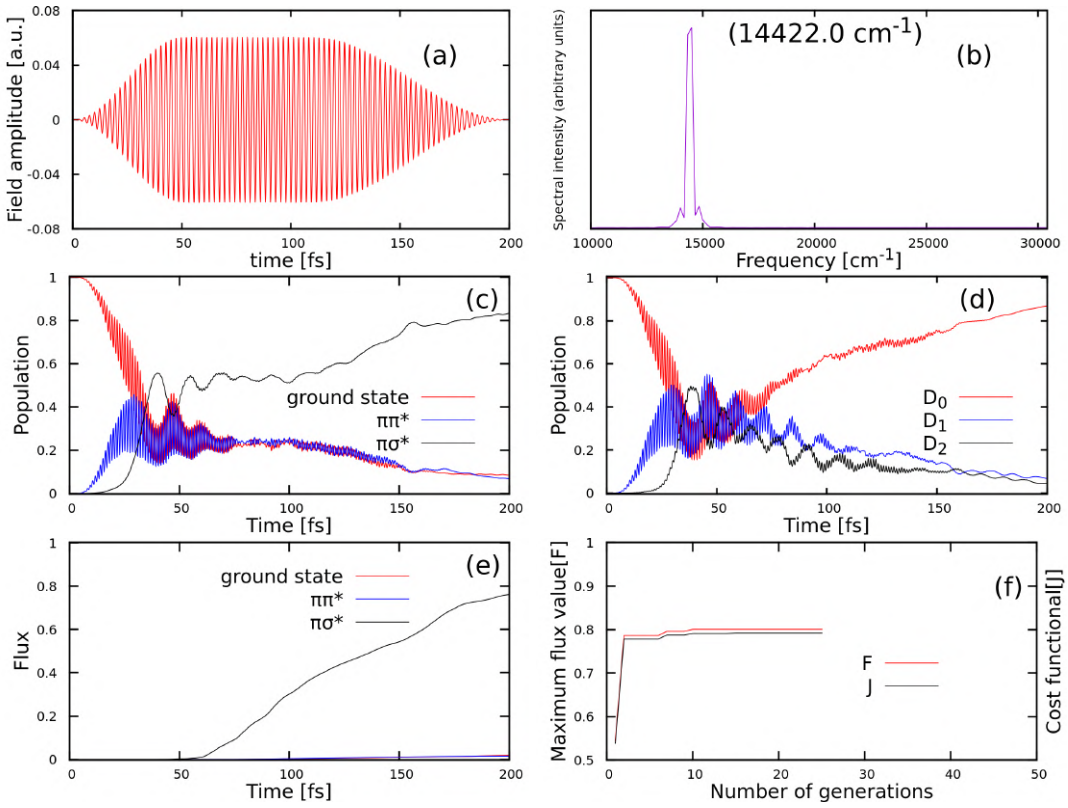

Figure 3.7: (0,0,0) initial condition : (a) to (f) are diabatic population dynamics, adiabatic population dynamics, optimal laser pulse, frequency spectrum and time-integrated flux and the convergence behaviour of cost functional (J) and total flux (F), respectively.

population decreases by 80% within ∼40 fs. The $\pi\pi^*$ state population initially increases but after reaching a maximum it starts decreasing. From 40 to 200 fs the diabatic populations of the ground and $\pi\pi^*$ electronic state remain same. The $\pi\sigma^*$ state population monotonically increases starting from ∼20 fs. The adiabatic electronic populations shown in panel (d) reveals that the D_0 state population decreases initially as in the diabatic case but after 45 fs it starts regaining the population in the asymptotic region. The D_1 and D_2 state population reveals a similar trend as the $\pi\pi^*$ and $\pi\sigma^*$ state population in the diabatic picture [cf., Fig. (c)]. However, after 45 fs it starts decreasing gradually. This implies that after crossing the two CIs the population is accumulated in the adiabatic asymptote of the ground state *i.e.* the asymptotic region of the diabatic $\pi\sigma^*$ state only. Therefore, it appears that the $\pi\sigma^*$ channel is the only active channel for dissociation [cf., Fig. 3.7(e)].

In fig. 3.8, the outcomes of optimal control of the N-H photodissociation using different

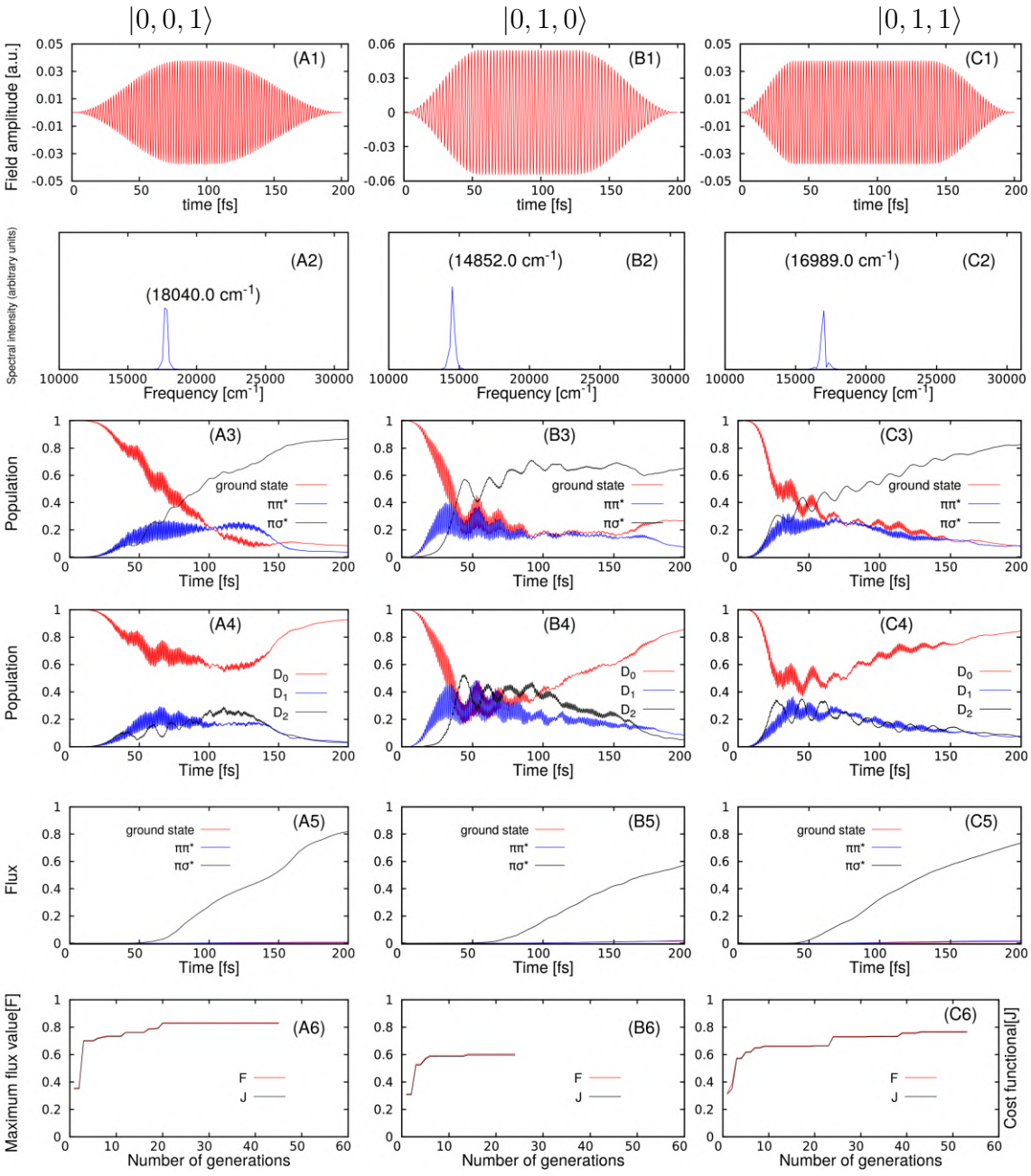

Figure 3.8: (A1,B1,C1) are the optimized pulse shape in the time domain. (A2,B2,C2) are the corresponding carrier frequency of the optimal pulse. (A3,B3,C3) and (A4,B4,C4) are the diabatic and adiabatic population dynamics w.r.t. time on the ground, $\pi\pi$ and $\pi\sigma^*$ states. (A5,B5,C5) are the dissociation yields through the three channels. (A6,B6,C6) are the convergence behavior of the cost functional (J) and total-flux (F).

vibrational wave functions as the initial condition for the TDSE are shown. Each column of this figure portrays the results for a given initial condition mentioned on the top of the column. The (A1,B1,C1) panel represents the optimal pulses obtained from the OCT calculations with the respective initial conditions and (A2,B2,C2) panel shows the corresponding frequency spectrum of those pulses. From the diabatic population plots (A3,B3,C3), it is clear that the quantum dynamics on the three states are not similar to the dynamics in the case of pulses of long duration and also the effect of initial vibrational excitation is recognizable. For the $|0,0,1\rangle$ initial condition the diabatic population of the ground state decreases at a slower rate than the $|0,0,0\rangle$ case whereas, for $|0,1,0\rangle$ and $|0,1,1\rangle$ case it is quite similar. The $\pi\pi^*$ state population initially increases in all the cases, but in the $|0,1,0\rangle$ case it increases rapidly, then decreases gradually. The $\pi\sigma^*$ state population increases to a value greater than 80% for $|0,0,1\rangle$ and $|0,1,1\rangle$ initial conditions but not in the case for $|0,1,0\rangle$. Here again we get the signature of IC between $\pi\pi^*$ and $\pi\sigma^*$ state and its effect is more prominent than the dynamics with the long time pulse and the excitation along out-of-plane bending coordinate quenches the IC. In the adiabatic population [cf., Figs. (A4,B4,C4)] the ground adiabatic state loses population because of FC excitation in the initial time but in the asymptotic region it is regained through quantum tunneling and nonadiabatic transitions through two CIs. The consequences are reflected in the flux profile [cf., Figs. (A5,B5,C5)], where it is clear that for the $|0,1,0\rangle$ initial condition the time accumulated flux at 200 fs through the $\pi\sigma^*$ asymptote ($\sim$58%) is quite smaller than the other cases ($\sim$81% and $\sim$73% for $|0,0,1\rangle$ and $|0,1,1\rangle$ cases, respectively). It seems that the initial excitation along out-of-plane bending mode inhibits the dissociation process. The similar effect was also observed in the quantum dynamics study without laser field.[92] Finally, the effect of initial condition on the dissociation yields is more prominent in case of 200 fs laser pulse than the 726 fs one.

3.3.2 Time-dependent probability densities

In order to get more detailed insights of the pulse driven dynamics we examined the snapshots of the nuclear WP components on the three diabatic PESs at different times shown in Figs. 3.9 and 3.10. The ground, $\pi\pi^*$ and $\pi\sigma^*$ components of the WP are projected from the 3-dimensional picture to the reduced dimension using the following equations, respectively,

$$\begin{aligned} P_{RQ_9}(R, Q_9) &= \int \psi(R, \Theta, Q_9)^* \psi(R, \Theta, Q_9)\, d\Theta, \\ P_{R\Theta}(R, \Theta) &= \int \psi(R, \Theta, Q_9)^* \psi(R, \Theta, Q_9)\, dQ_9. \end{aligned} \tag{3.12}$$

Fig. 3.9 depicts the WP snapshots in $R - Q_9$ space. The optimal laser pulse takes the ground state WP to the $\pi\pi^*$ state and to the $\pi\sigma^*$ state [cf., A1 in Fig. 3.6]. The initial WP has one node along the Q_9 mode which is retained for ground and $\pi\pi^*$ state components of WP but in the $\pi\sigma^*$ state the nodal line disappears [see Fig. 3.9 c(2) -c(4)]. At 36.5 fs almost all the WP density is accumulated in the FC region of the ground state. After $\sim$73 fs the $\pi\pi^*$ and $\pi\sigma^*$ state starts gaining population. As time progresses the $\pi\sigma^*$ state acquires more population due to the action of the plateau region (highest amplitude region) of the pulse. The $\pi\sigma^*$ WP rapidly extends to large NH distances owing to strongly repulsive nature of the $\pi\sigma^*$ PES [cf., Fig. 3.9 c(3)]. The snapshot at $\sim$146 fs shows an interesting phenomena that a node appears in the $\pi\pi^*$ and $\pi\sigma^*$ components of the WP along *R*. This is because of the vibrational excitation in the FC region of the $\pi\pi^*$ state component of the WP. This vibrationally excited WP can access the $\pi\sigma^*$ state via IC through CIs.

In Fig. 3.10 the same probability densities as discussed above are plotted in the $R - \Theta$ plane. It can be seen that the diabatic ground state WP has zero excitation along Θ and *R* coordinates. The $\pi\pi^*$ and $\pi\sigma^*$ state components of the WP acquires larger amplitudes from the ground state due to continuous excitation by the optimal pulse in time. Similarly at $\sim$ 146 fs a nodal pattern in the $\pi\pi^*$ and $\pi\sigma^*$ components of the WP along *R* coordinate

appears because of vibrational excitation. Subsequently, the IC promotes it to the $\pi\sigma^*$ state. Similarly, the $\pi\sigma^*$ component of the WP reaches the dissociation limit rapidly due to the repulsive nature of the $\pi\sigma^*$ PES.

The energy of the optimal pulse [cf., (A2,B2,C2) in Fig. 3.6] is not enough for the system to cross the barrier energy in the $\pi\sigma^*$ state ($\sim$0.2 eV). Thus after excitation, the WP reaches the asymptote due to quantum tunneling, [106] this is evident from the snapshots C(1) to C(4) of Fig. 3.9 and 3.10. The two CIs are located in the barrier region of $\pi\sigma^*$ PES (cf., Fig. 3.2), therefore the nonadiabatic transition through these two CIs occurs because of the tunneling process.[107] WP dynamics on the $\pi\sigma^*$ state without the external electromagnetic field leads to a considerable amount of nonadiabatic transition through two CIs.[92] But in the presence of the optimal pulse nonadiabatic transitions seldom occurs which indicates that the pulse promotes the tunneling process rather than the nonadiabatic transitions so that it achieves the maximum amount of photodissociated product in the ground state. From 73 to 146 fs, $\pi\sigma^*$ component of the WP oscillates in the upper cone of the D_0/D_2 CI [cf., Fig. 3.9 c(2)-c(4), 3.10 c(2)-c(4)]. Each time it passes the region of the CI, a fraction comes back to the ground adiabatic surface and dissociates to the ground state of pyridine. This explains the recovery of adiabatic population of ground state after 200 fs (see (A3) in Fig. 3.6).

3.3.3 Probability densities for $|0,0,0\rangle$ condition with 200 fs pulse

Figures 3.11 and 3.12 display the snapshots of the probability densities in $R-\Theta$ and $R-Q_9$ space at each $\sim$ 40 fs time interval for $|0,0,0\rangle$ initial WP, respectively. The ground and $\pi\pi^*$ WP components predominantly remain in the FC region in the early period of evolution. In the $\pi\sigma^*$ state the WP rapidly extends to the asymptotic region. Unlike the previous 726.0 fs pulse driven dynamics, with an increase of time multiple nodes along *R* coordinate appears in the ground and $\pi\pi^*$ WPs and extends to the CIs. In other words, this short time UV pulse excites the components of lower electronic energy to their higher vibrational levels, reflecting the large excess energy in the NH stretching motion. This

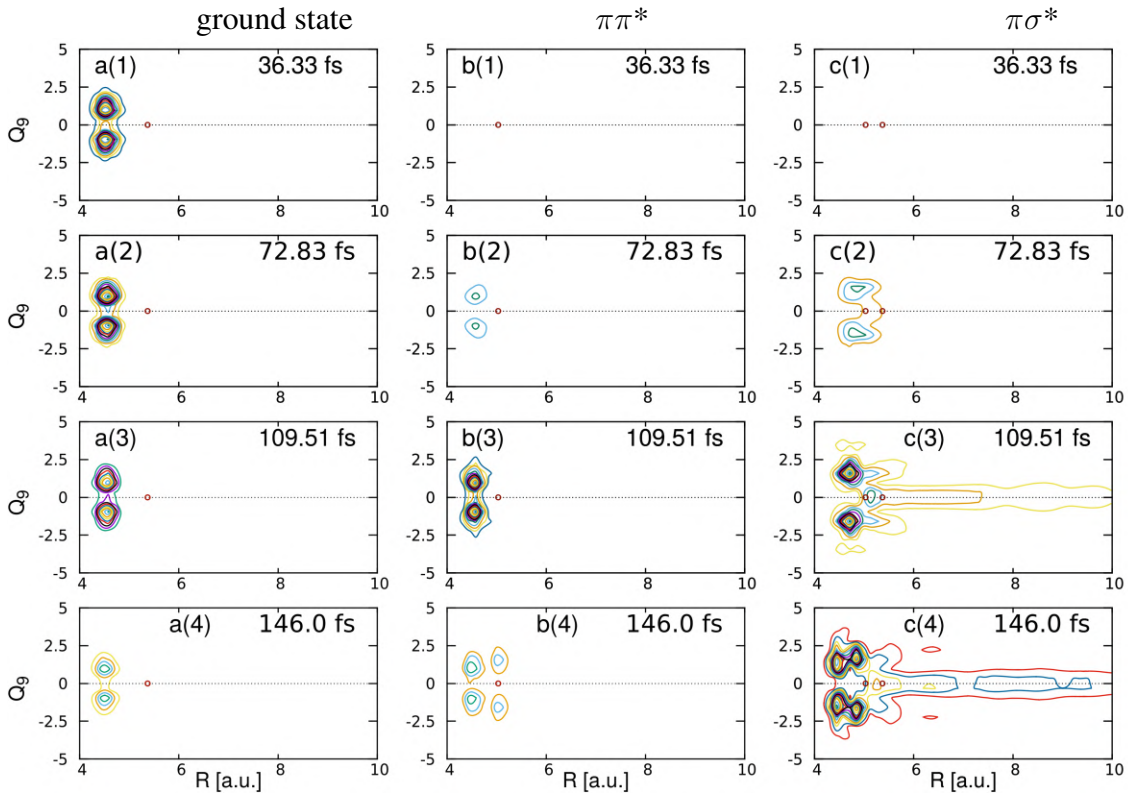

Figure 3.9: Snapshots of the probability density of the WP components on the diabatic ground state, $\pi\pi^*$ and $\pi\sigma^*$ states in $R - Q_9$ plane at different times in the pulse driven dynamics of the $|0, 0, 1\rangle$ initial condition.

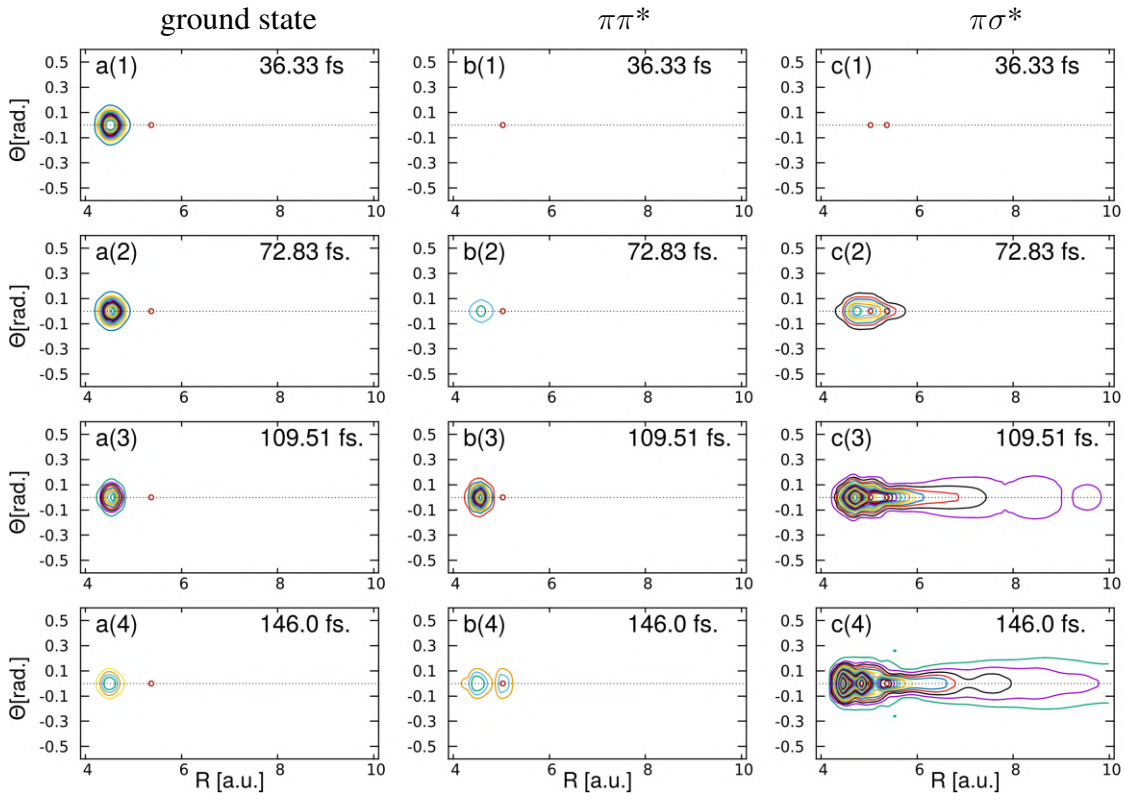

Figure 3.10: Snapshots of the probability density of the WP components on the diabatic ground state, $\pi\pi^*$ and $\pi\sigma^*$ states in $R - \Theta$ space at different times in the pulse driven dynamics of $|0, 0, 1\rangle$ initial condition.

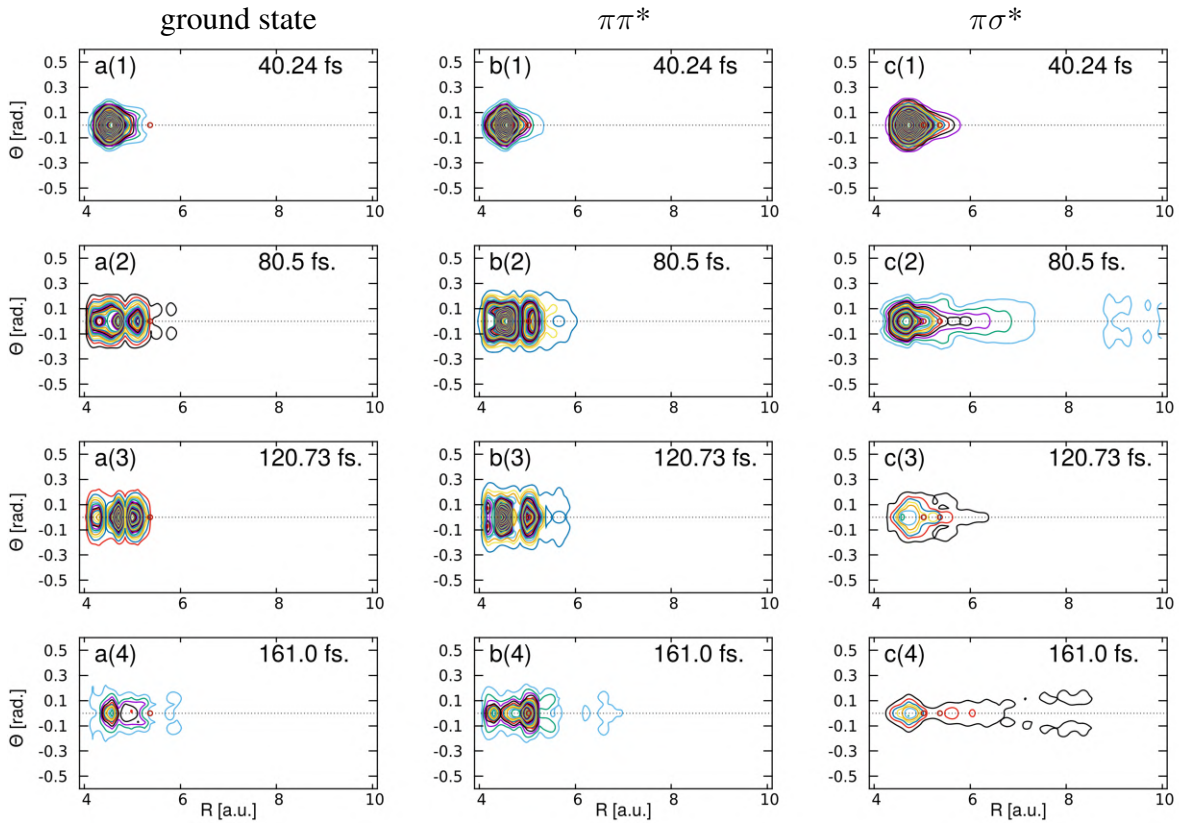

Figure 3.11: Snapshots of the probability density of the WP components on the diabatic ground state, $\pi\pi^*$ and $\pi\sigma^*$ states in $R - \Theta$ space at different times in the pulse driven dynamics of $|0, 0, 0\rangle$ initial condition.

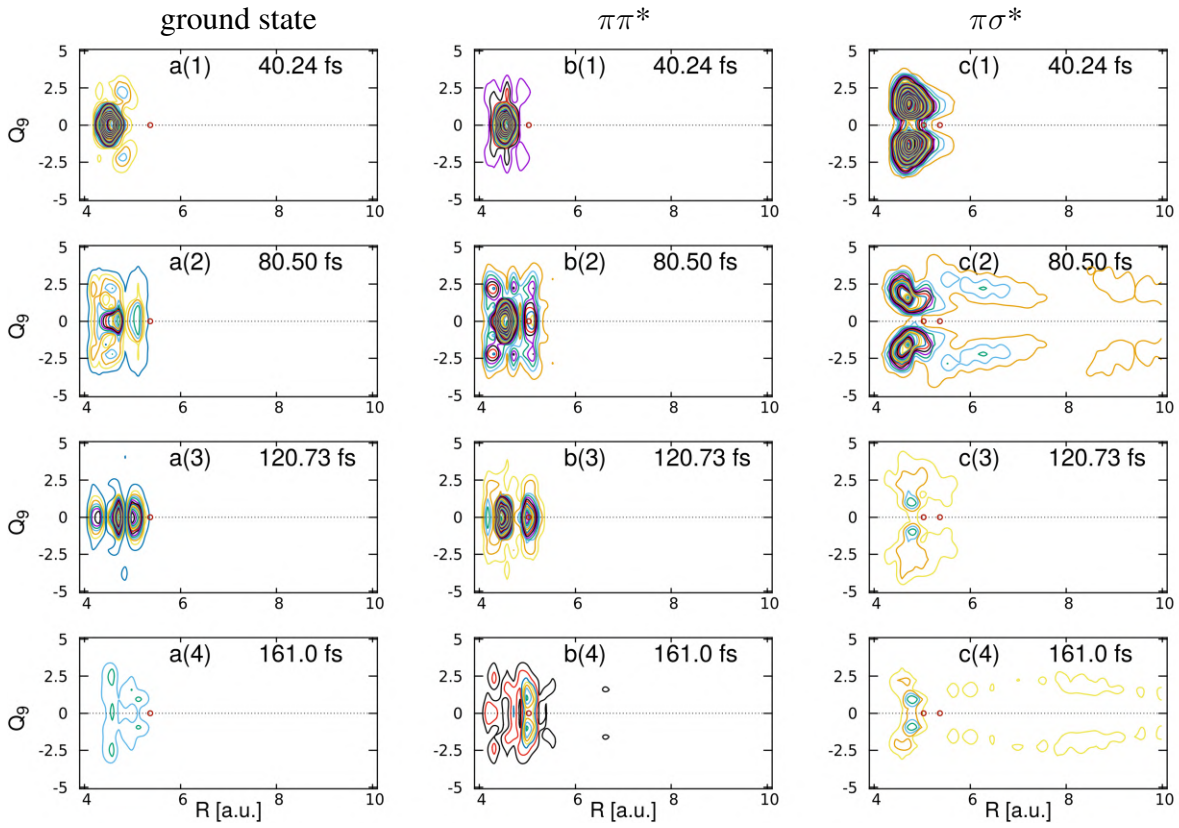

Figure 3.12: Snapshots of the probability density of the WP components on the diabatic ground state, $\pi\pi^*$ and $\pi\sigma^*$ states in $R - Q_9$ space at different times in the pulse driven dynamics of $|0, 0, 0\rangle$ initial condition.

indicates that the molecule in a highly vibrationally excited quasistationary state in the ground and $\pi\pi^*$ PESs is accessing the CIs which eventually leads to the IC to the $\pi\sigma^*$ state. [108] The plots of the probability densities on the $\pi\sigma^*$ state in $R - Q_9$ space exhibit an interesting feature of the nonadiabatic WP dynamics. In all the snapshots, there is a nodal line at Q_9=0. This appears due the fact that the diabatic coupling term is an odd function of the coupling coordinate Q_9.[73, 109, 110]

3.4 Summarizing Remarks

In summary, optimal laser pulses are constructed to control the N-H photodissociation dynamics of the pyridinyl radical. The $|0,0,0\rangle$, $|0,0,1\rangle$, $|0,1,0\rangle$ and $|0,1,1\rangle$ vibrational wave functions of the ground electronic state were considered as the initial conditions in the OCT calculations to study the effect of vibrational pre-excitation along the coupling coordinates on the dissociation yield or the branching ratios. For all the initial conditions, the N-H dissociation yield in the $\pi\sigma^*$ asymptote is greater than 95%. It is due to the fact that the energy range considered for the optimization of the UV laser pulse using GA is lower than the the energy difference between the ground state and the two excited states in the dissociation limit. The initial WP is excited from ground state to some vibrational state of $\pi\pi^*$ state in FC region by the laser pulses created in each of the generation of the present optimization scheme. Once the vibrational state of energy greater or equal to the D_1/D_2 CI is achieved, almost all the population leads to the dissociation product through the $\pi\sigma^*$ asymptote owing to the topography of the PESs as depicted in Fig. 2 and 3. Moreover, different vibrational wave functions of the ground state is subjected to same initial guess laser fields generated by the GA and converged to different optimal laser pulses. This study gives us a detail information about the N-H photodissociation mechanism through two successive CIs present in $\pi\sigma^*$ state. As those initial wave functions are of different parity (even or odd with respect to the three coordinates)[cf., Fig. 3.4], it reveals

the behavior of the WP near the two CIs and its impact on the photodissociation. In case of 726 fs laser pulse the dependence of time-integrated flux on the initial vibrational state is observed within the propagation time $\leq$ 250.0 fs. The θ and Q_9 excitation hinders the nonadiabatic transition through D_1/D_2 and D_0/D_1 CIs, respectively, and reflects back to the equilibrium region of the $\pi\pi^*$ state. This reflected part of the population eventually reaches to the dissociation generally by two processes, viz., (1) the re-excitation by the laser pulse followed by nonadiabatic transition and (2) IVR to avoid the CI [95]. In case of 726 fs dynamics, the system gets enough time to go through these two processes and at the end almost all excited population leads to the dissociation. Whereas, in 200 fs dynamics it is not possible. Therefore, the total dissociation yield for 726 fs dynamics is almost unaffected due to initial vibrational state of the WP however in the case of 200 fs the effect is noteworthy [cf., table 3.3].

We have designed the optimal pulse shape with a motivation to maximize the dissociation yield. To achieve the goal we adopted a sophisticated and stochastic search optimization algorithm, the GA. The frequencies obtained from the optimization calculations are almost near the resonance energy for the $\pi\sigma^*$ excitation. The frequency spectrum of the optimal pulses show sharp peaks at a particular frequency for 726 and 967.55 fs pulse duration but for 200 fs pulse the peaks are quiet broader. The amplitude of the 200 fs pulse is much larger than the others.

The optimal laser pulses are computed for different duration like 200, 726 and 967.55 fs. It is observed that the dissociation yields are dependent on the duration of the laser pulse for all the initial conditions. Therefore, the total time of the laser pulse can be one of the parameters to be optimized beside the frequency, amplitude and shape. Because of the two CIs situated very near to the FC region and large energy difference in the asymptotic region, a laser pulse with time-dependent frequency, viz. chirped pulse, can be a possible alternative of a single frequency laser pulse. [111, 112] A laser pulse consisting of multiple components of different frequencies and relative phase differences can also be an extension

Table 3.3: The results of the OCT calculations with $|0,0,0\rangle, |0,0,1\rangle, |0,1,0\rangle, |0,1,1\rangle$ initial conditions for pulse duration of 250.0, 726.0 and 967.55 fs.

Initial condition	**Cost functional(J)**	**Total flux(F)**	E_{max} $[a.u.]$
Pulse duration: 250 fs			
$\|0,0,0\rangle$	0.79	0.80	6.02970×10^{-2}
$\|0,0,1\rangle$	0.83	0.83	3.75681×10^{-2}
$\|0,1,0\rangle$	0.60	0.60	5.4322×10^{-2}
$\|0,1,1\rangle$	0.76	0.77	3.75681×10^{-2}
Pulse duration: 726 fs			
$\|0,0,0\rangle$	0.96	0.97	3.75681×10^{-2}
$\|0,0,1\rangle$	0.95	0.97	4.61935×10^{-2}
$\|0,1,0\rangle$	0.96	1.0	2.42598×10^{-2}
$\|0,1,1\rangle$	0.96	0.97	4.57441×10^{-2}
Pulse duration: 967.55 fs			
$\|0,0,0\rangle$	0.94	0.96	4.26249×10^{-2}
$\|0,0,1\rangle$	0.97	0.98	4.02926×10^{-2}
$\|0,1,0\rangle$	0.96	0.98	3.78218×10^{-2}
$\|0,1,1\rangle$	0.95	0.97	4.46835×10^{-2}

of this work. For further development, the other coupling coordinates can be added to better understand the IC mechanism at the two CIs.

CHAPTER 4

Control of optically dark nσ* state mediated photodissociation of thioanisole

4.1 Introduction

The photochemistry of bio-active aromatic molecules is important because these molecules are an ideal model system for investigating the photobiological and photochemical reactions in nature. Thioanisole molecule contains an aromatic ring and a hetero atom, S. The photoexcitation of thianisole molecule at 289.8 nm wavelength leads to photodisssociation of S-CH_3 bond following $\pi\pi$* excitation [113]. This process occurs on the repulsive nσ* state which conically intersects with the $\pi\pi$* state and the ground electronic state[64]. Due to the nonadiabatic transitions through two successive CIs the molecule can access the optically dark nσ* state. The energy splitting between the ground and first excited state after the S_0/S_1 CI, i.e., in the asymptotic region is very small ($\sim$ 300 cm^{-1})[114]. Therefore, thioanisole can dissociate by these two channels and can produce two types of products (1) ground doublet states of both radicals, PhS[D_0] + CH_3[D_0], (2) excited thiophenoxyl radical and ground-state methyl radical, PhS[D_1] + CH_3[D_0] [115]. In the S-CH_3 bond

dissociation dynamics of thioanisole molecule a passage through CIs plays a significant role.[116] This nonadiabatic photoinduced dissociation of thioanisole is investigated here by the time-dependent WP method.

Lim et. al. have investigated the methyl photodissociation of thioaniole in the gas phase.[115] They have monitored the dissociation yield as a function of photoexcitation energy to give the photofragment excitation (PHOFEX) spectrum. Moreover, in this experimental work the S_1/S_2 CI was probed and the nσ* mediated photodissociation mechanism was proposed. An interesting result observed in this experimental work was that the presence of dynamic resonances in the photodissociation of thoanisole. This reveals that the branching ratio of the two different channels change dramatically for the internal energy of $\sim$722 cm^{-1}. Roberts et. al. have investigated experimentally more exotic phenomena involved in nσ* mediated dynamics of thioanisole photodisssociation.[113] From this experimental study it was found that the nonadiabatic photochemistry through CIs can be manipulated with 'vibration-specific control'. Moreover, the mechanism of the S-CH_3 bond fission via nσ* following excitation to the $\pi\pi$* state is also established. The nuclear framework evolves to the larger ϕ (torsional angle) range where the barrier associated with the S_1/S_2 CI is smaller than the planer geometry, i.e., at ϕ = 0. The photodissociation dynamics of thioanisole was further studied by Woo et. al. where nonadiabtic bifurcation dynamics at CIs between ground and nσ* states is observed and also it was established that the adiabatic and nonadiabatic dissociation pathways can coexist in the vicinity of CIs.[117, 118] The S_1/S_2 CI was further characterized for deuterated thioanisole (C_6H_5S-CD_3) in multi-dimensional space of normal modes.[119, 120, 121] The experimental results revealed that the branching ratio is not only enhanced by the excitation of 7a mode (the C–S–CH_3 asymmetric stretching mode), there are another three modes like S–CD_3 symmetric stretching, CD_3 bending, and a defined mixed mode is also responsible for the enhancement of the branching ratio for the deuterated thioanisole molecule.

The analytic full-dimensional potential energy surfaces and the interstate couplings of

the three lowest singlet states were reported by Li and Truhlar, where an improved anchor points reactive potential (APRP) method was employed to construct the diabatic potential energy matrix.[64] The ab initio energies were calculated by extended multi-configurational quasi-degenerate perturbation theory (XMC-QDPT) followed by the fourfold way and model space diabatization, with a mixed, minimally augmented basis set of 6-311+G(d) for carbon and hydrogen and MG3S for sulfur. The potential energy matrix was further improved by Shu and Truhlar.[122] Li et. al. have investigated theoretically the nonadiabatic dynamics of methyl dissociation of the thioanisole molecule in a three dimensional space. Their findings suggest that the photodissociation of low-lying S_1 vibronic levels are not merely nonadiabatic but also the heavy atom tunneling plays a very important role in the dissociation dynamics.[116]

In the past decades there is a keen interest to develop in the OCT framework to deal with the chemical processes like, photodissociation, photoinduced intramolecular H-transfer, and *cis*-trans photoisomerisation, by trained laser pulse(s).[10, 11, 16, 21, 83, 84, 85, 86] Due to coherent character of the laser, it became a promising external controller of photoinduced chemical processes. The evolution of the molecular system towards a desired target state can be achieved by obtaining the best combination of the laser parameters viz., frequency, amplitude, shape, duration of the pulse, and delay time between pump-dump pulses. [80, 87, 88]

In the present study, the nonadiabatic dynamics of the photodissociation is carried out within the mathematical framework of OCT where the optimization is done using the GA. The calculations are performed with a target for the maximization of the photodissociation yield through two channels (i.e. the nσ* and ground state in diabatic representation) in accordance with the TDSE with different initial conditions. In the OCT calculations a monochromatic laser pulse is employed as the external controller of the present photodissociation dynamics. The parameter space is comprised of amplitude, carrier frequency and two shape parameters of the laser pulse. The cost functional for the optimization is

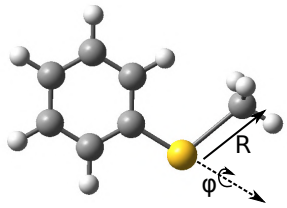

Figure 4.1: Schematic diagram of the reaction coordinate, R, and the coupling coordinate, ϕ of thioanisole.

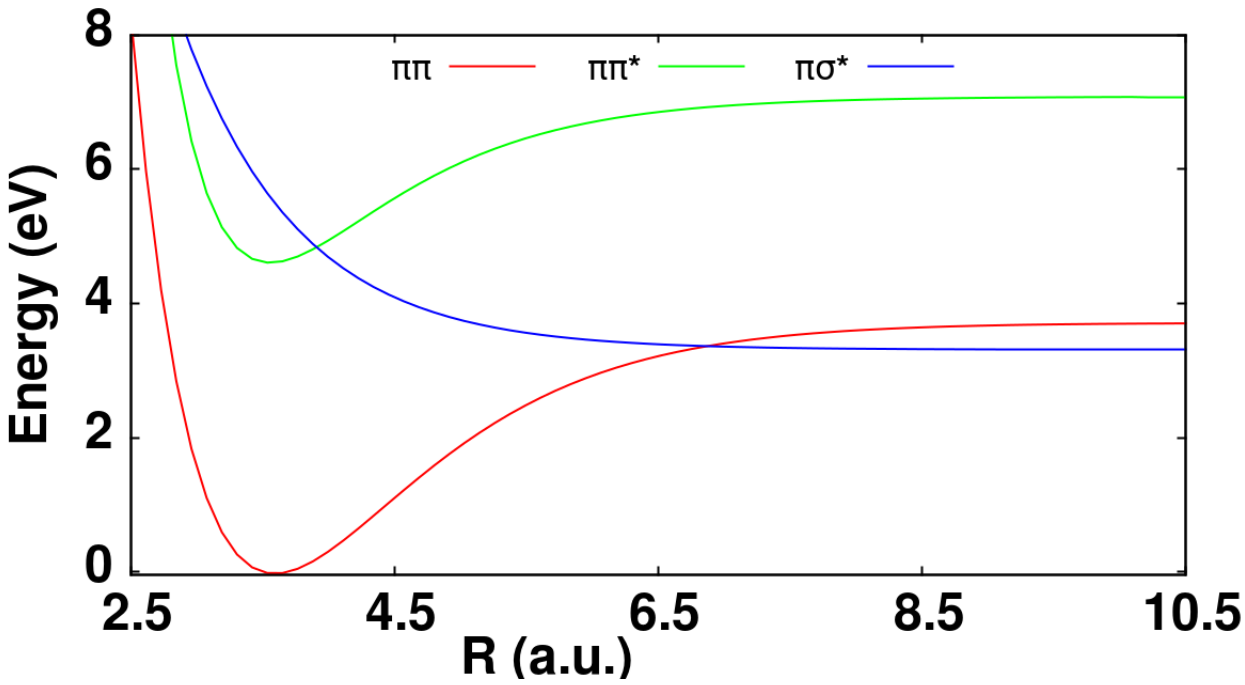

Figure 4.2: Diabatic potential energy is plotted along the S-C stretching coordinate, R.

constructed in such a way that the GA maximizes the dissociation yield but at the cost of minimum fluence associated with the laser pulse. These attributes of the cost functional lead to the maximization of the nonadiabatic transition through CIs. To justify the results of the OCT calculations, the initial WPs were prepared in the FC region of $\pi\pi^*$ state by delta excitation and allowed to evolve for a duration of 40000 a.u. A comparison between the photodissociation dynamics in presence and in absence of optimal laser pulse is elaborately discussed in the rest of the article.

4.2 Theory and Methodology

4.2.1 Model Hamiltonian

In this work, a three-states and two-modes model Hamiltonian is employed. From the findings of the experimental work performed by Lim et. al. and Roberts et. al. it is found that among the all 42 internal modes only two modes, the S-CH_3 stretching coordinate and CCSC dihedral angle, are the most important coordinates[113, 115] and they are employed in the present study [see Ref. 64]. For the calculation of diabatic potential energy surface, single-point energy calculation was performed along these two coordinates. This indicates that the methyl group is moved along these coordinates without any change of C-H bond lengths or the relative angles associated with the methyl group. Hence, for the sake of simplicity of molecular Hamiltonian the methyl group is considered as a composite atom whose total mass is centered at the center-of-mass. The distance between the S-atom and the composite atom is considered as the reaction coordinate and it is denoted as ***R***. The relation between ***R*** and the S-CH_3 bond length, r_{SC}, is given by $R = r_{SC} + 0.14$ a.u. (cf. Fig. 4.1) where the extra 0.14 a.u. is the distance between the C-atom of methyl group and its center-of-mass along S-CH_3 bond. The antisymmetric coordinate CCSC dihedral angle is taken as the coupling coordinate which is defined as ϕ (cf. Fig. 4.1). The three electronic states are labeled as $\pi\pi$ (ground state), $\pi\pi^*$ and nσ^* in diabatic electronic representation (cf. Fig. 4.2) and S_0, S_1 and S_2 in the adiabatic electronic representation.

To study the CH_3 photodissociation of thioanisole molecule a 2D model Hamiltonian in the three-states diabatic electronic basis is considered. The Hamiltonian reads as

$$\boldsymbol{H} = \boldsymbol{T} + \boldsymbol{V} = T_N \begin{pmatrix} 1 & 0 & 0 \\ 0 & 1 & 0 \\ 0 & 0 & 1 \end{pmatrix} + \begin{pmatrix} V_{00} & V_{01} & V_{02} \\ V_{10} & V_{11} & V_{12} \\ V_{20} & V_{21} & V_{22} \end{pmatrix}. \tag{4.1}$$

V_{11}, V_{22} and V_{33} are the PESs of the diabatic $\pi\pi$, $\pi\pi$* and nσ* states, respectively (see panel (a) in Fig. 4.3). The off-diagonal elements represent the electronic couplings between the respective diabatic states (see panel (b,c,d) in Fig. 4.3). The diabatic potential energy matrix is given in Ref. 64 and its improved versions is available in Ref. 122. In the present work the version III of the diabatic potential energy matrix of Ref. 122 is employed. The key advantage of this potential energy model is that the predicted geometry of the S_1/S_2 CI aligns well with experimental observations.[117] In contrast, other versions of the potential energy matrix, presented in Ref. 122, were generated by manually adjusting a single parameter (D_3) in the nσ* surface to shift the position of the S_1/S_2 CI. Although the surface hopping calculation with these modified potential surfaces predict $\pi\pi$* state lifetimes close to the experimental results,[113, 117] the predicted S_1/S_2 CI geometry from these modified potential surfaces deviates from the geometry found from experiment considerably.[115] The S_1/S_2 CI geometry obtained from potential energy surface constructed by Li et. al. also agrees with the version III of potential energy matrix.[116] Xu et. al. revisited this problem implementing a neural network based complex scaling (NN-SC) method to determine the two dimensional potential energy surface for the calculation of resonance eigenvalues and their work suggests that the lifetimes of the vibronic resonances are in good agreement with the experimental results.[123] Therefore, it can be concluded that the lifetime of the $\pi\pi$* state of thioanisole is quite sensitive to the S_1/S_2 CI barrier as well as involvement of some other mode like C-S-CH_3 angle. Moreover, thioanisole molecule is a geometrically analogous to phenol and to account the O-H photodissociation of phenol a two dimensional model (the two modes are O-H bond distance and CCOH dihedral angle) is found to be quite sufficient as implemented in the work of Lan et. al.[73] The validity of the two dimensional model for phenol was further confirmed by Xie et. al. where they found the O-H vibrational and the CCOH torsional modes have the largest overlaps with the g and h vectors, the energy gradient and coupling gradient vectors, at the minimum energy CI.[106] Hence, in the present study, the two dimensional model Hamiltonian is considered and it is found to

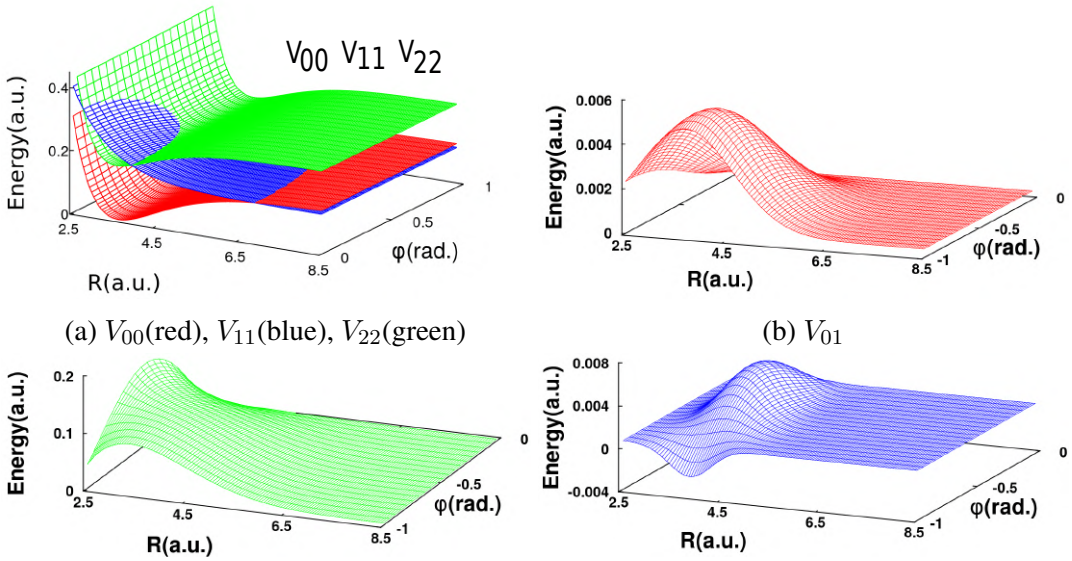

(a) V_{00}(red), V_{11}(blue), V_{22}(green)

(b) V_{01}

(c) V_{02}

(d) V_{12}

Figure 4.3: (a) Diabatic potential energy surfaces in (R,ϕ) space where V_{00}, V_{11}, and V_{22} represents the ground, $\pi\pi$*, and nσ* state, respectively, (b,c,d) the inter-state diabatic coupling surfaces.

be quite efficient to get a primary insight of the methyl photodissociation mechanism of thioanisole. Although, the two dimensional model does not reproduce the lifetimes, the dissociation dynamics remains invariant in presence of optimal pulse.

In Eq. 4.1, T_N represents the kinetic-energy operator. The KE operator in the two dimensional space (R, ϕ) in atomic units reads ($\hbar = 1$)

$$T_N = -\frac{1}{2\mu_{S(CH_3)}}\frac{\partial^2}{\partial R^2} - \frac{1}{2I}\frac{\partial^2}{\partial \phi^2}, \tag{4.2}$$

where $\mu_{S(CH_3)}$ is the reduced mass of the S-atom and the composite atom (CH_3),

$$\begin{aligned} \mu_{S(CH_3)} &= \frac{m_S m_{(CH_3)}}{m_S + m_{(CH_3)}}, \\ m_{(CH_3)} &= m_C + 3m_H. \end{aligned} \tag{4.3}$$

The moment of inertia about the molecular axis can be written as

$$\frac{1}{I} = \frac{1}{I_1} + \frac{1}{I_2}, \tag{4.4}$$

with

$$\begin{aligned} I_1 &= \mu_{S(CH_3)}(R\sin\alpha)^2, \\ I_2 &= 4m_C\left[r_{CC}\sin\left(\frac{\pi}{3}\right)\right]^2 + 4m_H\left[(r_{CC}+r_{CH})\sin\left(\frac{\pi}{3}\right)\right]^2. \end{aligned} \tag{4.5}$$

m_H, m_S, and m_C are the rest masses of the hydrogen, sulphur and carbon atom, respectively. r_{CC} and r_{CH} are the CC and CH bond distances of the phenyl moiety, respectively and α is the angle between S-CH_3 and SC bond at the ground-state (S_0) equilibrium geometry.

4.2.2 Wave-packet propagation

The photoinduced dynamics of thioanisole system is investigated by numerically solving the TDSE on a two dimensional grid in (R, ϕ) space. The time evolution of the system is calculated by ($\hbar$=1)

$$i\frac{\partial}{\partial t}\begin{pmatrix} |\psi_1(t)\rangle \\ |\psi_2(t)\rangle \\ |\psi_3(t)\rangle \end{pmatrix} = \boldsymbol{H}\begin{pmatrix} |\psi_1(t)\rangle \\ |\psi_2(t)\rangle \\ |\psi_3(t)\rangle \end{pmatrix}. \tag{4.6}$$

$|\psi_i(t)\rangle$ is the wave function at time t of the i^{th} state and the vibrational eigen functions of adiabatic ground state represents the initial wave function i.e. $|\psi_i(t=0)\rangle$. These vibrational eigen functions of the ground adiabatic state are excited to the $\pi\pi^*$ state in the FC region for the preparation of the initial WP. To determine the time evolution of wave function at time t, the exponential operator, i.e. $exp\big[-i\boldsymbol{H}\Delta t\big]$, at each time step is approximated by the SO method[99]:

Table 4.1: Numerical grid parameters

Parameters		
N_R/N_ϕ	265/128	Number of grid points
$R_{min}/R_{max}(a_0)$	2.5/15.07087	Extension of grid along R
ϕ_{min}/ϕ_{max}(rad.)	-π/π	Extension of grid along ϕ
$R_{flux}(a_0)$	9.3665	Location of the analysis plane
$R_{mask}(a_0)$	10.9933	Starting point of the damping function
T(a.u.)	40000.00	Total propagation time
ΔT(a.u.)	0.61036	Length of the time step used in the propagation

$$\exp\left[-i\boldsymbol{H}\Delta t\right] = \exp\left[\frac{-i\boldsymbol{V}\Delta t}{2}\right]\exp\left[-i\boldsymbol{T}\Delta t\right]\exp\left[\frac{-i\boldsymbol{V}\Delta t}{2}\right] + \mathcal{O}\big[(\Delta t)^3\big]. \tag{4.7}$$

The action of the KE operator on the wave function is carried out in the momentum space and then transformed back to the coordinate space by fast Fourier transform (FFT) method.

To avoid reflection of the WP components from the grid boundary a sine type of damping function is implemented in the asymptotic region of R.[73] The damping function is expressed as

$$f(R_i) = \sin\left[\frac{\pi}{2}\frac{(R_{mask} + \Delta R_{mask} - R_i)}{\Delta R_{mask}}\right], \qquad R_i \geq R_{mask}, \tag{4.8}$$

here $R = R_{mask}$ is the point where damping function is activated and its value is unity up to this point then it gradually decreases to zero at the grid edge. The dissociation yield is defined as the time-accumulated flux through dividing surface located at $R = R_{flux}$

$$\Phi^R(t) = \frac{1}{\mu}\int_{t=0}^{t} Im\left[\left\langle \Psi(R,\phi,\tau)\middle|\frac{\partial\Psi(R,\phi,\tau)}{\partial R}\right\rangle\right]\Bigg|_{R=R_{flux}} d\tau. \tag{4.9}$$

The time-dependent diabatic and adiabatic electronic population of the three coupled electronic states are calculated as expectation values of the respective projection operators.[104]

The diabatic/adiabatic population of i^{th} electronic state is defined as $\langle\Psi(t)|\psi_i^{d/a}\rangle\langle\psi_i^{d/a}|\Psi(t)\rangle$, i =0,1 or 2, where $\psi_i^{d/a}$ is the i^{th} WP component. The adiabatic WP components, ψ_i^a, are calculated by the following operation

$$\psi_i^a = \sum_{j=0}^{2} [U_{ji}]^\dagger \psi_j^d, \qquad j = 0, 1, 2 \tag{4.10}$$

where U_{ji} is ji^{th} element of diabatic-to-adiabatic transformation matrix i.e. U. The matrix U is constructed from the eigen functions of diabatic potential energy matrix and it is defined by the following equation

$$V^a = U^\dagger V^d U, \tag{4.11}$$

where V^a is the adiabatic potential energy matrix.[124, 125] The adiabatic potential energy surface of the three states for the present molecule is plotted in Fig. E.3 in APPENDIX E.

4.2.3 Mathematical framework of optimal control theory

In this present work, the optimization problem is mathematically formulated by the construction of a cost functional.[126, 127, 128] It is defined by

$$J[\epsilon(t)] = \Phi^R(T) - \alpha_0 \int_0^T |\epsilon(t)|^2 \, dt, \tag{4.12}$$

where $\Phi^R(T)$ is the total time integrated dissociation yield at time T (see Table. I) through the three adiabatic (S_0, S_1, and S_2) asymptotes which is described in Eq. 4.9. This quantity serves as an objective and maximization of it is the aim of the present study. In the second part of Eq. 10, α_0, designated as a penalty factor is chosen as $\alpha_0 = 0.001$ a.u. in this study. The negative sign in this part assures that maximization of J leads to the minimization of the second term i.e. to lower the fluence of the laser pulse with an electric field $\epsilon(t)$ to

avoid the undesirable physical processes (e.g., ionization) caused by high field strength. The primary goal of the present work is to maximize the cost functional $J[\epsilon(t)]$ using the GA. [38, 83, 129]

In order to quantify the time dependent laser field, a simple time-dependent sinusoidal function is taken into consideration which is multiplied with envelop function, $\epsilon(t) = \epsilon_0 \sin(\omega t) \cdot s(t)$, where ϵ_0 and ω are amplitude and the frequency of the pulse, respectively. The envelop function, $s(t)$, is a smooth function which describes the amplitude of the pulse at time t. In this work, this function is formulated as

$$s(t) = \begin{cases} \sin^2[\frac{\pi}{2}(\frac{t-t_0}{t_1-t_0})] & t_0 \leq t \leq t_1 \\ 1.0 & t_1 \leq t \leq t_2 \\ \sin^2[\frac{\pi}{2}(\frac{t_3-t}{t_3-t_2})] & t_2 \leq t \leq t_3 = T, \end{cases} \tag{4.13}$$

where, the initial time t_0 and t_3 are set to 0 and T, respectively. The other two time parameters, t_1 and t_2, controls the shape of the pulse. The GA is employed to search for the best possible combination of the four laser parameters E_0, ω, t_1 and t_2 to obtain the maximum value of the cost functional J (cf., Eq. 5.3).[80] GA works within a predefined parameter range, which is defined as $0.0 \leq \epsilon_0 \leq 0.5$, $0.0425 \leq \omega \leq 0.1865$, $0.0 \leq t_1 \leq 32000.0$, and $0.0 \leq t_2 \leq 40000.0$ a.u.

The GA follows the rules of Darwinian evolution such as survival of the fittest, crossover, mutation, etc. to find the best combination of parameters. The possible values of the parameters are randomly selected in binary number and a string of these binary numbers are introduced as "chromosome" in GA. In this case, each of the four laser parameters mentioned above are mapped onto a string of binary numbers of length 10 in a "chromosome". Therefore, for the four parameters the chromosome is composed of 40 binary digits or bits. Consequently, the number of possible sets of these four laser parameters is 2^{40}.

At the initial step or first generation of GA, a random selection of parameter set is performed among the possible parameter space. The number of selected parameter sets

or chromosomes in a generation is called total population and it is kept fixed at 10 for all the generations. By analogy with the biological evolution process, each chromosome corresponds to a trial laser field concomitantly a particular value of cost functional (Eq. 5.3) which is considered as the fitness value associated with that chromosome. Then a tournament selection of the chromosomes is performed where fitter chromosome from a randomly selected pair is allowed to mate to produce child. The operations like crossover, mutation, etc., are also applied on the initial population with a certain predefined probabilities ($P_{cross} = 0.5, P_{mutation} = 0.02$). This processes are repeated iteratively and the best set of parameters is determined for each of the generation. When the fitness value of the best parameter set fulfills the convergence criteria, then the parameter set is considered as the best solution within the defined parameter space.

4.3 RESULTS and DISCUSSION

The equilibrium molecular structure of thioanisole in the ground electronic state is analogous to phenol except oxygen and H-atom is replaced by sulphur and methyl group, respectively. Therefore, the potential energy surface of thioanisole is topologically similar to phenol but the $\pi\pi$ and $\pi\pi$* state are shallower than the latter.

4.3.1 Vibrational wave functions of ground state

The vibrational energy eigen values of the adiabatic ground state PES is calculated using pseudospectral method (see APPENDIX D). The sixteen lowest energy eigen values and their assignments in terms of two quantum numbers (n_R,n_ϕ) are given in Table II. The quantum number n_R and n_ϕ represents the number of nodes of the corresponding vibrational eigen function along coordinates R and ϕ, respectively.[130] The calculated fundamental frequencies of the stretching and coupling mode are 718 and 320 cm^{-1}, respectively. The experimental values of the fundamental frequency of the stretching mode is 735 cm^{-1}.[131]

Table 4.2: Eigenvalues, E_n(cm^{-1}), and assignments (n_R,n_ϕ) of the pseudospectral peaks of adiabatic ground state

E_n	(n_R, n_ϕ)	E_n	(n_R, n_ϕ)	E_n	(n_R, n_ϕ)	E_n	(n_R, n_ϕ)
448.34	(0,0)	1166.24	(1,0)	1874.87	(2,0)	2573.0	(3,0)
768.12	(0,1)	1483.12	(1,1)	2189.42	(2,1)	2887.52	(3,1)
1086.0	(0,2)	1802.12	(1,2)	2504.22	(2,2)	3200.82	(3,2)
1404.42	(0,3)	2116.62	(1,3)	2820.12	(2,3)	3512.12	(3,3)

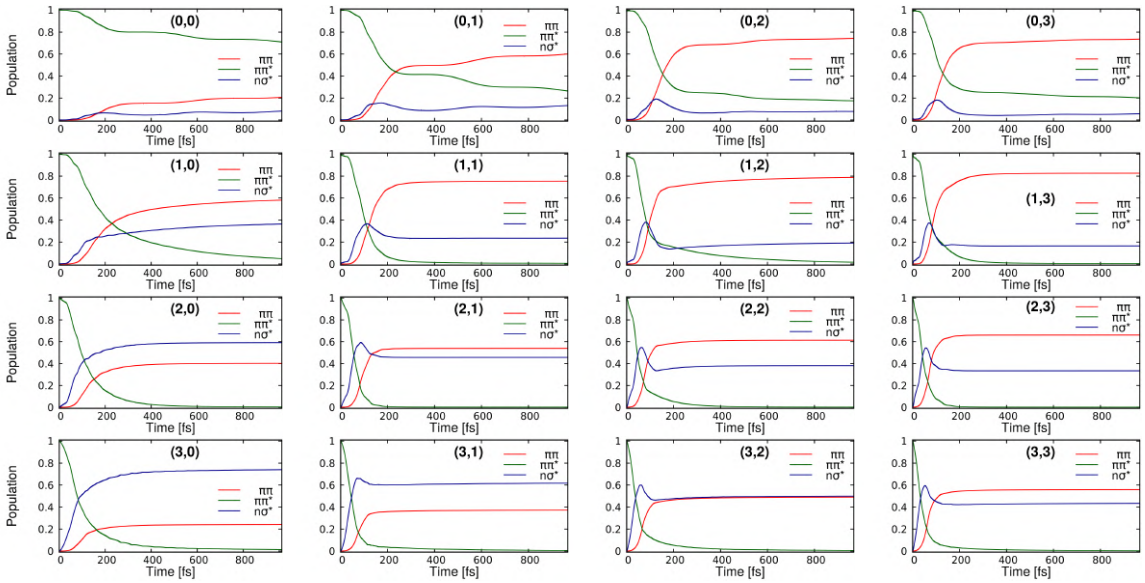

Figure 4.4: Diabatic electronic populations plotted with respect to time for sixteen initial conditions (the initial conditions are marked in the individual panels).

4.3.2 Electronic population dynamics

In order to investigate how the initial vibrational excitation influences the methyl photodissociation of thioanisole molecule, different initial wave functions are propagated on two dimensional coupled potential surfaces of lowest three electronic states. The initial wave functions are prepared by placing the sixteen vibrational eigen functions of the electronic ground state vertically into the $\pi\pi^*$ state.

Dynamics with $n_R = 0$ initial condition

The diabatic population dynamics of initial conditions where S-CH_3 stretching mode is in vibrational ground state like (0,0), (0,1), (0,2) and (0,3) shows an increment in population

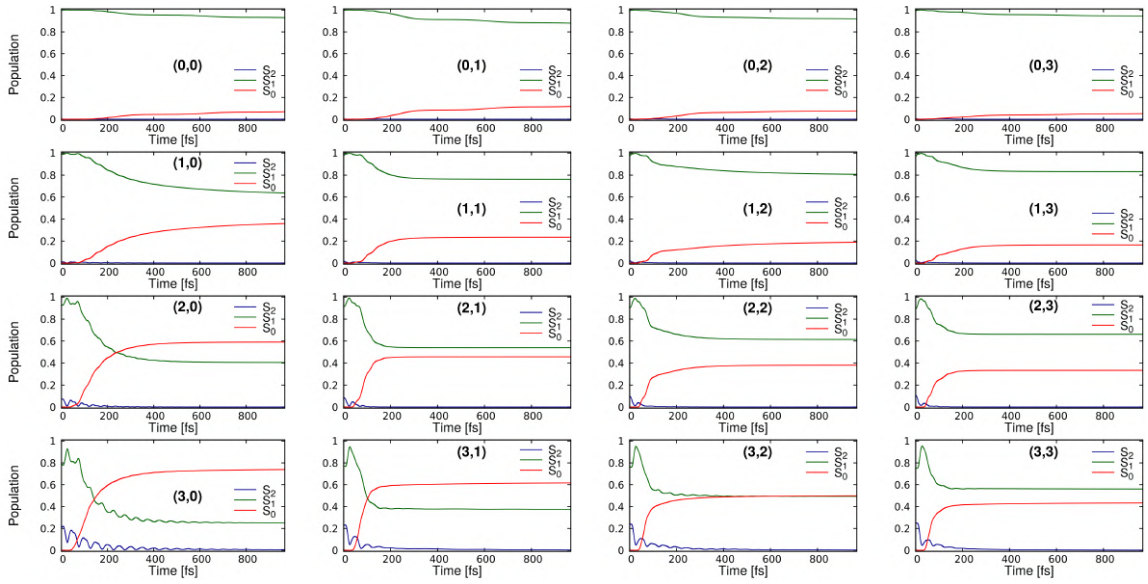

Figure 4.5: Adiabatic electronic population dynamics on the three electronic states for different initial vibrational states when they are vertically excited to $\pi\pi^*$ state in absence of laser pulse.

transfer between $\pi\pi^*$ and nσ^* states as the quantum number n_ϕ increases (cf., Fig. 4.4). This phenomenon can be understood by the inspection of S_1/S_2 CI. The lower cone of S_1/S_2 CI has a barrier of 0.23 eV with respect to the minimum of S_1 PES. Therefore, increase in quantum number n_ϕ that is, increase in vibrational energy along ϕ mode helps the WPs to overcome the barrier. The energies associated with this vibrational WPs are less than the S_1/S_2 CI barrier. This implies that the tunneling plays a very important role in the $\pi\pi^*$ to nσ^* transition for (0,0), (0,1), (0,2) and (0,3) initial conditions. This is further supported by the adiabatic population dynamics (see Fig. 4.5), which shows that the electronic population remains predominantly in the S_1 state throughout the dynamics for (0,0), (0,1), (0,2) and (0,3) initial conditions, with minimal transfer to S_0 ($< 10\%$) and over 90% of the population retained in S_1. The s_0 state gains the small amount of population by the nonadiabatic transition at S_0/S_1 CI and moves towards the dissociation into the methyl and phenyl fragments in their ground states (cf. Fig. E.1). Similarly, the population in the $\pi\pi^*$ state undergoes dissociation into the two fragments in their excited states (cf. Fig. E.1), with the dissociation yield increasing as the n_ϕ quantum number rises.

Dynamics with $n_R \geq 1$ initial condition

The initial conditions where S-CH_3 stretching mode is vibrationally excited by one quantum of energy that is, (1,0), (1,1), (1,2) and (1,3) vibrational wave functions of ground state contains energy comparable to the S_1/S_2 CI barrier. Therefore, a very fast population transfer from $\pi\pi^*$ to nσ^* state is observed (cf., Fig. 4.4). It should be noted that the diabatic population of nσ^* state shows a very sharp rise in the initial duration of the dynamics, within $\sim$50 fs. The reason behind is that in the early stages of the dynamics a part of the population pass through the S_1/S_2 CI and due to a very repulsive nature of nσ^* state the WP moves quickly to hit the next CI (S_0/S_1). The WP splits into two parts here and move towards $\pi\pi$ and nσ^* channels. Figure 4.4 reveals that there is a noticeable impact of the initial excitation of the coupling mode on the lifetime of the $\pi\pi^*$ state. The interesting odd-even effect can be observed with respect to the occupation number of the coupling mode. For initial conditions with an odd number of quanta into the coupling mode [(1,1) and (1,3)], the decay rate of $\pi\pi^*$ state is higher than with an even number of quanta of the coupling mode [(1,0) and (1,2)]. From Figure E.1, it is apparent that in the long propagation time range there is no odd-even effects in the time accumulated dissociation yields for different initial conditions but a close inspection reveals that the odd-even effect is present in the short time range.

The initial conditions with two quanta of S-CH_3 stretching vibrational energy, that is, (2,0), (2,1), (2,2) and (2,3) WPs, show the similar fast decay of the $\pi\pi^*$ state population (see Fig. 4.4). The odd-even effect is still present in these cases because the vibrational energies embedded in these WPs are not much higher than the barrier created by the S_1/S_2 CI. Consequently, the corresponding time accumulated dissociation yields also show the odd-even effect like in the previous case. The odd-even effect is not so prominent in the electronic population dynamics for (3,0), (3,1), (3,2) and (3,3) as the previous initial conditions (cf. Fig. 4.4) because the vibrational energies are higher than the barrier created by the S_1/S_2 CI.

The time-dependent adiabatic population dynamics for the initial conditions (1,0), (1,1), (1,2), and (1,3) reveal that as the quantum number n_ϕ increases, the population transfer from the S_1 state to the S_0 state decreases (see Fig. 4.5). Adding one quantum of energy to the R mode provides the $\pi\pi^*$ WP component sufficient energy to overcome the S_1/S_2 CI barrier. As a result, a significant portion of the population undergoes nonadiabatic transitions at both the S_1/S_2 and S_0/S_1 CIs, leading to a substantial accumulation of population in the S_0 state at its asymptote.

The adiabatic population dynamics for the (2,0), (2,1), (2,2), and (2,3) initial conditions follows the similar trend but the population transfer from S_1 to S_0 state is much more higher than than the previous case because of the presence of two quantum of vibrational energy along R mode. For the same reason the population transfer from S_1 to S_0 state is increased for (3,0), (3,1), (3,2), and (3,3) initial conditions (see Fig. 4.5).

It appears that the survival probability of the $\pi\pi^*$ state is extremely sensitive to the initial vibrational excitation of the S-CH_3 stretching mode. The initial excitation of the torsional mode leads to a recognizable phenomenon the 'odd-even' effect on the decay rates and branching ratios. A similar effect was also reported by Baer *et. al.*[132] and Lan *et. al.*[73]. The initial conditions $n_R = 2$ and $n_R = 3$ does not enhance the nonadiabatic decay rate significantly. In 1987, Sobolewski predicted a similar scenario in which the nonadiabatic decay (i.e., radiationless decay) rate becomes saturated with increasing initial vibrational excitation within statistical limits employing a two states model with weak coupling.[133]

4.3.3 Dynamics with optimal pulse

OCT with $n_R = 0$ initial conditions

The vibrational wave functions of $n_R = 0$ ((0,0), (0,1), (0,2), and (0,3)) are excited to the $\pi\pi^*$ state using continuous laser pulse within the GA based optimal control formalism as described in section II.C. The corresponding time-dependent optimal pulses are depicted

in panels (A1,A2,A3,A4) of Fig. 4.6. The frequency spectra of these optimal pulses are also calculated by Fourier transformation from the time domain to the frequency domain. The central frequencies for the (0,0), (0,1), (0,2), and (0,3) initial conditions are 40615 cm^{-1}, 40578 cm^{-1}, 39991 cm^{-1}, and 40133 cm^{-1}, respectively, which are extracted from the corresponding frequency spectra (cf., panels (B1,B2,B3,B4) in Fig. 4.6).

In order to understand the optimal pulse driven methyl photodissociation mechanism on three coupled potential energy surfaces, the time-dependent diabatic and adiabatic populations are plotted in panels (C1,C2,C3,C4) and (D1,D2,D3,D4) in Fig. 4.6, respectively. The initial WP prepared in the ground electronic state which is gradually excited to the $\pi\pi^*$ state in the FC region by the optimal pulse. Consequently, the $\pi\pi^*$ state acquires population in the initial time (~ 200 fs) of dynamics. However, the $\pi\pi^*$ population starts decreasing after touching a maximum, because of the nonadiabatic population transfer to the nσ^* state. The vibrationally excited component of the WP predominantly populates the nσ^* state in the FC region. The population of nσ^* state increases and it converges to 65.6%, 60.8%, 45%, and 39.5% for (0,0), (0,1), (0,2), and (0,3) initial conditions, respectively. In contrary, the population of ground state decreases and converges to 32.8%, 37.4%, 51.4%, and 57.4%, respectively. The "odd-even" effect has not been observed. The population acquired by nσ^* state decreases monotonically with the initial excitation along ϕ. The increase in n_ϕ, i.e. initial excitation along the coupling mode ϕ, leads to an increases in the vibrational energy along ϕ mode. Therefore, when the WP hits the S_0/S_1 CI, the higher energy asymptote becomes more accessible for WPs with higher n_ϕ. As a consequence, the ground state gains more population at the expense of nσ^* state population for higher n_ϕ. For all these initial conditions, the adiabatic population of S_1 state increases initially (up to ~ 200 fs) and then converges to the population of daibatic ground state population. Similarly, the ground state population decreases initially like the diabatic ground state and converges to population of diabatic nσ^* state. The S_2 state initially acquires some population because of intensity borrowing effect [134] in the FC region. Thereafter, the population decreases because of

nonadiabatic population transfer to the S_1 state.

When the initial wave function is prepared in the FC region of $\pi\pi$ state by the vertical excitation of (0,0), (0,1), (0,2), and (0,3) vibrational eigen functions of ground state, the time integrated dissociation flux is substantially low in the nσ* channel. The flux is not very high for ground state channel with (0,0) initial condition but it increases significantly with the increase of n_ϕ quantum number (see Fig. E.1). Whereas, in presence of the optimal pulse the fluxes through the nσ* channel is enhanced substantially and there is a dependence of the branching ratio of dissociation yields through the nσ* and ground state asymptotes on the quantum number n_ϕ (cf. Fig. 4.6). The energy content within the initial WPs increases with n_ϕ. Consequently, the accessibility of the diabatic ground state asymptote through energetically higher dissociative channel increases with the expense of yield through energetically lowest, nσ*, channel when the initial vibrational quantum number n_ϕ, increases.

In all the initial conditions with $n_R = 0$ the maximum flux (F) and the cost functional (J) increases progressively and converges to their maximum value (see panels (F1,F2,F3,F4) in Fig. 4.6).

The OCT with $n_R = 1$ initial condition

Fig. 4.7 represents the results of the optimal control calculations with the initial conditions (1,0), (1,1), (1,2), and (1,3). The panels (A1,A2,A3,A4) shows the temporal profile of the optimal pulse shape calculated by the GA based optimal control scheme for those initial conditions, respectively. The corresponding central frequencies of these laser pulses are 38752 cm^{-1}, 37495 cm^{-1}, 38168 cm^{-1}, and 38585 cm^{-1}, respectively (see panels (B1,B2,B3,B4)). The diabatic electronic population dynamics for these initial conditions are also similar to the previous case (i.e. $n_R = 0$ initial conditions), where the laser pulse predominantly populates the nσ* state in the FC region. The nσ* population increases gradually for all these initial conditions and converges to 68.8%, 53.0%, 56.7%, and 44.0%

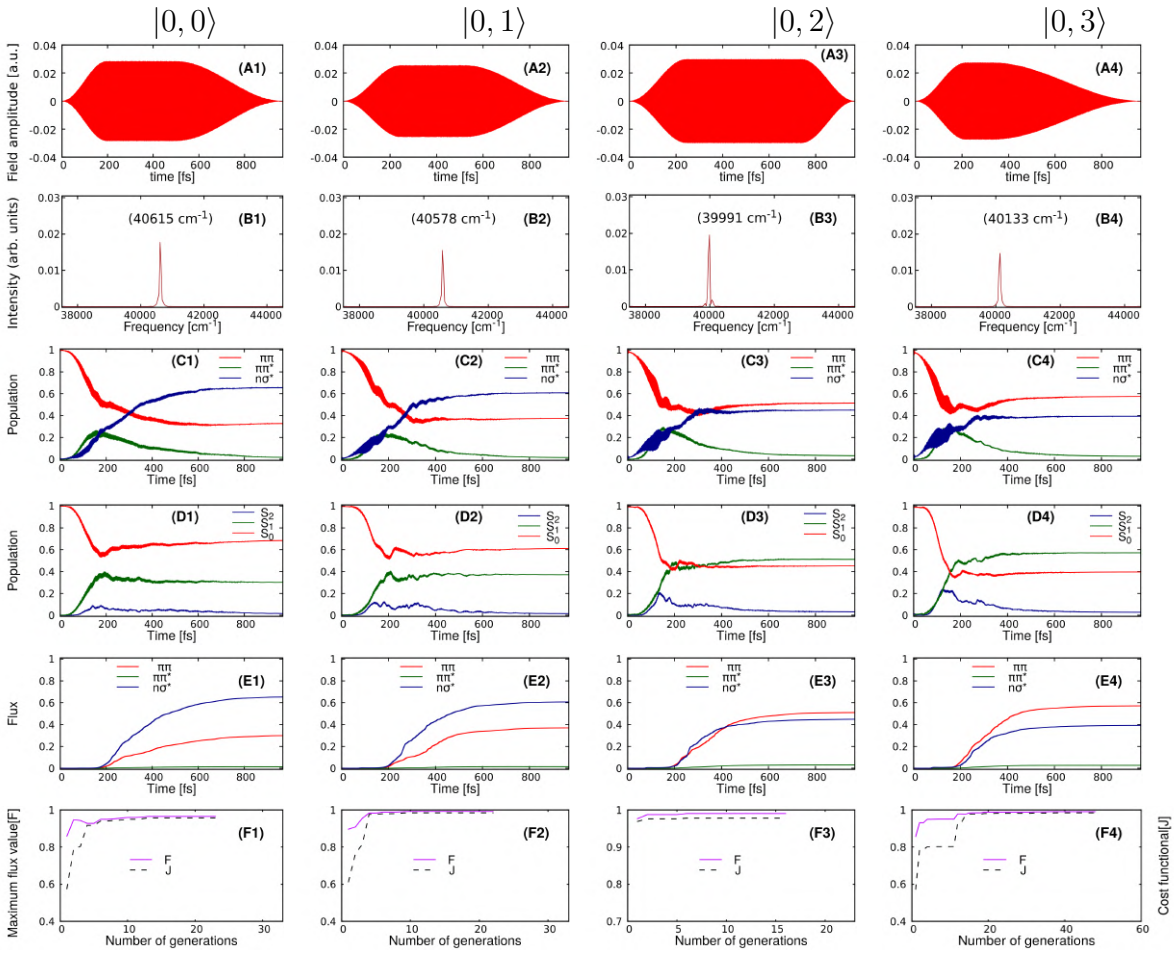

Figure 4.6: Results of OCT calculations using (0,0), (0,1), (0,2) and (0,3) initial conditions. The temporal profile of optimal pulse (panels (A1,A2,A3,A4)), the frequency spectrum of these pulses (panels (B1,B2,B3,B4)), diabatic population dynamics (panels (C1,C2,C3,C4)), adiabatic population dynamics (panels (D1,D2,D3,D4)), time-integrated flux with respect to time (panels (E1,E2,E3,E4)), and values of cost functional [J], in addition, the total dissociative flux [F] at each generation (panels (F1,F2,F3,F4)) are plotted.

of the total population. The $\pi\pi^*$ state gets populated in the initial $\sim$160 fs, $\sim$220 fs, $\sim$200 fs, and $\sim$290 fs for (1,0), (1,1), (1,2), and (1,3) initial conditions, respectively, then the population decreases monotonously up to almost zero (see panels (C1,C2,C3,C4)). The adiabatic population dynamics with respect to time has been plotted in the panels (D1,D2,D3,D4). The population of S_1 state increases up to $\sim$200 fs and then converges to diabatic population of the ground state after almost 600 fs. Similarly, up to initial 200 fs, because of $\pi\pi^*$ excitation in the FC region, the ground state population increases but then converges to the

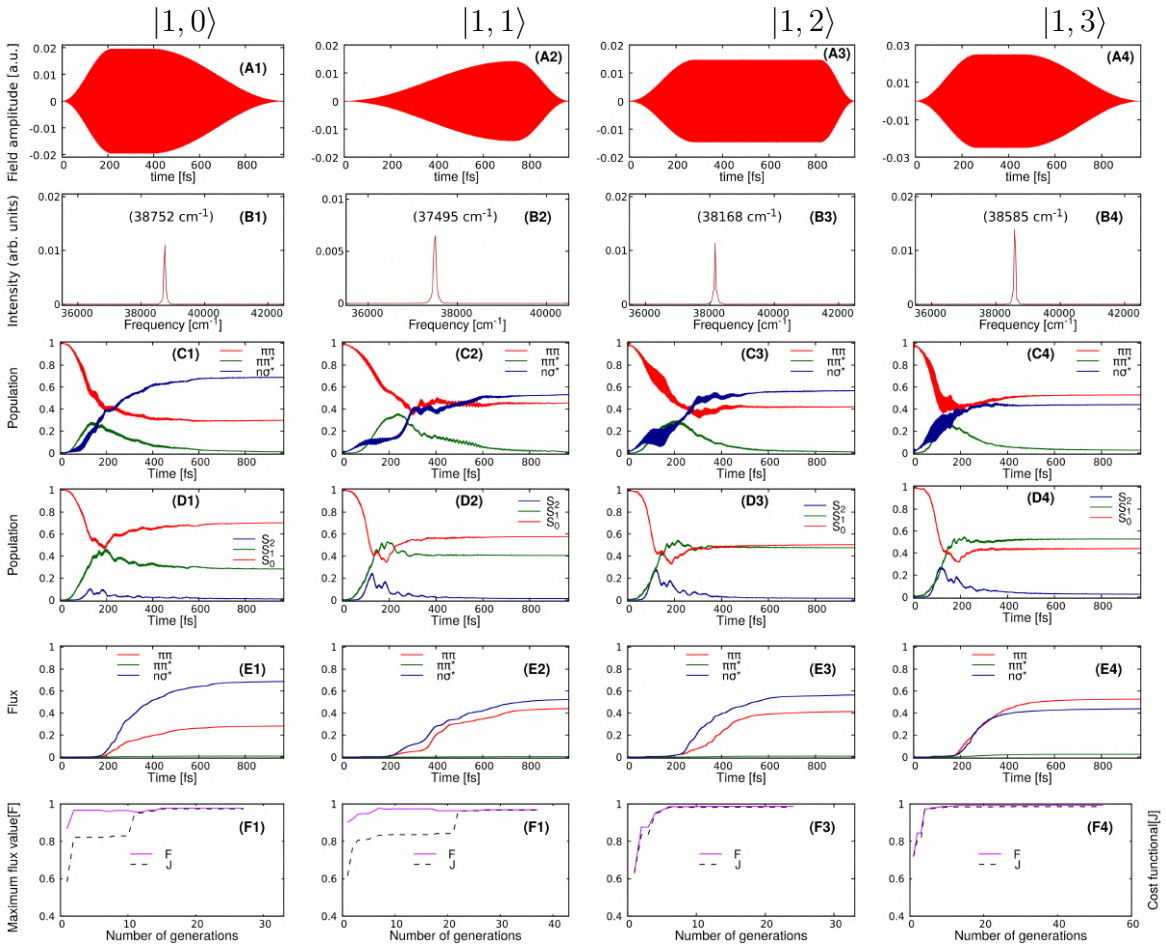

Figure 4.7: Results of OCT calculations using (1,0), (1,1), (1,2) and (1,3) initial conditions. The temporal profile of optimal pulse (panels (A1,A2,A3,A4)), the frequency spectrum of these pulses (panels (B1,B2,B3,B4)), diabatic population dynamics (panels (C1,C2,C3,C4)), adiabatic population dynamics (panels (D1,D2,D3,D4)), time-integrated flux with respect to time (panels (E1,E2,E3,E4)), and values of cost functional [J], in addition, the total dissociative flux [F] at each generation (panels (F1,F2,F3,F4)) are shown.

diabatic nσ* state population after 600 fs. Although, the adiabatic population plots suggest that the S_2 state gains populaton to some extent (below 20%) up to ∼400 fs because of intensity borrowing effects[134], it starts loosing population due to nonadiabatic transition through S_1/S_2 CI. Then it converges to almost zero at the end of the dynamics. In presence of the optimal pulses the system starts dissociating at ∼200 fs mainly through the nσ* and ground state asymptotes. In this case, the "odd-even" effect is not observed, i.e. initial conditions with odd quantum number of n_ϕ does not enhances the dissociation towards the nσ* channel.[132]

For all the initial conditions with $n_R = 1$ the maximum flux (F) and the cost functional (J) increases progressively and converges to their maximum value (see panels (F1,F2,F3,F4) of Fig. 4.7).

The OCT with $n_R = 2$ initial condition

In an analogous way, optimal control calculations have also been performed for the initial conditions (2,0), (2,1), (2,2), and (2,3). The corresponding results are presented in Fig. E.2. The shape of the optimal pulses calculated from the GA using these initial conditions are plotted in the panels (A1,A2,A3,A4). The corresponding central frequencies of these pulses are extracted from the frequency spectra and they are 37648 cm^{-1}, 37805 cm^{-1}, 37618 cm^{-1}, and 37202 cm^{-1}, respectively (cf., panels (B1,B2,B3,B4)). In this case also, the laser primarily populates the nσ* state and the population rises until it converges to a certain value. For (2,0) initial condition the nσ* population converges to 75$\%$ of the population, with an increase in quantum number n_ϕ this converged population value decreases i.e., for (2,1), (2,2), and (2,3) initial conditions the nσ* population converges to 67.8$\%$, 52.2$\%$, and 34.6$\%$ of the total population, respectively. The $\pi\pi$* state gets populated in the early duration of the dynamics until $\sim$200 fs, $\sim$160 fs, $\sim$200 fs, and $\sim$90 fs for (2,0), (2,1), (2,2), and (2,3) initial conditions, respectively, due to the action of optimal pulses. Subsequently, the population decreases unless it converges to almost zero (cf., panels (C1,C2,C3,C4)). When the laser pulse excites the WP from S_0 to S_1 state in the FC region, the S_2 state acquires very small amount of population probability (below 10$\%$) via the so-called intensity borrowing effects.[134] The S_1 population increases in the initial period of the dynamics then it decreases after arriving at a maximum for (2,0) and (2,1) initial condition. However, the S_1 population almost gets converged to the maximum for (2,2) and (2,3) initial conditions. The associated energy with the WP (2,2) and (2,3) are so high that it can promptly reach the two adiabatic S_0 and S_1 asymptotes. Consequently, the S_1 population increases rapidly and converges for these two initial conditions. The time

integrated dissociation fluxes towards the three asymptotes are plotted with respect to time in panels (E1,E2,E3,E4). It has been observed that with the increase in n_ϕ the total integrated flux towards nσ* asymptote decreases and it increases towards $\pi\pi$* state asymptote.

For all the initial conditions with $n_R = 2$ the maximum flux (F) and the cost functional (J) increases progressively and converges to their maximum value (see panels (F1,F2,F3,F4) in Fig. E.2).

4.3.4 Time-dependent wave packets

In this section, a comparison between the nuclear WPs is carried out at different times in the nσ*, $\pi\pi$*, and diabatic ground states which evolve by the continuous excitation in presence of optimal field and after vertical excitation (i.e. in absence of field) to $\pi\pi$* state (cf., Figs. 4.8, 4.9, and 4.10). The dotted lines in all the plots represent the linear geometries and the small pink circles on this line represent the positions of the CI. In other words the molecular geometry of the two CIs are planer. For all the initial conditions, most of the WP densities remains near to the dotted line, that is, propagate along R coordinate keeping geometries almost near to planer.

The (0,0) initial condition

The (0,0) wave function of ground state is vertically excited to the $\pi\pi$* state in the FC region. The panel (A1) of Fig. 4.9 represents the probability density of the diabatic $\pi\pi$* component of WP at time 182.48 fs. It is observed that the shape of the WP has been little stretched along ϕ which implies energy is redistributed along ϕ mode. At 364.96 fs, an interference pattern along ϕ appears in the probability density plot of $\pi\pi$* component. Also the amplitude of probability density on the $\phi = 0$ line is almost double of the previous snapshot (cf., panel (A2) of Fig. 4.9). Since the diabatic coupling is non-zero at the FC region, a portion of the $\pi\pi$* WP component gets transferred to the nσ* state and also gets transferred back in time to the $\pi\pi$* state, leading to the interference pattern and enhancement

in the probability amplitude. A nodal pattern is observed along the line at $\phi = 0$ in the $\pi\pi^*$ WP density which is generated by the CI between nσ^* and ground state (see panels (A1) and (A2) in Fig. 4.8). Similarly, the nσ^* component of the WP also appears with a nodal line at $\phi = 0$ and it is generated by the CI between $\pi\pi^*$ and nσ^* states (see panels (A1) and (A2) in Fig. 4.10). These nodal lines are the result of GP effect. [71, 73, 88] The ground and nσ^* state components of the WP are extended up to their corresponding asymptotes which reveals that both the ground state and nσ^* state are the active photodissociation channels.

In the quantum dynamics calculations with optimal laser pulse the initial WP is prepared with the (0,0) vibrational eigen function of the ground state potential energy surface. The panels (B1) and (B2) of Fig. 4.8 represents the probability densities of ground state component of WP, which is evolved in presence of optimal pulse generated by the GA based optimal control scheme, at 182.48 fs and 364.96 fs, respectively. The optimal pulse gradually excites the WP to the $\pi\pi^*$ state in the FC region. Consequently, the $\pi\pi^*$ component of the WP is mainly localized in FC region and its pattern exactly mimics the ground state component in the FC region (see (B1) and (B2) of Fig. 4.9). The probability density of the WP in the $\pi\pi^*$ state is delocalized along ϕ mode that is because the potential energy surface of $\pi\pi^*$ state is very much shallow along the ϕ mode in comparison to the ground state. Therefore, after reaching to the $\pi\pi^*$ state the WP easily gets delocalized along ϕ coordinate. The nσ^* potential energy surface crosses the $\pi\pi^*$ and ground state along ϕ coordinate at $\sim$0.5 rad. and $\sim$1.0 rad., respectively. As a consequence, a portion of WP component of $\pi\pi^*$ state moves to the ground state in time and produces the interference pattern in the delocalized part of the WP density of the FC region in the ground state. Similarly, a few vibrationally excited component of the $\pi\pi^*$ state WP move to the nσ^* state and comes back to the $\pi\pi^*$ state which creates the interference pattern in the $\pi\pi^*$ state. The nodal pattern of the $\pi\pi^*$ WP density along ϕ coordinate bears the evidence of the vibrational excitation along R mode. So, the optimal laser pulse excites the WP to suitable vibrational state of $\pi\pi^*$ state to access the nσ^* state. Then, due to repulsive nature of the nσ^* state, the WP

reaches the S_0/S_1 CI rapidly. At S_0/S_1 CI, the WP splits into two parts due to nonadiabatic transition. One of them follows the diabatic nσ* asymptote which leads to the dissociated fragments (PhS and CH_3) in their ground electronic states and another part climbs to the diabatic ground state asymptote which leads to the fragments (PhS[D_1] and CH_3[D_0]) in the excited state. The energy difference between the nσ* and ground state asymptotes is very low (cf., Fig. 4.3(a)), therefore a portion from each of the density component moves back and forth between the two PESs and produces an interference pattern in their asymptotic regions (cf., panel (B2) of Fig. 4.8 and 4.10). From the WP probability density plots of nσ* state (cf., panels (B1) and (B2) in Fig. 4.10), it can be seen that the WP bifurcates along coordinate R from S_1/S_2 CI. The same phenomenon is also observed in ground state WP density. This is the consequence of the GP effect.

An interesting fact is that when the (0,0) vibrational wave function is vertically excited to the $\pi\pi$* state, the WP propagates along the reaction coordinate, R, following adiabatic path on $\pi\pi$* and nσ* state (cf., Fig. 4.8 and 4.10). In other words, the WP spreads out along R at a large torsional angle, ϕ on these states. The barrier created by the S_1/S_2 CI along R at ϕ = 0 (planner geometry) is higher than the vibrational energy associated with the (0,0) WP. Therefore, the WP prefers to move along the reaction coordinate at large ϕ where this barrier is less and appears as a hump instead of CI. Consequently, the dissociation yield on diabatic ground state asymptote is higher than the energetically lower, nσ*, asymptote (see Fig. E.1). On the other hand, when the (0,0) WP is excited to the $\pi\pi$* state then the WP propagates along R following the noadiabatic path on $\pi\pi$* and nσ* state (cf., Fig. 4.8 and 4.10). In other words, the WP spreads out along R remaining close to ϕ = 0, i.e. planner geometry. Since, the two CIs are present along R at ϕ = 0, the WP participates in the nonadiabatic transitions and finally the dissociation yield in the nσ* asymptote increases (see panel (E1) of Fig. 4.6).

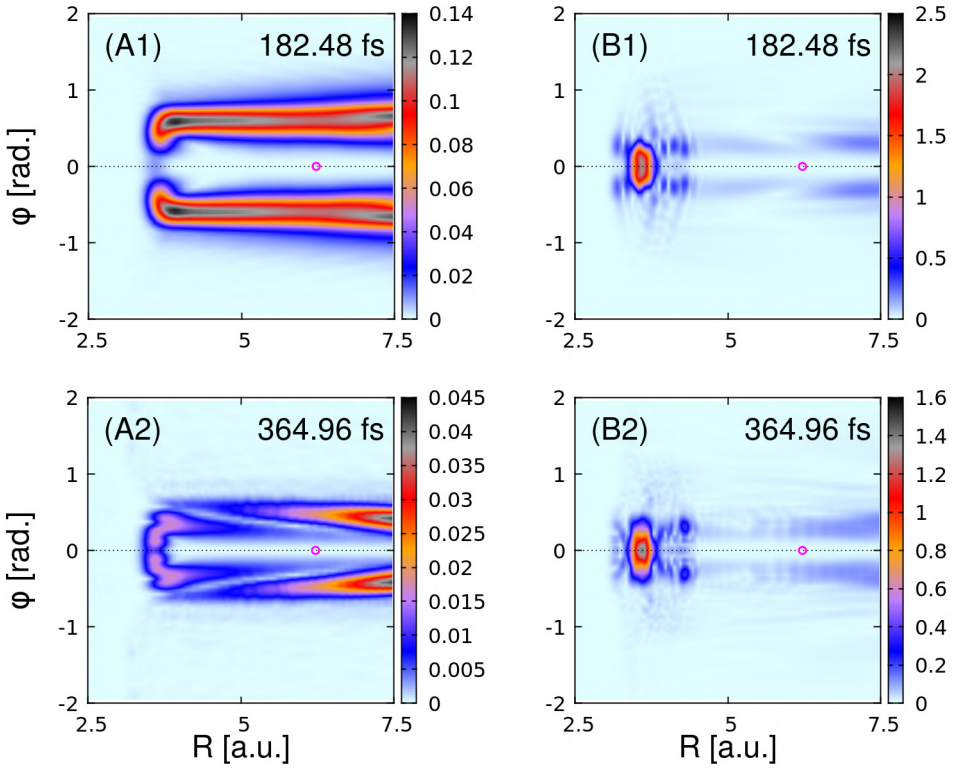

Figure 4.8: Snapshots of the WP probability density in the diabatic ground state for the (0,0) initial condition. The panels (A1) and (A2) are the snapshots at 182.48 fs and 364.96 fs for vertical excitation, respectively. The (B1) and (B2) are the snapshots at 182.48 fs and 364.96 fs for excitation by optimal pulse, respectively. The pink circle represents the position of the CI.

The (1,1) initial condition

Figures 4.11, 4.12, 4.13 show the WP probability densities on the ground, $\pi\pi^*$, and nσ^* diabatic potential energy surfaces, respectively, at different time for the aforementioned two types of excitation where initial vibational WP is (1,1) eigen function of the ground electronic state. In the case of vertical excitation to the $\pi\pi^*$ state the probability density of $\pi\pi^*$ WP component remains localized in the FC region (see panels (A1) and (A2) of Fig. 4.12). The $\pi\pi^*$ WP component preserves the initial nodal patterns of (1,1) eigen function up to $\sim$195 fs. Then, the nodal pattern along R eventually disappears, as it can be seen in the snapshot at 304.14 fs, and the WP component moves to the nσ^* state through nonadiabatic transition at the S_1/S_2 CI. The $\pi\pi^*$ WP density is delocalized along the ϕ mode because it

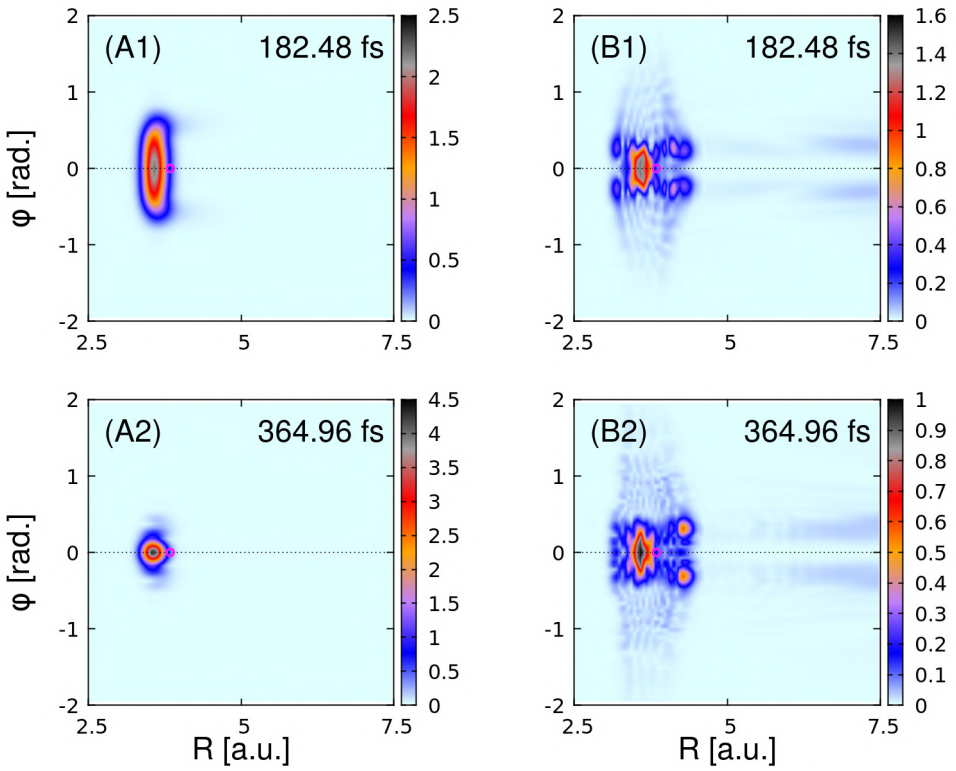

Figure 4.9: Snapshots of the WP probability density in the diabatic $\pi\pi^*$ state for the (0,0) initial condition. The panels (A1) and (A2) are the snapshots at 182.48 fs and 364.96 fs for vertical excitation, respectively. The (B1) and (B2) are the snapshots at 182.48 fs and 364.96 fs for excitation by optimal pulse, respectively. The pink circle represents the position of the CI.

contains extra one quantum of vibrational energy along ϕ mode. Since, the WP is initially excited by one quantum along each of the modes, the WP can access the nσ^* state in the FC region and also gets enough energy to overcome the barrier of S_1/S_2 CI. This is how, the nσ^* state borrows the WP density from $\pi\pi^*$ state and leads to the photodissociation followed by another nonadiabatic transition through the CI between the ground and nσ^* state. While the initial WP prepared in the $\pi\pi^*$ state was an antisymmetric function of ϕ, we have a symmetric wave function in the nσ^* state. The ground state also acquires WP density due to the nonadiabatic transition through CI between ground and nσ^* state and instantly reaches the dissociation limit. Therefore, the peak of the probability density is observed near or in the asymptotic region of diabatic ground state (see panels (A1) and (A2) in Fig. 4.11). It is revealed that the nodal line along S-C stretching coordinate is present in

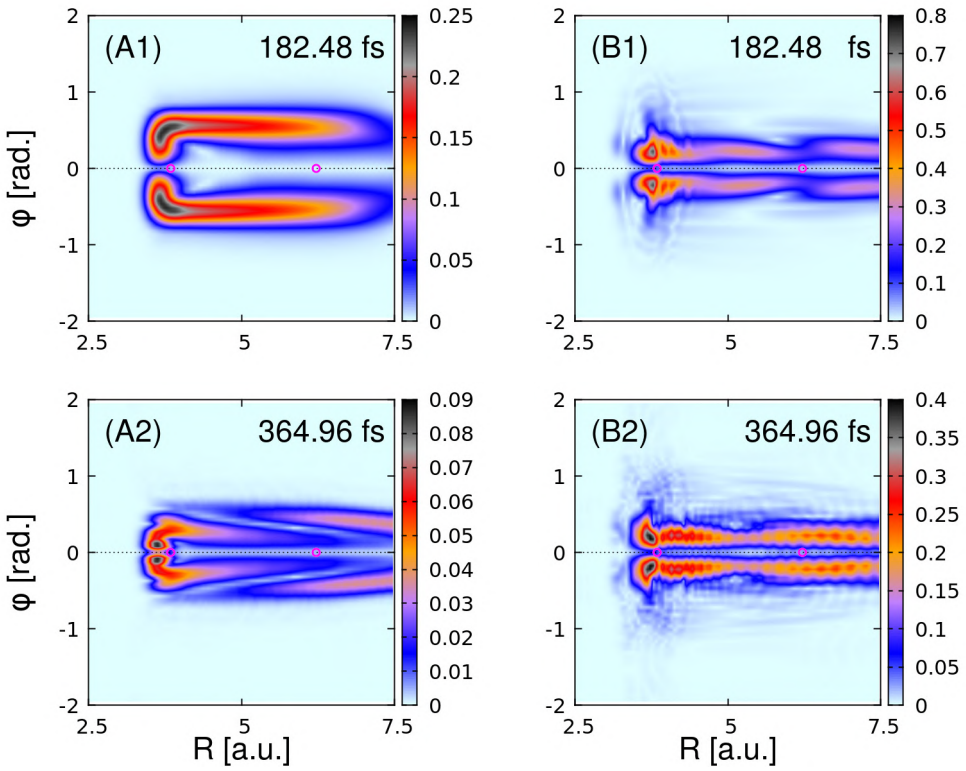

Figure 4.10: Snapshots of the WP probability density in the diabatic nσ* state for the (0,0) initial condition. The panels (A1) and (A2) are the snapshots at 182.48 fs and 364.96 fs for vertical excitation, respectively. The (B1) and (B2) are the snapshots at 182.48 fs and 364.96 fs for excitation by optimal pulse, respectively. The two pink circles represent the positions of the two CIs.

the ground state wave function.

In the other case, the (1,1) vibrational eigen function of the ground state is excited to $\pi\pi$* state in the FC region by the optimal pulse which is calculated by the GA based optimal control scheme. The two snapshots of probability densities of the ground state wave function component at time 194.65 fs and 304.14 fs are shown in the panels (B1) and (B2) panels of Fig. 4.11, respectively. The ground state wave function remains localized mainly in the FC region in the initial duration of dynamics (cf., (B1) panel in Fig. 4.11) without loosing its two nodes. Then slowly the density in the FC region on the ground state decreases because of the continuous excitation to the excited states by the optimal laser pulse. The two nodes are also preserved in the probability density at 304.14 fs in the FC region (cf., (B2) panel in Fig. 4.11). The optimal laser pulse excites the WP to the $\pi\pi$* state gradually

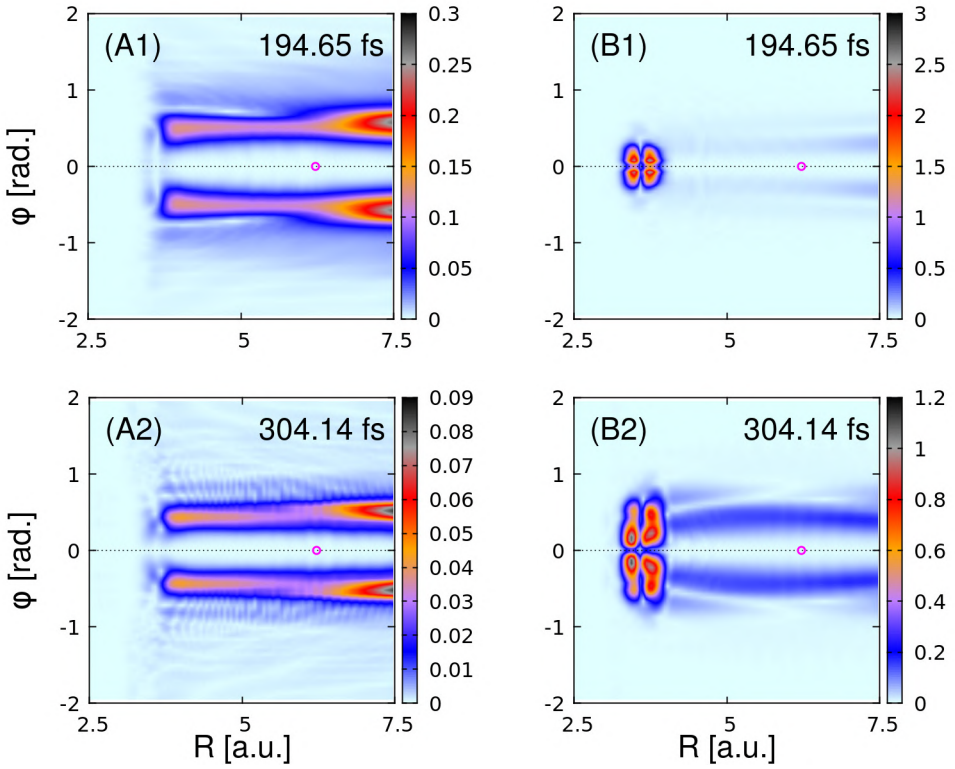

Figure 4.11: Snapshots of the wave packet probability density in the diabatic ground state for the (1,1) initial condition. The panels (A1) and (A2) are the snapshots at 194.65 fs and 304.14 fs for vertical excitation, respectively. The (B1) and (B2) are the snapshots at 194.65 fs and 304.14 fs for excitation by optimal pulse, respectively. The pink circle represents the position of the CI.

from the ground state in FC region. Therefore, the probability density on the $\pi\pi^*$ surface is localized in the region of well and almost exactly mimics the ground state component in the FC region. The nσ^* component of the WP also persists the nodal line along the ϕ mode in the FC region (cf., (B1) and (B2) panels in Fig. 4.13). Since, the nonadibatic coupling between $\pi\pi^*$ and nσ^* state in nonzero in the FC region, nσ^* state acquires probability density because of nonadibatic transition in this region. The nonadiabatic coupling is an odd function of ϕ, therefore, we have a symmetric wave function with respect to ϕ mode, which was antisymmetric in the ground state and in the nσ^* state. In other words, the nodal line along the S-C stretching direction disappears after nonadiabatic transition through the S_1/S_2 CI. An interference pattern is observed in the asymptotic region of the nσ^* state which is the result of very small energy gap between diabatic ground and nσ^* state in their asymptotic

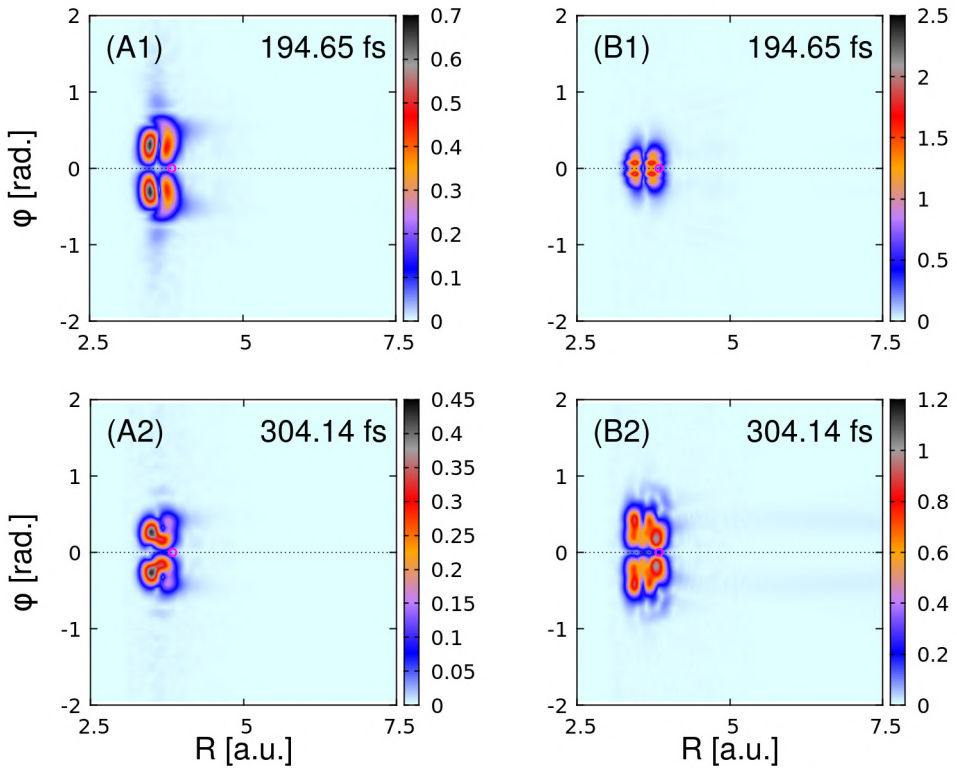

Figure 4.12: Snapshots of the WP probability density in the diabatic $\pi\pi^*$ state for the (1,1) initial condition. The panels (A1) and (A2) are the snapshots at 194.65 fs and 304.14 fs for vertical excitation, respectively. The (B1) and (B2) are the snapshots at 194.65 fs and 304.14 fs for excitation by optimal pulse, respectively. The pink circle represents the position of the CI.

region.

When the (1,1) wave function is excited to the $\pi\pi^*$ state, both the adiabatic and diabatic paths become active (cf. Fig. 4.11 and 4.13). The (1,1) vibrational WP contains enough energy to overcome the barrier created by the S_1/S_2 CI. Therefore, the nσ^* state can acquire population from the $\pi\pi^*$ state by nonadiabatic transition. At the CI between ground and nσ^* state the WP transits nonadiabatically to the lower energy asymptote because of having extra vibrational energy by one quantum along ϕ mode. The ground state component of the WP follows the adiabatic path and leads to dissociation into the excited state of the photofragments. Although the nonadiabatic transition is enhanced compared to the (0,0) initial condition, the dissociation yield of nσ^* state is less than the ground state. On the other hand, the excitation of WP by the optimal laser pulse promotes the nonadiabatic transition

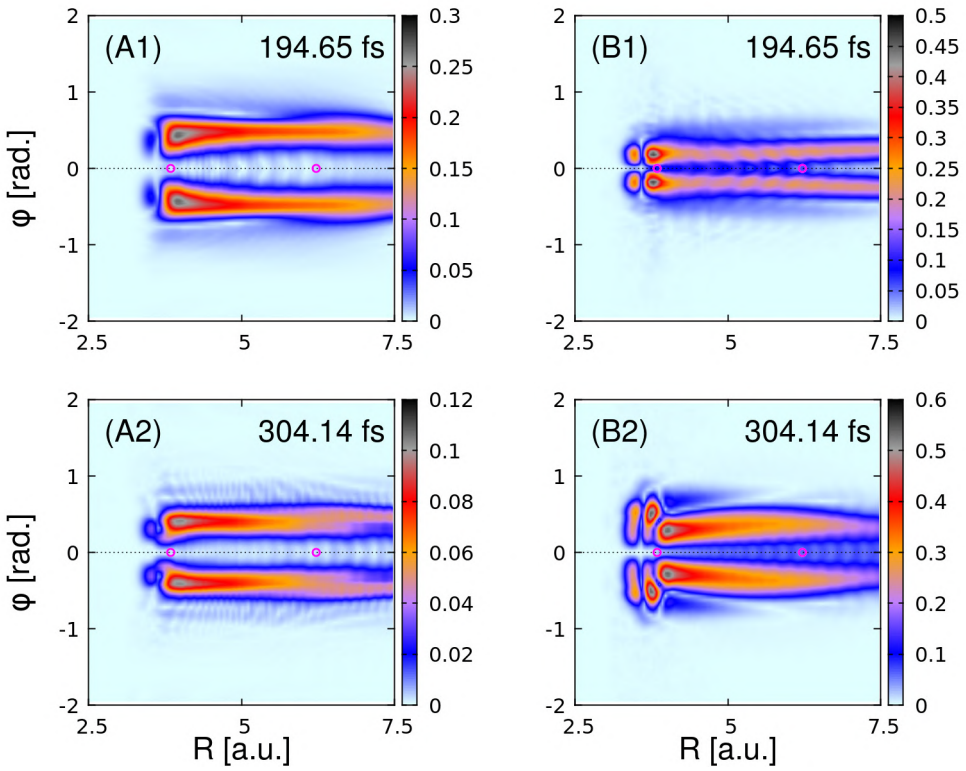

Figure 4.13: Snapshots of the WP probability density in the diabatic nσ* state for the (1,1) initial condition. The panels (A1) and (A2) are the snapshots at 194.65 fs and 304.14 fs for vertical excitation, respectively. The (B1) and (B2) are the snapshots at 194.65 fs and 304.14 fs for excitation by optimal pulse, respectively. The two pink circles represent the positions of the two CIs.

and lead to the enhancement of the nσ* state population dramatically. As a consequence, in the case laser pulse excitation the WP density intend to keep proximity with the line along R at a planner geometry.

4.4 Summarizing remarks

In summary, it has been observed that the methyl photodissociation of thioanisole molecule can follow two paths (1) adiabatic path where the molecule dissociates along S-C stretching coordinate loosing planarity for torsional angle nonzero, (2) nonadiabatic path where the molecule dissociates along S-C stretching coordinate keeping the planarity of the molecule. The optimal pulse enforces the WP to prefer the nonadiabatic path for the

methyl dissociation of thioanisole while the vertical excitation promotes the adiabatic path. Consequently, the dissociation yield in the nσ* state asymptote is enhanced in presence of the optimal pulse but the vertical excitation leads to the enhancement in the ground state asymptote. An explicit dependence of the branching ratio on the initial vibrational excitation of the WP has been found in both types of excitation techniques. Initial excitation along the ϕ coordinate leads to an increase in the diabatic ground state asymptote but excitation along R mode promotes the nonadiabatic path to increase the dissociation through the nσ* asymptote. The optimal pulse vibrationally excites the $\pi\pi$* component of the WP along the S-C stretching coordinate to promote the nonadiabatic transition at S_1/S_2 and S_0/S_1 CIs so that the the system dissociates to the energetically lowest asymptote. Moreover, this satisfies the motivation of constructing the cost functional for obtaining the maximum yield with an expense of fluence of laser pulse as low as possible.

The two-dimensional potential energy surfaces considered in this study are well-suited for an initial investigation of methyl dissociation in thioanisole using a fully quantum mechanical approach. While this model Hamiltonian does not accurately reproduce the experimental lifetime of the $\pi\pi$* state, it serves as a minimal model that effectively captures the dissociation process in accord with experimental findings regarding the photodissociation pathway. Additionally, incorporating other vibrational modes could provide further insights into the methyl photodissociation of thioanisole. Specifically, a comparative study between this two-dimensional model and higher-dimensional models would help in identifying the vibrational mode responsible for the sluggishness of methyl photodissociation. Such an excercise is presently being undertaken.

CHAPTER 5

Suppression of N-H photodissociation of pyridinyl radical implementing frequency chirping: Utilization of coherent superposition principle

5.1 Introduction

The aspiration to control quantum mechanical phenomena has been alive since the inception of quantum mechanics. The discovery of the laser in the 1960s sparked hope for turning this aspiration into reality.[1, 2] Theoretical developments have since suggested that target states or desired outcomes can be achieved by optimizing laser pulses, an idea that continues to attract significant attention in contemporary research.[135, 136, 137] Among these advancements, OCT has emerged as the most effective theoretical framework for designing laser pulses to achieve specific photophysical objectives.[137, 138] In OCT, the frequency, amplitude, phase, and pulse shape are usually optimized to determine the optimal pulse.

Coherent control of photofragmentation using laser pulses leverages the superposition principle in its purest form, a phenomenon that cannot be achieved within the first-order perturbation limit.[139] In other words, controlling the state distribution of photofragments

is not feasible using continuous wave (cw) excitation in the weak-field limit.[12, 140, 141] However, it is noteworthy that the form of the WP can still be controlled using cw excitation.[142, 143] Although, when photodissociation is mediated via nonadiabtic transition, the momentum distribution or dissociation probability can be manipulated by phase-only shaped laser pulses implementing frequency chirping.[144, 145] Moreover, the nonadiabatic transition at the CI can also be tuned using cw laser pulse with either multi-frequency or single frequency component.[95]

Processes such as photosynthesis[146], vision[147], and light harvesting[148] rely on photochemical reactions. However, photochemical reactions also have adverse effects, including DNA damage[149] and degradation of solar cells.[150] Hence, the quantum control techniques must be designed for both the acceleration as well as suppression of the photochemical reaction, depending on the specific requirements of the application. The photochemical reactions can be manipulated using classical laser field[7, 137, 151, 152] or employing the photon-cavity.[153, 154]

Theoretical and experimental investigation of photodissociation dynamics of pyridinyl radical is very important because it plays an important role as the intermediate in photoinduced water splitting reaction where pyridine act as the photocatalysis.[89, 90, 91] Pyridinyl radical also can act as reducing agent for CO_2 in electrochemical catalysis.[155, 156, 157, 158, 159] The electronic structure and $\pi\sigma$-mediated N-H photodissociation dynamics were studied by Ehrmaier et al.[92], whose findings indicate that a three-mode, three-electronic-state model Hamiltonian is sufficient to describe the photodissociation process. The three modes include the N-H stretching coordinate (R), the out-of-plane bending of the H-atom θ, and the wagging mode (Q_9) and the three electronic states include the ground, $\pi\pi^*$, and $\pi\sigma^*$ state. Here, R serves as the reaction coordinate, θ acts as the coupling coordinate for the nonadiabatic interaction between the ground and $\pi\pi^*$ states, and Q_9 is the coupling coordinate for the nonadiabatic interaction between the $\pi\pi^*$ and $\pi\sigma^*$ states.

In our previous work, we have shown that the N-H photodissociation of pyridinyl radical

can be maximized by monochromatic laser pulse. Using a GA based OCT framework the amplitude, frequency, and shape of the monochromatic laser pulse has been optimized. More than 90% of the population was found to be dissociated via the $\pi\sigma^*$ state in presence of optimal pulse. In this work, the objective of the OCT calculation is quite the opposite of the previous case. Here, the focus is on controlling the lifetime of the $\pi\pi^*$ state by maximizing the overlap of the $\pi\pi^*$ WP component with the ground vibrational eigenfunction of $\pi\pi^*$ state.

5.2 Theory and methodology

The Hamiltonian in the dipole moment approximation is expressed as:

$$\hat{\boldsymbol{H}}(t) = \hat{\boldsymbol{H}}_0 - \hat{\boldsymbol{\mu}} \cdot \overrightarrow{E}(t), \tag{5.1}$$

where $\hat{\boldsymbol{H}}_0$ is the molecular Hamiltonian in the diabatic representation. This Hamiltonian, $\hat{\boldsymbol{H}}_0$, comprises the sum of the kinetic, $\hat{T}$, and potential, $\hat{\boldsymbol{V}}$, energy operators. The symbols $\hat{\boldsymbol{\mu}}$ and $\overrightarrow{E}(t)$ denote the molecular dipole moment and the external electric field from a laser, respectively. The system's time evolution is governed by the TDSE:

$$i\hbar\frac{\partial \boldsymbol{\psi}(t)}{\partial t} = \hat{\boldsymbol{H}}(t)\boldsymbol{\psi}(t), \qquad \boldsymbol{\psi}(t=0) = \boldsymbol{\phi}_0. \tag{5.2}$$

In this equation, the initial WP $\boldsymbol{\phi}_0$ is calculated using the pseudospectral method and represents the ground vibrational wave function of the system's ground state.

The goal is to determine the electric field $\overrightarrow{E}(t)$ that can drive the system from its initial state $\boldsymbol{\phi}_0$ to a final state $\boldsymbol{\psi}(t=T)$ that closely approximates a desired target state $\boldsymbol{\phi}_f$. This involves optimizing the time-dependent field to achieve a high degree of overlap between $\boldsymbol{\psi}(t=T)$ and $\boldsymbol{\phi}_f$, effectively steering the system's evolution to the target state. The optimal control can be formulated as the maximization of an electric field dependent cost functional,

$J[\overrightarrow{E}(t)]$ which is defined as

$$J[\overrightarrow{E}(t)] = J_s - \alpha_0 \int_0^T dt \left|\overrightarrow{E}(t)\right|^2 \tag{5.3}$$

In this work, the model Hamiltonian for the N-H photodissociation of the pyridinyl radical consists of three electronic states and three vibrational modes. The electronic states included are the ground state, the $\pi\pi^*$ state, and the $\pi\sigma^*$ state. The three vibrational modes considered are the N-H bond stretching coordinate R, which acts as the reaction coordinate; the out-of-plane bending coordinate of the hydrogen atom, θ and the normal mode Q_9, as detailed in Ref. 92. Accordingly, the total WP, $\boldsymbol{\psi}(t)$, is represented as:

$$\boldsymbol{\psi}(t) = \begin{pmatrix} \psi_0(t) \\ \psi_1(t) \\ \psi_2(t) \end{pmatrix}, \tag{5.4}$$

where $\psi_0(t)$, $\psi_1(t)$, and $\psi_2(t)$ correspond to the WPs associated with the ground, $\pi\pi^*$, and $\pi\sigma^*$ electronic states, respectively. The molecular Hamiltonian is represented as

$$\hat{\boldsymbol{H}}_0 = \hat{T}_N \mathbf{I}_3 + \begin{pmatrix} V_{00} & V_{01} & V_{02} \\ V_{10} & V_{11} & V_{12} \\ V_{20} & V_{21} & V_{22} \end{pmatrix}, \tag{5.5}$$

where $\hat{T}_N$ is the nuclear KE operator, and I_3 is the 3×3 identity matrix, representing that the KE acts equally on each electronic state. Here, V_{00}, V_{11}, and V_{22} are the diabatic potentials of the ground, $\pi\pi^*$, and $\pi\sigma^*$ states, respectively, while the off-diagonal terms V_{ij} (for $i \neq j$) represent the inter-state diabatic couplings. Detailed description of the KE, $\hat{T}_N$, and diabatic potential energy surfaces for the N-H photodissociation of pyridinyl radical has been given in the Ref. 92 and 160.

In the present work the molecule is excited to the only optically bright $\pi\pi^*$ state by an

external laser pulse therefore the molecular dipole moment matrix, $\hat{\boldsymbol{\mu}}$, in Eq. 5.1 can be expressed as

$$\hat{\boldsymbol{\mu}} = \begin{pmatrix} 0 & \mu_{01} & 0 \\ \mu_{10} & 0 & 0 \\ 0 & 0 & 0 \end{pmatrix}, \tag{5.6}$$

where the term μ_{01} is the TDM for the ground and $\pi\pi^*$ state which is considered as a constant (unity). It is valid approximation in a diabatic electronic basis, as the electronic character of the states remains consistent across the entire nuclear coordinate space within this framework.[94] The validation of this approximation was also further confirmed in our recent works on pyrrole and malonaldehyde.[87, 95, 96]

In this work, our objective is to design an optimal laser pulse that maximizes the lifetime of the $\pi\pi^*$ electronic state. Specifically, this optimal pulse should work to minimize nonadiabatic transitions between the $\pi\pi^*$ and $\pi\sigma^*$ states, as well as reduce the dissociation flux through the $\pi\sigma^*$ state. To achieve this target, the J_s term in Eq. 5.3 will be composed of two components. The first component will measure the overlap between $\psi(T)$, the WP at the final time T, and the target wave function ϕ_f, which represents the ground vibrational state of the $\pi\pi^*$ state. The second component will incorporate the time-accumulated flux for all three states, which inversely contributes to the cost functional. Together, these components guide the optimization process, favoring a laser pulse that maintains the system in the $\pi\pi^*$ state and minimizes both nonadiabatic transitions and unwanted dissociation. So, the term J_s can be written as

$$J_s = \left|\left\langle \psi(T)|\hat{O}_c|\phi_f \right\rangle\right|^2 + \frac{10^{-8}}{J_1} \tag{5.7}$$

where

$$J_1 = \sum_{i=0}^{2} \Phi_i(t) = \sum_{i=0}^{2} \frac{1}{\mu} \int_{t=0}^{t} Im\Big[\left\langle \psi_i \right| \frac{\partial \psi_i}{\partial R} \Big\rangle \Big|_{R=R_{flux}}\Big] d\tau. \tag{5.8}$$

Here, μ denotes the reduced mass along the R coordinate, which is associated with the N-H bond stretching mode, serving as the reaction coordinate for the dissociation process. The

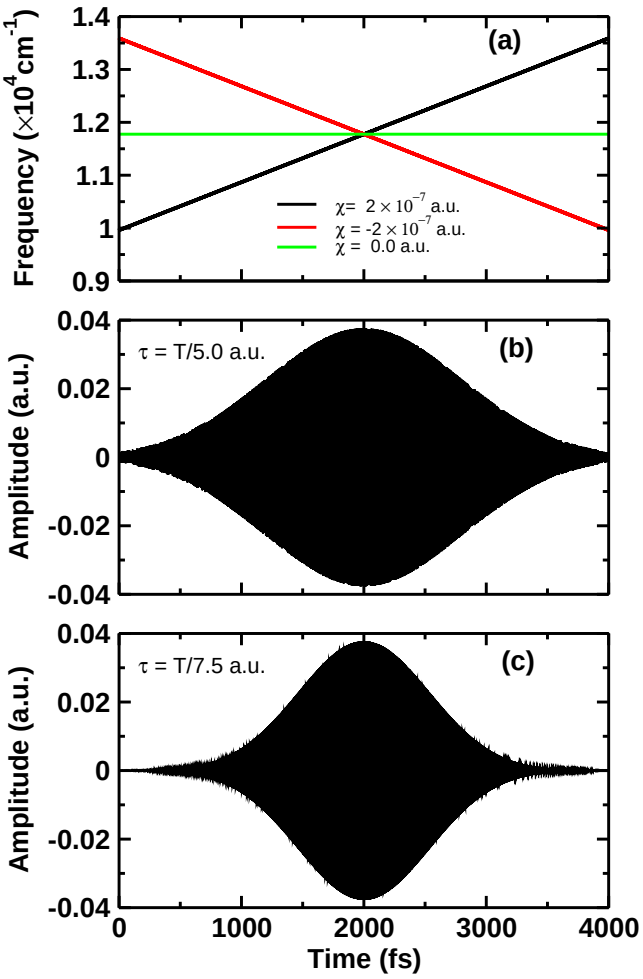

Figure 5.1: Temporal profile of laser pulses and corresponding frequency: (a) frequency variation over time, (b) and (c) laser pulse shapes with standard deviations of $\tau = T/5.0$ and $T/7.5$, respectively.

parameter R_{flux} specifies the position along the R coordinate at which the flux analysis is conducted, effectively marking the point beyond which dissociation is considered to occur.

The operator $\hat{O}_c$ is defined as a step function that acts as a boundary indicator for the $\pi\pi^* - \pi\sigma^*$ CI. Its value is set to unity up to the location of the CI and becomes zero beyond this point. Mathematically, it can be expressed as:

$$\hat{O}_c(R) = \begin{cases} 1, & \text{for } R \leq R_{CI} \\ 0, & \text{for } R > R_{CI} \end{cases} \tag{5.9}$$

where R_{CI} is the coordinate value at the CI. This operator helps to distinguish regions within the potential energy surface, ensuring that the overlap is selectively maximized within the equilibrium region of the $\pi\pi^*$ state, while inhibiting nonadiabatic transitions through the $\pi\pi^* - \pi\sigma^*$ CI.[144, 145]

The laser field considered in the present work is a linearly chirped pulse with a gaussian envelop, defined as,

$$\overrightarrow{E}(t) = \overrightarrow{E}_0 \exp\left[-\frac{(t-t_0)^2}{2\tau^2} - i(t-t_0)\Big(\omega_0 + \chi\frac{t-t_0}{2}\Big)\right], \tag{5.10}$$

where:

- $\overrightarrow{E}_0$ is the amplitude of the electric field,
- t_0 is the central time of the pulse,
- τ represents the standard deviation of the pulse shape (related to the Gaussian envelope width),
- ω_0 is the central frequency of the pulse,
- $\chi/2$ is the chirp rate, determining the rate of frequency change over time.

This form of the electric field represents a Gaussian-modulated pulse with a time-dependent frequency, allowing for control over the frequency sweep of the pulse. If χ is negative, the frequency of the pulse decreases over time, creating what is known as a downwardly chirped pulse. Conversely, if χ is positive, the frequency increases with time, and the pulse is referred to as an upwardly chirped pulse. This chirping allows for selective control over the interaction dynamics by adjusting the frequency sweep direction in the laser field.

The GA has been employed to determine the optimal pulse which maximizes the cost functional, J. The parameters in the Eq. 5.10 namely, the amplitude $\overrightarrow{E}_0$, the central frequency ω_0, chirping rate χ, and width of the pulse, τ are varied within a predefined range of values [see Table 5.1]. Through iterative exploration, the GA efficiently navigates this

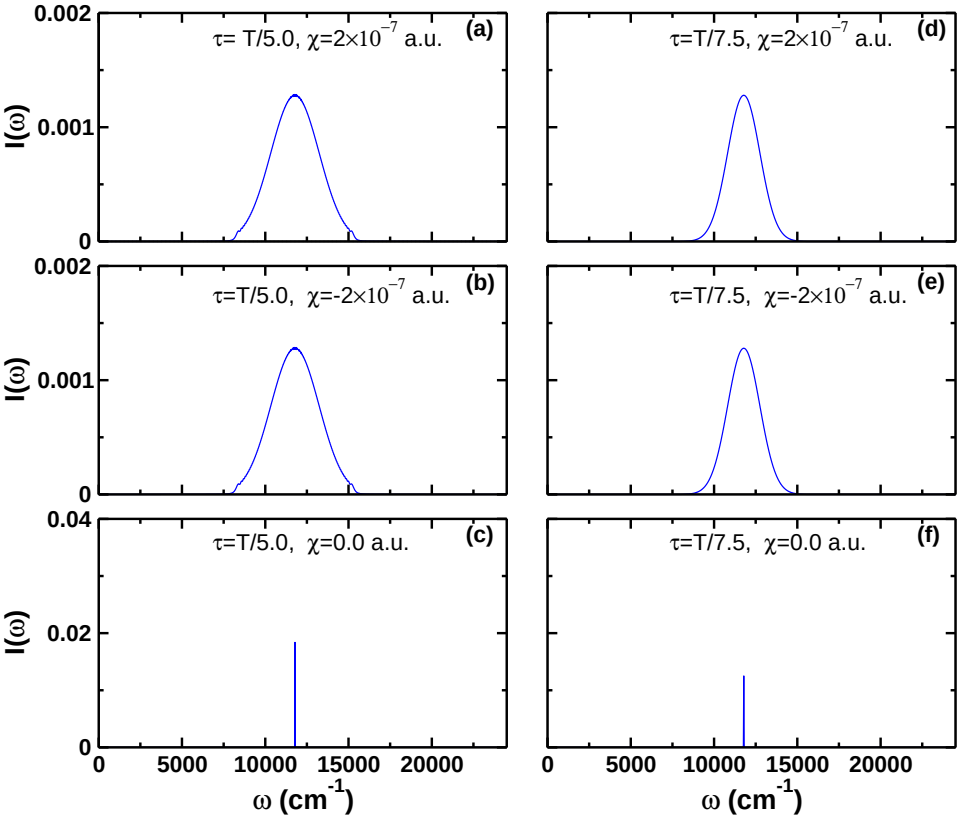

Figure 5.2: Spectral profile of the six laser pulses with varying chirp rates, χ, and standard deviation of the gaussian envelope, τ, as mentioned in panels (a-f).

parameter space to identify the pulse configuration that achieves the desired optimization objectives, thereby maximizing the cost functional. The parameter t_0 is set to a constant

Table 5.1: Parameters used in the optimization of the laser pulse.

Parameter	**Description**	**Value[a.u.]**
$\overrightarrow{E}_0$	Amplitude of electric field	0.0151-0.0755
ω_0	Central frequency	0.0236-0.059
χ	Chirping rate	-3×10^{-7} - 3×10^{-7}
τ	Width of pulse	16655.16 - 27758.6

value of $T/2$, where $T = 138793.0$ a.u. represents the total duration of the laser pulse. Consequently, t_0 defines the central time of the pulse as the midpoint of the total duration, occurring at $T/2$.

5.3 Results

Dynamics of the Pyridinyl photodissociation with chirped pulse

In a test, the N-H photodissociation dynamics are investigated using six laser pulses, each with different chirping rates and pulse envelope widths [cf. Table 5.2]. The central frequency is set to 11775.7 cm^{-1},corresponding to the 1.46 eV energy gap between the $\pi\pi^*$ and ground state. The amplitude is fixed at 0.0377 a.u., placing it in the weak field region to prevent unnecessary photoionization or other non-physical processes [cf. Fig. 5.1]. The spectral profiles of the six laser pulses are depicted in Fig. 5.2. For non-zero chirp rate χ, the spectra are broad in frequency space, encompassing continuously varying frequency components whereas for $\chi = 0$, the spectrum displays a sharp peak at the central frequency which corresponds to a monochromatic laser pulse. The total duration, T, of these laser pulses is 4000 fs.

Table 5.2: Parameters of laser pulses used for the N-H photodissociation dynamics test.

Pulse Number	**Chirping Rate (χ)**	**Pulse Width (τ)**
1	2×10^{-7}	T/5.0
2	-2×10^{-7}	T/5.0
3	0.0	T/5.0
4	2×10^{-7}	T/7.5
5	-2×10^{-7}	T/7.5
6	0.0	T/7.5

The diabatic electronic populations of the three electronic states are shown over time under the influence of six laser pulses (see Fig. 5.3). The population dynamics exhibit significant variation with different chirp rates, χ. When $\chi = 2 \times 10^{-7}$, corresponding to a linear increase in pulse frequency over time, the ground state population decreases gradually. In contrast, for $\chi = -2 \times 10^{-7}$, the population decreases more rapidly, with the fastest decline observed at $\chi = 0.0$. Similarly, there is a remarkable impact of the chirping rate on the dynamics of $\pi\pi^*$ state. For positively chirped pulse the $\pi\pi^*$ state population

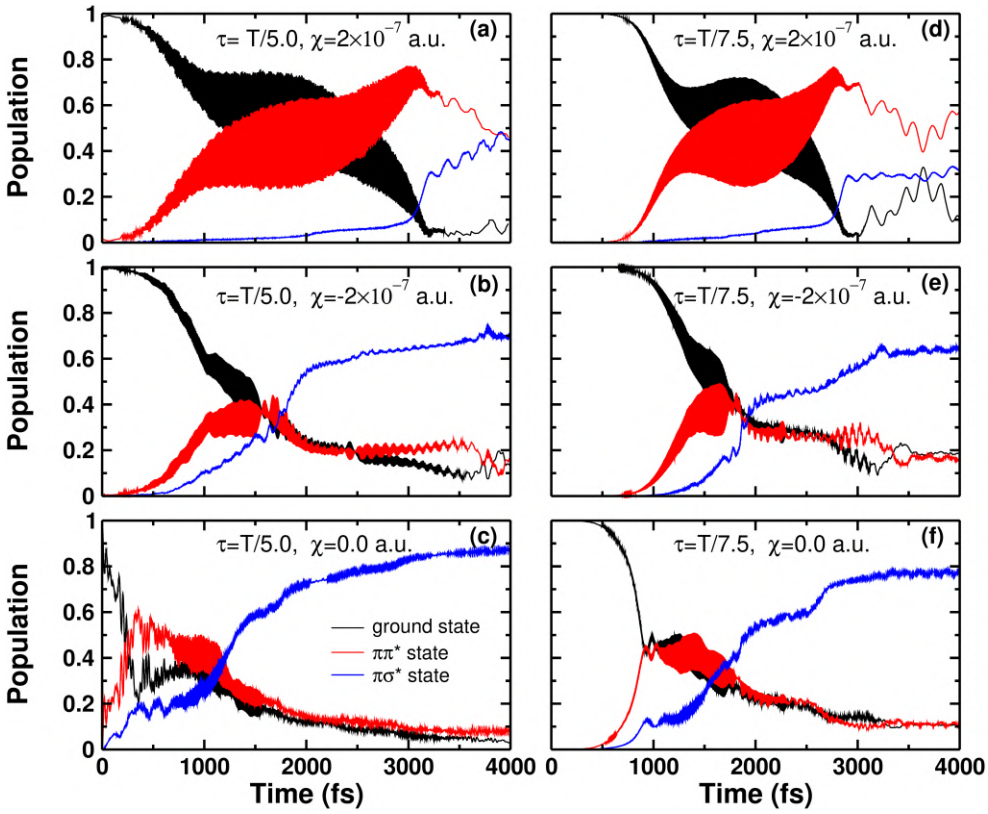

Figure 5.3: The diabatic electronic population dynamics of the ground, $\pi\pi^*$, and $\pi\sigma^*$ states are shown over time in the presence of six laser pulses with different chirp rates, χ, and the standard deviation of the Gaussian envelope, τ, as depicted in panels (a-f).

increases up to ∼3000 fs whereas, for the negatively chirped and monochromatic laser pulses, the population does not sustain growth for such an extended duration. The $\pi\pi^*$ state population increases up to only ∼1200 fs for negatively laser pulse while it starts decreasing rapidly after an instant increase in presence of monochromatic laser pulse. The implementation of the linear chirp in the laser pulse has most significantly influenced the nonadiabatic transition occurring at the $\pi\pi^*/\pi\sigma^*$ CI (CI-1) and, consequently, it is reflected in the $\pi\sigma^*$ state dynamics also. The nonadiabatic transition through the CI-1 occurs more slowly in the presence of positively chirped laser pulse compared to negatively chirped and monochromatic pulses. Therefore, the WP gets excited to the $\pi\pi^*$ state in portions with time and is not immediately transferred to the repulsive $\pi\sigma^*$ potential energy surface by nonadiabtic transition through CI-1 for $\chi = 2 \times 10^{-7}$. Consequently, the population on the $\pi\sigma^*$ state remains below 10% until 3000 fs. This indicates that the positively chirped pulse directs the WP components to move towards the equilibrium rather than propelling them toward dissociation. On the other hand the negatively chirped and monochromatic laser pulse does not hinders the nonadiabatic transition at CI-1. For $\chi = -2 \times 10^{-7}$ the population of $\pi\sigma^*$ population increases steadily until ∼2000 fs, after which the growth rate slows down considerably. In the case of $\chi = 0.0$ the $\pi\sigma^*$ population increases rapidly from the onset, and by the end of the dynamics, nearly 88% of the population is transferred to the $\pi\sigma^*$ state. The effect of the chirped rate follows the same trend for both the values of τ (see Fig. (a-f)).

Fig. 5.4 represents the time accumulated flux through the ground, $\pi\pi^*$, and $\pi\sigma^*$ asymptote with respect to time. Panel (a) illustrates the flux profile for $\chi = 2 \times 10^{-7}$, showing that the dissociation flux through the $\pi\sigma^*$ state remains below 5% up to 2000 fs. After that, it begins to increase slowly and, by the end of the laser pulse duration, it reaches nearly 39%. As discussed previously, the positively chirped laser pulse induces a sluggish nonadiabatic transition, preventing the WP from efficiently accessing the $\pi\sigma^*$ state, thereby reducing the dissociation yield. For $\chi = -2 \times 10^{-7}$ laser pulse, the dissociation yield via the $\pi\sigma^*$

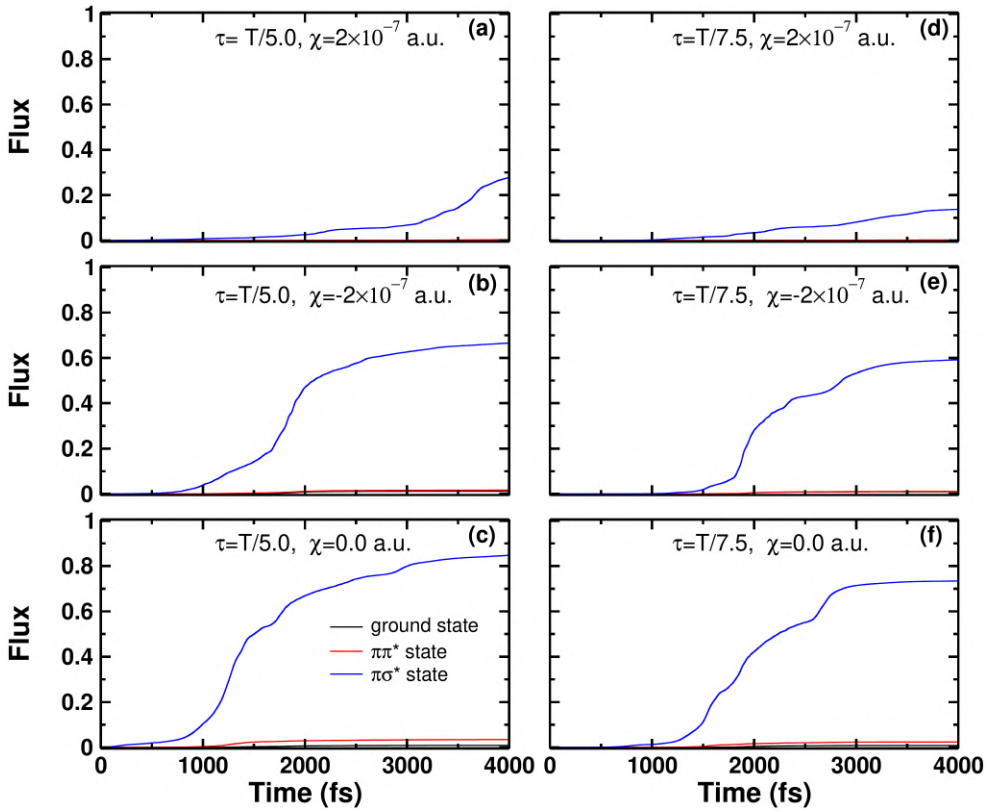

Figure 5.4: The dissociation flux through the ground, $\pi\pi^*$, and $\pi\sigma^*$ asymptotes are shown over time in the presence of six laser pulses with different chirp rates, χ, and the standard deviation of the Gaussian envelope, τ, as depicted in panels (a-f).

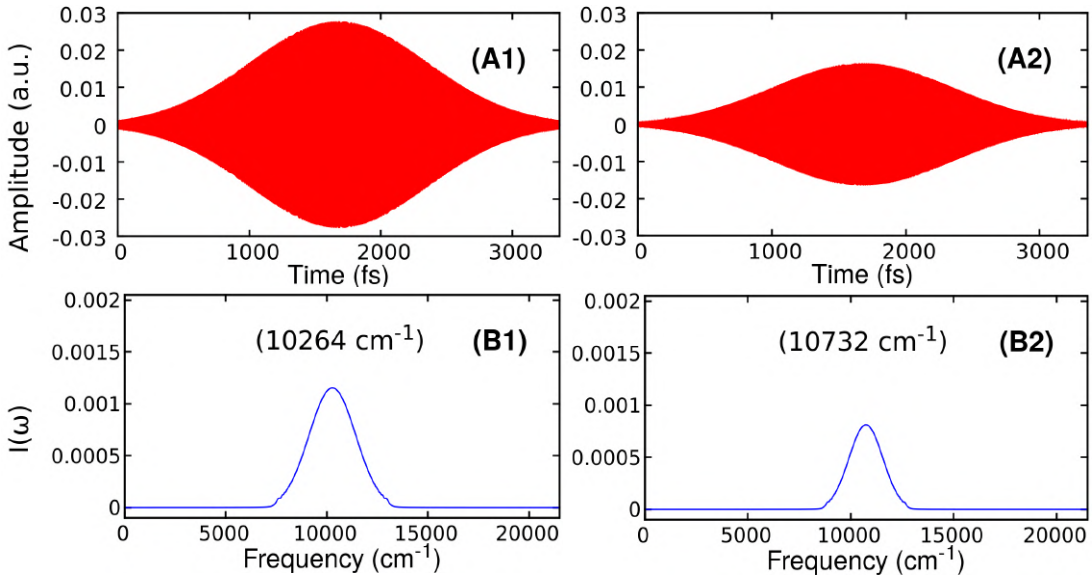

Figure 5.5: Temporal and frequency profiles of the optimal laser pulses obtained using the GA. Panels (A1) and (A2) show the temporal profiles of Type-1 and Type-2 laser pulses, respectively, while panels (B1) and (B2) display their corresponding frequency profiles.

state is comparatively high and $\sim$67% of the population gets dissociated by the end of the pulse duration. The dissociation yield for monochromatic laser pulse is illustrated in panel (c), where $\sim$86% of the population dissociates via $\pi\sigma^*$ state. Additionally, a small fraction ($\sim$5%) dissociates through the excited state, $\pi\pi^*$, dissociation channel. The other three panels (d-f) present the flux profiles for the laser pulse envelope with a standard deviation of $\tau = T/7.5$, corresponding to the same chirp rates: $\chi = 2 \times 10^{-7}$, -2×10^{-7}, and 0.0 au. The effect of the chirping rate is similar to that observed for $\tau = T/5.0$, where the dissociation yields via the $\pi\sigma^*$ state are approximately 14%, 60%, and 74%, respectively. However, the total yields are slightly lower than those for the corresponding χ values with $\tau = T/5.0$. This reduction can be attributed to the slower rise in the pulse amplitude during the leading edge and the narrower full-width-half-maximum (FWHM) of the pulses compared to those with $\tau = T/5.0$.

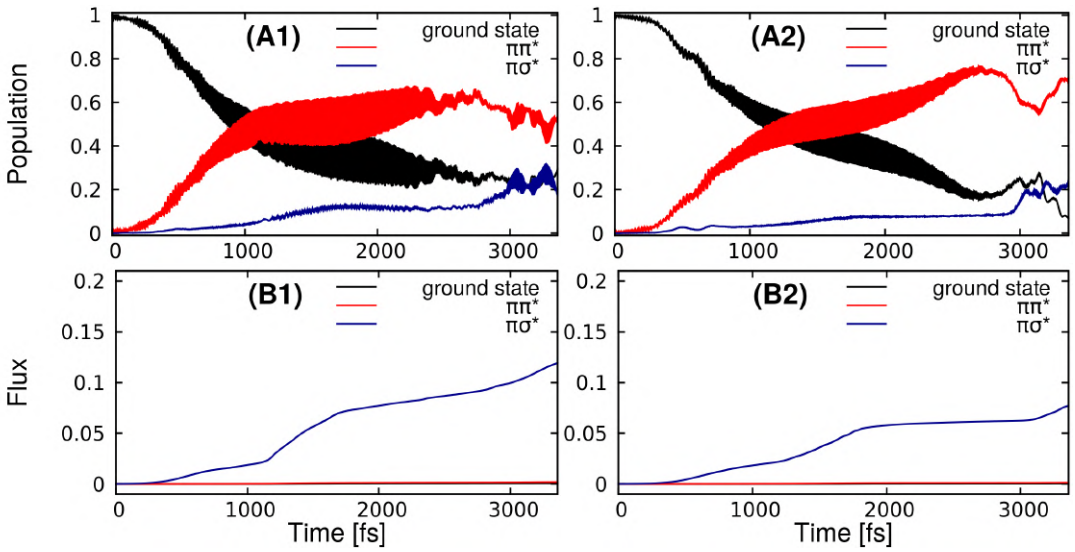

Figure 5.6: The diabatic electronic population dynamics and time-accumulated flux over time under optimized laser pulses. Panels (A1) and (A2) are the time-dependent diabatic population dynamics driven by Type-1 and Type-2 optimal laser pulse, respectively, while panels (B1) and (B2) display the time-accumulated flux obtained by the action of these two pulses, respectively.

OCT calculation to maximize the life time of $\pi\pi^*$ state

Two types of quantum control calculations have been performed with a motivation of the maximization of the lifetime on the $\pi\pi^*$ state simultaneously minimizing the dissociation flux through the $\pi\sigma^*$ state. To account this problem the cost functional (see Eq. 5.3) has been maximized using GA within the parameter ranges given in Table 5.1. In the Type-1 calculation, the optimal pulse is determined by optimizing the amplitude, $\overrightarrow{E}(t)$, central frequency, ω_0, and chirping rate, χ for fixed width of the pulse, $\tau = 27758.6$ a.u. (see panel (A1) in Fig. 5.5). In the Type-2 calculation, an additional parameter, the pulse width τ, was also optimized (see panel (A2) in Fig. 5.5). The values of the optimized parameters of these two types of calculations are summarized in Table 5.3.

The diabatic population of the three electronic states in the presence of the two optimal pulses is shown in Fig. 5.6. The Type-1 laser pulse excites the ground vibrational WP gradually from the ground electronic state to the $\pi\pi^*$ state in the FC region (see panel (A1)). This pulse excites the WP components more slowly than the monochromatic laser pulse

Table 5.3: Optimized parameters obtained from the GA.

Optimized values of parameters obtained from Type-1 calculation	
Amplitude, $\overrightarrow{E}(t)$	2.7788565$\times 10^{-2}$ a.u.
Central frequency, ω_0	5.3307845$\times 10^{-2}$ a.u.
Chirping rate, χ	-1.8915$\times 10^{-7}$ a.u.
Optimized values of parameters obtained from Type-2 calculation	
Amplitude, $\overrightarrow{E}(t)$	1.65137$\times 10^{-2}$ a.u.
Central frequency, ω_0	4.8877$\times 10^{-2}$ a.u.
Chirping rate, χ	-1.352$\times 10^{-7}$ a.u.
Width of the pulse, τ	27758.6 a.u.

because of the frequency chirping effect[160]. At the end of the pulse duration, $\sim$70$\%$ of the ground state populations are excited to the excited states. The plot illustrates an increase in the $\pi\pi^*$ population up to 1000 fs, during which the $\pi\sigma^*$ state population remains below 4$\%$. This indicates that within this timeframe, the portion of the wave packet excited from the ground state to the $\pi\pi^*$ state does not undergo a nonadiabatic transition to the $\pi\sigma^*$ state at CI-1. Instead, it accumulates in the FC region of the $\pi\pi^*$ state. This behavior is a direct consequence of frequency chirping employed in the laser pulse. Beyond this initial period, the population of the $\pi\pi^*$ state continues to increase, although comparatively more slowly, to $\sim$ 2500 fs. In this interval, the nonadiabatic transition at CI-1 occurs comparatively at faster rate and consequently, the $\pi\sigma^*$ state starts acquiring some population. Afterwards, the population of $\pi\sigma^*$ state is increased and $\pi\pi^*$ state population decreases. The time accumulated flux through the three asymptotes is plotted in panel (B1). The dissociation flux via $\pi\sigma^*$ state remains nearly zero up to $\sim$200 fs and then starts increasing very slowly and at the end of the pulse duration it reaches $\sim$12$\%$ only which is significantly lower than the dissociation flux observed with a monochromatic laser pulse. No dissociation flux has been obtained through the ground state and the $\pi\pi^*$ channels. Therefore, the objective of maximizing the lifetime of the $\pi\pi^*$ state while minimizing the dissociation of N-H bond has been successfully achieved.

The diabatic population of the three states in the presence of Type-2 laser pulse is shown

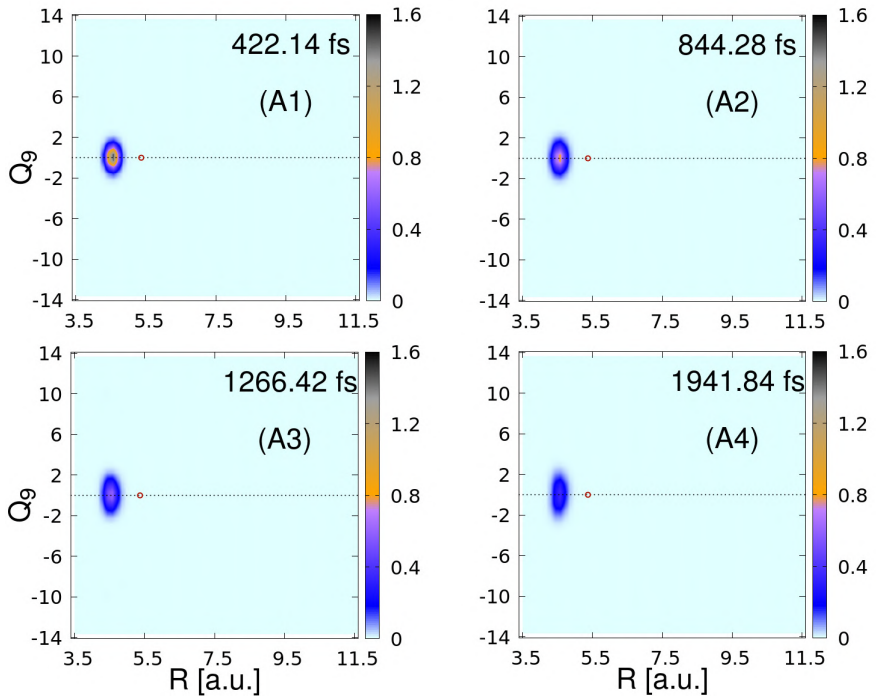

Figure 5.7: Snapshots of probability densities for the ground state WP component in $R-Q_9$ space at different times during the field driven dynamics.

in panel (A2) in Fig. 5.6. Similar to the Type-1 case, the ground state population decreases gradually with time up to approximately 2634.3 fs and by this time $\sim$85% of the population has been transferred to the excited states. Subsequently, the $\pi\pi^*$ population exhibits a slight oscillatory growth before decreasing to approximately 7%. This indicates that the Type-2 optimal pulse excites the WP more efficiently than the Type-1 pulse. The $\pi\pi^*$ state population increases gradually with time up to $\sim$1000 fs and continues to increase up to $\sim$2634.3 fs almost in the same rate unlike the Type-1 case. Within this period, the $\pi\sigma^*$ population grows very slowly and reaches $\sim$8% only at $\sim$2634.3 fs. This suggests that, in the presence of the Type-2 laser pulse, the $\pi\pi^*$ WP component accumulates in the FC region of the corresponding state more effectively than it does under the influence of the Type-1 laser. The time-accumulated flux plot demonstrates that the flux via the $\pi\sigma^*$ state is suppressed more effectively by the Type-2 laser pulse compared to the Type-1 pulse. The total dissociation yield on the $\pi\sigma^*$ state asymptote is $\sim$7.7% only which is remarkably lower than the dissociation yield observed with monochromatic laser[160] and even lower than

the dissociation yield for Type-1 pulse.

5.3.1 Time dependent probability densities

In order to get an insight of the mechanism of the dynamics under the influence of the optimal laser pulses the snapshots of the probability densities of the ground, $\pi\pi^*$, and $\pi\sigma^*$ state WP components at different times are represented in Figs. 5.7-5.12. The snapshots of the probability densities are taken at 422.14, 844.28, 1266.42, and 1941.84 fs for all the three states in the two dimensional reduced spaces, $R - Q_9$ and $R - \theta$. The probability densities in the two dimensional space are calculated by the following formulas

$$\begin{aligned} P_{RQ_9}(R, Q_9) &= \int \psi(R, \theta, Q_9)^* \psi(R, \theta, Q_9)\, d\theta, \\ P_{R\theta}(R, \theta) &= \int \psi(R, \theta, Q_9)^* \psi(R, \theta, Q_9)\, dQ_9. \end{aligned} \tag{5.11}$$

The probability densities of the ground electronic states represent that it remains concentrated in the FC region only and the density decreases gradually with time (see Fig. 5.7 and 5.10). It is also noticeable that no nodal pattern has been appeared over time within the probability density plots neither along reaction coordinate, R, nor along the coupling coordinates, Q_9 and θ, for both $R - Q_9$ and $R - \theta$ space. Additionally, the probability density of the ground state shrinks over time rather than diffusing (cf. panels (A1,A1,A3,A4) in Fig. 5.7 and 5.10) On the other hand, when the monochromatic laser, i.e. 3^{rd} and 6^{th} pulse in table 5.2, is applied the probability density gets diffused and nodal pattern along the coupling coordinate, Q_9, emerges with time. The ground state WP component was also found to be diffuse, and nodal pattern was also present, when an optimal laser pulse with a single frequency was applied, as demonstrated in our previous work.[160]

Figures 5.8 and 5.11 represent the snapshots of probability densities of $\pi\pi^*$ WP component in $R - Q_9$ and $R - \theta$ spaces, respectively. Initially, the $\pi\pi^*$ WP component remains diffused along the Q_9 coordinate with multiple nodal lines along the coordinate, R (cf. panel

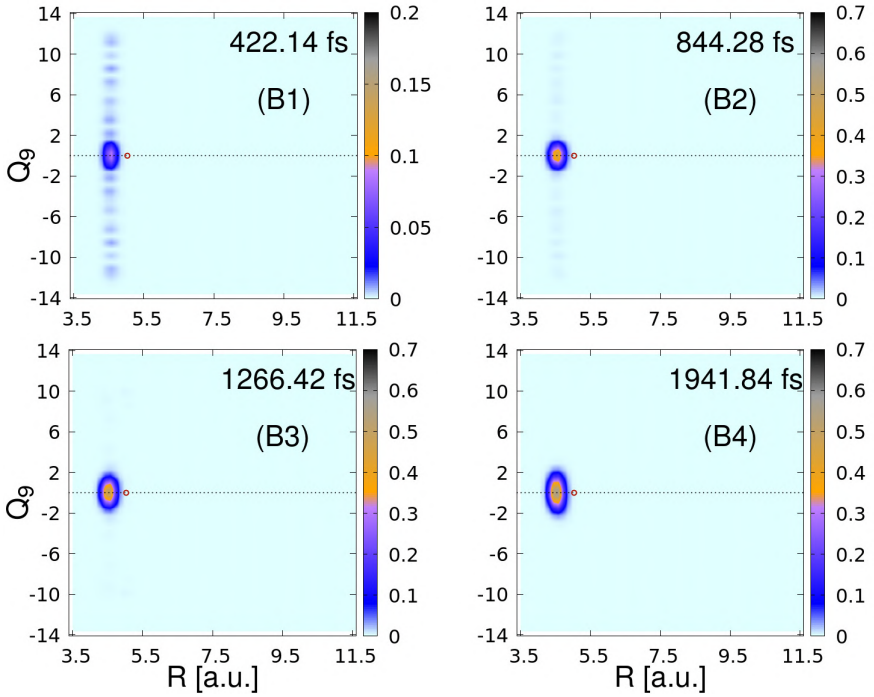

Figure 5.8: Snapshots of probability densities for the $\pi\pi^*$ state WP component in $R - Q_9$ space at different times during the field driven dynamics.

(B1) of Fig. 5.8). The probability density is observed to be symmetric about the $Q_9 = 0$ line, extending up to $Q_9 \sim \pm 13$ a.u. The probability density is highest at the $Q_9 = 0$ and it decreases gradually towards the larger $\pm Q_9$ values. This pattern of WP probability distribution along the Q_9 coordinate persists during the dynamics (see panel (B2) of Fig. 5.8) while the diffuseness decreases, and the wavepacket becomes increasingly concentrated in the FC region (cf. panel (B2,B3,B4) in Fig. 5.8). Also in the $R - \theta$ space the wavepacket remains in the FC region initially and the amplitude increases with time because of gradual excitation of ground state wavpacket to the $\pi\pi^*$ state by the optimal pulse. It is a common phenomenon that when CIs are located near the equilibrium region, the excited WP tends to undergo nonadiabatic transitions, provided there are no significant energy barriers in the way.[73, 92, 160] Interestingly, in both reduced-dimensional representations, the $\pi\pi^*$ WP component does not cross CI-1. This observation suggests that the optimal chirped frequency laser pulse effectively suppresses the nonadiabatic transition.

Figures 5.9 and 5.12 illustrate the $\pi\sigma^*$ WP probability densities is the two dimensional

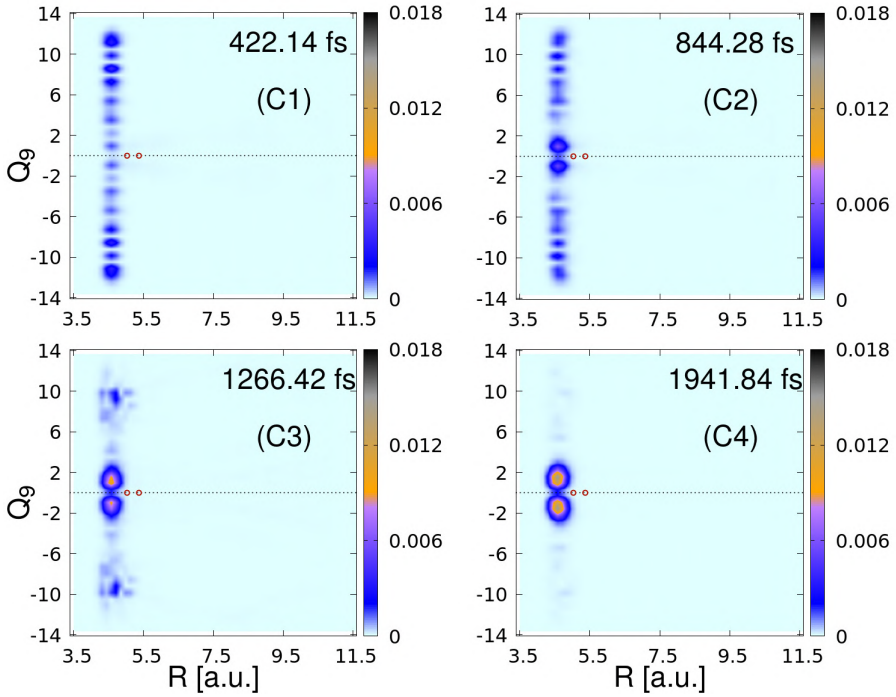

Figure 5.9: Snapshots of probability densities for the $\pi\sigma^*$ state WP component in $R - Q_9$ space at different times during the field driven dynamics.

spaces. In presence of the optimal chirped laser pulse, the $\pi\sigma^*$ WP probability densities also follows the same trend. Initially, it displays a diffused nature along the Q_9 coordinate, with multiple nodal patterns along R (see panel C1 of Fig. 5.9). It is observed that the probability density is symmetric with respect to the $Q_9 = 0$ line and extended up to $Q_9 \sim \pm 13$ a.u. The probability density is highest in the larger Q_9 and it decreases gradually towards the $Q_9 = 0$ line. Subsequently, this distribution along the Q_9 coordinate changes, eventually reversing its pattern while maintaining symmetry with respect to the $Q_9 = 0$ line (see panel (C2) of Fig. 5.12). Over time, the diffuseness decreases and the $\pi\sigma^*$ WP density becomes increasingly concentrated in FC region (cf. panels (C3) and (C4) in Fig. 5.12). In the $R - \theta$ space, the WP density remains localized in the FC region and the probability density amplitude increases with time because of gradual excitation of ground state WP to the $\pi\pi^*$ state by the optimal pulse (cf. panels (C1)-(C4) of Fig. 5.12). The $\pi\sigma^*$ WP component also cannot undergo the nonadiabatic transition at the nearest CI, CI-1, due to frequency chirping implemented in the optimal pulse.

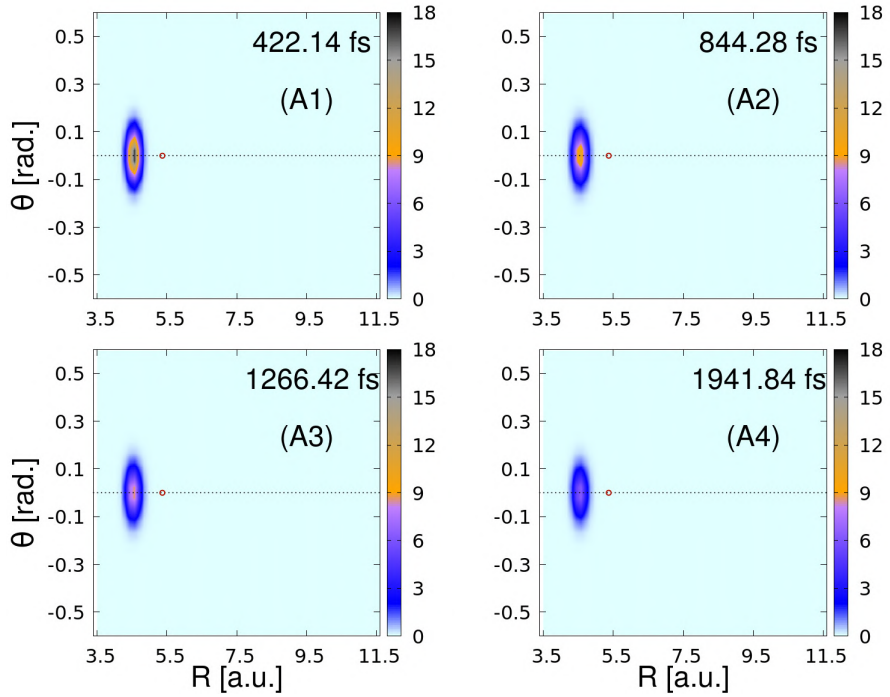

Figure 5.10: Snapshots of probability densities for the ground state wavepacket component in $R-\theta$ space at different times during the field driven dynamics.

In order to analyze the effect of the frequency chirping in the photodissociation dynamics of pyridinyl we can consider the analytical formulation of the WP dynamics of the three states within the framework of first order perturbation theory (see APPENDIX-C). The Eq. C.6 represents the time evolution of the three WP components with time in presence of an electromagnetic (e.m.) field. The $\pi\pi^*$ state WP component, i,e. $\psi_1(t)$, consists of two parts where first part indicates the excitation of the ground state WP by the e.m. field the second part indicates the portion of the $\pi\sigma^*$ WP component undergoes nonadibatic transition between the $\pi\pi^*$ and $\pi\sigma^*$ state. Since our target in the quantum control studies is the maximization of the overlap of $\psi_1(t)$ with the ground vibrational eigenfunction of $\pi\pi^*$ state, the excitation by the e.m. field will primarily be considered to illustrate the chirping effect in the present work. Without loosing any generality, the target vibrational state on the $\pi\pi^*$ electronic state can be considered as a superposition of the vibrational eigenstates, $\zeta_{1,n}$,

and it can be written as[161]

$$\phi_f(T) = \sum_n a_n e^{-i\phi_n(T)} \zeta_{1,n}. \tag{5.12}$$

After separating the preparation stage from the subsequent dynamics this equation recasts as

$$\phi_f(T) = \sum_n a_n e^{-\epsilon_{1,n}T/\hbar} e^{-i\phi_n} \zeta_{1,n}. \tag{5.13}$$

If the optimal laser pulse excites a coherent superposition of eigen states of $\pi\pi^*$ state at time t, then the WP component of the corresponding electronic state can be expressed as

$$\psi_1(t) = \sum_n c_n e^{-\epsilon_{1,n}t/\hbar} \zeta_{1,n}. \tag{5.14}$$

In order to determine the coefficient c_n, let us multiply the $\psi_1(t)$ in Eq. C.6 by $\langle\zeta_{1,n}|$

$$\begin{aligned} \langle\zeta_{1,n}|\psi_1(t)\rangle &= -\frac{i}{\hbar}\int_0^t \langle\zeta_{1,n}|e^{-\frac{i}{\hbar}H_{11}t}(-\mu_{01}E)e^{-\frac{i}{\hbar}H_{00}t}|\zeta_{0,0}\rangle dt \\ c_n &= \tilde{E}(\omega_{1,n}-\omega_{0,0})\langle\zeta_{1,n}|\mu_{01}|\zeta_{0,0}\rangle \end{aligned} \tag{5.15}$$

where $\tilde{E}(\omega_{1,n}-\omega_{0,0})$ and $\langle\zeta_{1,n}|\mu_{01}|\zeta_{0,0}\rangle$ are the Fourier component of the field at the frequency, $\omega_{1,n}-\omega_{0,0}$, and FC factor, respectively. At the end of the pulse duration, i.e. at time T, we will have $\psi_1(T) = \phi_f(T)$. From this condition we can finalize that

$$\begin{aligned} a_n e^{-i\phi_n} &= \tilde{E}(\omega_{1,n}-\omega_{0,0})\langle\zeta_{1,n}|\mu_{01}|\zeta_{0,0}\rangle \\ \tilde{E}(\omega_{1,n}-\omega_{0,0}) &= \frac{a_n e^{-i\phi_n}}{\langle\zeta_{1,n}|\mu_{01}|\zeta_{0,0}\rangle} \end{aligned} \tag{5.16}$$

and the target state

$$\phi_f(T) = \sum_n \tilde{E}(\omega_{1,n}-\omega_{0,0})\langle\zeta_{1,n}|\mu_{01}|\zeta_{0,0}\rangle e^{-\epsilon_{1,n}T/\hbar}\zeta_{1,n}. \tag{5.17}$$

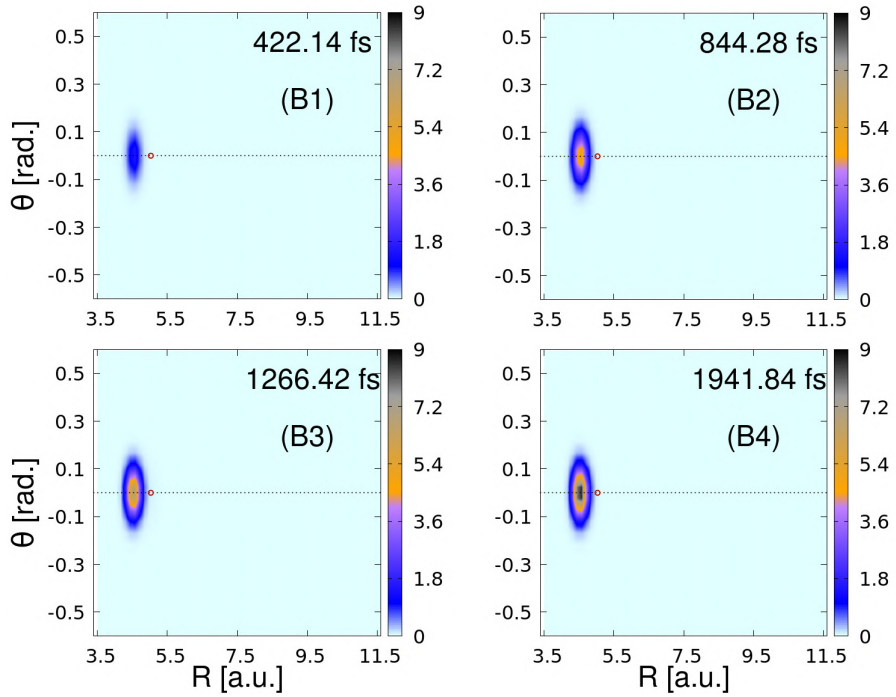

Figure 5.11: Snapshots of probability densities for the $\pi\pi^*$ state WP component in $R-\theta$ space at different times during the field driven dynamics.

For a general potential energy surface the period of vibration becomes longer for higher energy components. Therefore, to focus entire WP in the FC region at the same time on the $\pi\pi^*$ potential energy surface, the higher energy components have to be excited before the lower energy components.[162, 163] To meet this requirements, Eq. 5.17 suggests that the optimal pulse has to be designed is such a way so that the frequency should be swiped from higher to lower, i.e. the pulse should have downwardly chirped or negatively chirped frequency. From the GA base quantum control calculation also we obtained negatively chirped pulse (cf. Table 5.3). It is also observed that the laser pulse excited the higher energy component along the Q_9 mode at first then with time the WP relaxed to the ground vibrational state at the same time to get focused in the FC region (see Fig. 5.8 and 5.9).

The oscillatory nature of the time-dependent diabatic population of ground and $\pi\pi^*$ state (cf. Fig. 5.6) can be attributed to the second terms of the $\psi_0(t)$, $\psi_1(t)$, and both the terms of $\psi_2(t)$ in Eq. C.6. This behavior arises from the nonadiabatic coupling, V_{12}, in the FC region, which causes a portion of the WP component to oscillate between the $\pi\pi^*$

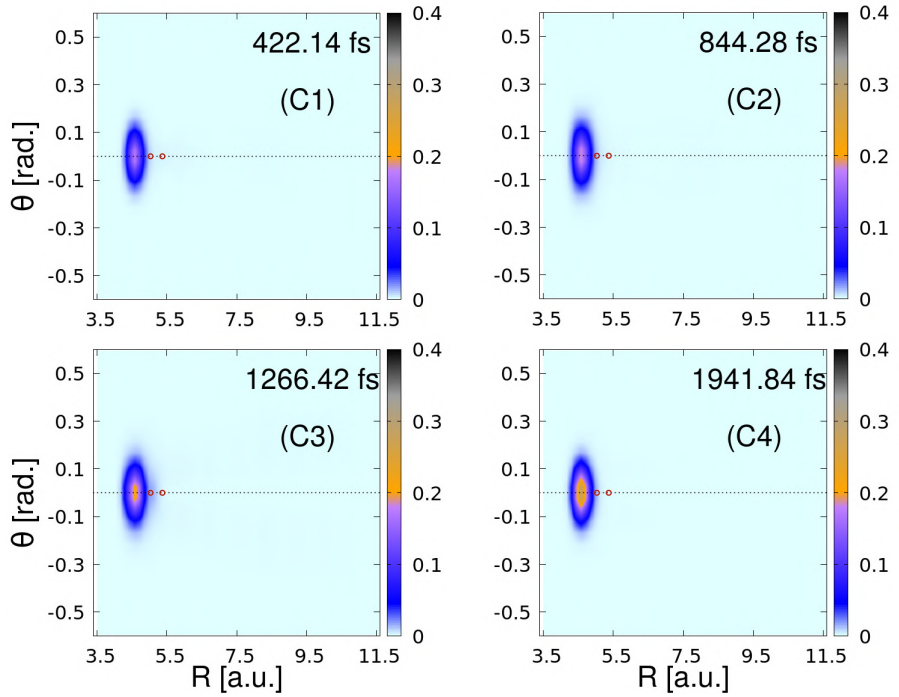

Figure 5.12: Snapshots of probability densities for the $\pi\sigma^*$ state WP component in $R-\theta$ space at different times during the field driven dynamics..

and $\pi\sigma^*$ states. Similarly, due to the nonadiabatic coupling V_{02}, another portion of the WP component oscillates between the $\pi\sigma^*$ and ground states. The oscillatory nature is more prominent in the present study than out previous works where monochromatic laser pulse had been implemented.[87, 88, 95, 160] The optimal laser pulse excites the initial WP coherently to a larger number vibrational eigenstates of the $\pi\pi^*$ state, facilitated by the broad frequency range of the pulse (cf. (B1) and (B2) in Fig. 5.5). Due to frequency chirping, the excited vibrational WP components interfere constructively, causing them to relax to the ground vibrational level of the $\pi\pi^*$ state and remain confined in the FC region. As a result, the WP spends an extended time in the FC region, leading to pronounced oscillations between the $\pi\pi^*$ and $\pi\sigma^*$ states due to the nonadiabatic coupling, V_{12}. In contrast, under a monochromatic laser pulse, the lack of coherent superposition among the excited vibrational WP components prevents the WP from remaining in the FC region of the $\pi\pi^*$ state. Instead, the WP becomes diffused along the R mode and undergoes nonadiabatic transitions at CI-1.[164]

5.4 Summarizing remarks

In summary, the $\pi\sigma^*$-mediated N-H photodissociation of the pyridinyl radical can be effectively suppressed by implementing linear frequency chirping in the design of the optimal laser pulse. A frequency-chirped laser pulse incorporates a broad range of frequency components, enabling coherent excitation of the vibrational WP from the ground state to multiple vibrational levels of the optically bright $\pi\pi^*$ state. The GA based OCT calculation designs the optimal laser pulse where frequency is downwardly chirped. So, the optimal pulse starts with higher frequency component and with time it decreases linearly to lower frequency components. Consequently, the higher vibrational energy components with higher vibrational period is excited first and with time gradually the component with lower vibrational period gets excited coherently to $\pi\pi^*$ state in the FC region. This coherent superposition of vibrational WP components creates a pseudo-stationary vibrational state, effectively trapping the WP.

The initial test calculations using six laser parameter sets provided a preliminary understanding of addressing the current problem. The results from the quantum dynamics calculation in presence of that six laser pulses suggest that incorporation of frequency chirping can effect the nonadiabtic transition at CI-1 and consequently, the dissociation yield.[144, 145] Based on these insights, the parameters of the pulse and their ranges were defined for the OCT calculations to maximizing the life time of the $\pi\pi^*$ state. The optimal laser pulse, comprised of downwardly chirped frequency, trapped vibrational WP in the FC region utilizing the interference between the excited WP components by coherent superposition in the $\pi\pi^*$ state.

CHAPTER 6

Summary and outlook

In this thesis, we have discussed that how OCT can be implemented to manipulate the chemical dynamics. The continuous laser pulse are employed as the external controller. In all these works the ultimate goal is to obtain an optimal laser pulse which will give us the maximum outcome at the end of chemical dynamics. In OCT, the formulation of a laser field dependent cost functional is the center of attraction. The cost functional is mainly comprised of three major parts, the target part, the fluence of laser, and the dynamical constraint. The target part is mainly dissociation flux through an analysis line placed at a certain distance along the reaction coordinate, the projection operator or both of them. The fluence of laser part is added to the cost functional to assure that the optimization of cost functional leads to a reasonable laser pulse shape which will not promote unnecessary processes, like ionization. The TDSE is employed as the dynamical constraint which is attached with the cost functional through a time dependent Lagrange multiplier. The optimization of cost functional is performed using GA.

This thesis reports mainly the quantum control calculations for the photodissociation of two molecules, N-H photodissociation of pyridinyl radical and methyl photodissociation of thioanisole. Pyridinyl radical is a radical which appears as a intermediate for pyridine

catalyzed water splitting reaction in presence of UV light. In this this reaction N-H photodissociation is an important step where pyridinyl absorbs light in the visible region of light. Moreover, pyridinyl can act as a reducible agent for CO_2 in presence of light. On the other hand, thioanisole is an important precursor molecule for drug development and it is one of the most studied sulphur containing model system.

To account the N-H photodissociation of pyridinyl a three state and three mode model Hamiltonian has been employed. The OCT calculation of N-H photodissociation has been performed for different initial vibrationally excited WPs to get an insight of the dissociation mechanism. For all the initial conditions, the N-H photodissociation occurs via $\pi\sigma^*$ state and yields are more than 95% with all these initial conditions for pulse durations 726 fs and 967.55 fs. There is no dependence of the the yields on the initial conditions has been found for these two long pulse durations, but for 250 fs pulse there is an explicit dependence on the initial conditions. One interesting fact is that initial excitation of out-of-plane bending mode of H-atom hinders the dissociation of N-H bond, therefore excitation of the same leads to lowest dissociation yield for 250 fs pulse and dissociation starts little late ($\sim$ 10-12 fs) with 726 fs and 967.55 fs pulses.

Similarly, for the methyl photodissociations of thioanisole a three state and two mode model Hamiltonian has been considered. To make the KE operator simple the methyl group has been considered as a composite particle where the total mass of the methyl group is considered to be embedded at its center-of-mass. To get a preliminary details of the dissociation mechanism the quantum dynamics for delta excitation to the $\pi\pi^*$ state and continuous excitation by an optimal laser pulse of duration 4000 a.u. are compared. It has been observed that methyl photodissociation can follow two paths, either adiabatic path where molecule dissociates along S-C stretching coordinate loosing planarity, or nonadiabatic path where keeping the planarity. In presence of optimal pulse it prefers the nonadiabatic path and in field-free case it follows the adiabatic path.

The quantum control of N-H photodissociation process is further extended with a

different target than the previous work, where suppression of the N-H photodissociation is the goal of the OCT work. In other words, maximization of the lifetime of the $\pi\pi^*$ state is the objective. In this work frequency chirping in the laser pulse has been included. In the GA optimization four parameters of the gaussian shaped laser pulse, like central frequency, width of the pulse, chirping rate, and amplitude are tuned to get a suitable pulse which will lead to the maximum $\pi\pi^*$ state lifetime. To reach the goal, two simultaneous objectives are included in the cost functional. They are the overlap integral of the $\pi\pi^*$ WP component with the ground vibrational eigen function of $\pi\pi^*$ state and other one is the inverse of flux through the asymptotes to suppress the dissociation yield. The optimal laser pulse obtained from the GA optimization is negatively chirped pulse. In presence of negative chirped pulse a coherent WP is formed in the FC region of the $\pi\pi^*$ state and it remains there for a longer time compared to the $\pi\pi^*$ WP component formed due to the monochromatic laser pulse. Moreover, the dissociation yield at the $\pi\sigma^*$ asymptote is effectively suppressed by the frequency chirping effect incorporated in the pulse.

All the laser pulses calculated by GA based optimal control scheme are experimentally feasible. The optimal pulse shapes and the associated frequencies are quite reasonable. In the first two works, the designed optimal pulses are monochromatic in nature and the frequencies are within the visible and UV ranges. On the other hand, in the third work linearly chirped laser pulse is implemented and the pulse scans a broad rang of frequency, from near IR to visible regime, with time. As the optimal pulse is negatively chirped pulse, it starts with higher frequency and proceeds towards lower frequency range with time. The amplitudes of all the laser pulses are in the order of $\sim$0.01 a.u. which falls in the regime where the probability of multi-photon ionization process is considerably less but tunneling ionization may take place. To the best of our understanding, these laser pulses are experimentally feasible given the present state of technology.

Outlook:

(1) The two dimensional model Hamiltonian considered for the methyl dissociation has a major demerit that it did not predict the lifetime of the $\pi\pi^*$ state. Therefore, this problem can be revisited with a model Hamiltonian incorporating few more modes to improve the lifetime of the $\pi\pi^*$ state to better align with the experimental results. A quantum control calculation with the higher dimensional Hamiltonian can also be performed using OCT-MCTDH.

(2) Similarly, to understand mechanism of the N-H photodissociation of pyridinyl radical in more details few more coupling coordinates can be included in the model Hamiltonian.

(3) In this thesis all the quantum control calculation has been performed for only photodissociation processes. So, this work can also be extended for reactive scattering problems. Using pump-probe scheme the final vibrational or rotational state distribution of products can be controlled in the case state-to-state dynamics of triatomic systems.

(4) Molecular orientation prior to collision significantly influences reactive scattering in the ultra-cold regime. Therefore, controlling the orientation (or rotational state) of the molecule (if it has permanent dipole moment) can lead to some interesting results. The quantum control scheme presented in the present thesis can be implemented to design an optimal pulse in the micro-wave region which can control the orientation of the molecule.

(5) One of the unique capabilities of chirped laser pulses is their ability to mitigate quantum state dephasing and also it can create "reflectron" state where molecule move towards the FC region from the dissociation state. Hence, with the aid of chirped laser pulse and the quantum control schemes a scattering state can be transformed into a bound state. In other words, molecular association can achieved using chirped laser pulse.

Appendices

APPENDIX A

Derivation of adiabatic TISE

The adiabatic molecular energy within BO approximation is expressed as [see Eq. 2.14]

$$\langle \psi_{\beta}^{BO} \chi_{\beta j}^{BO} | H_e + T_n + V_{nn} | \psi_{\alpha}^{BO} \chi_{\alpha k}^{BO} \rangle = E_{\alpha k}^{BO} \delta_{\alpha\beta} \delta_{jk}. \tag{A.1}$$

The kinetic energy operator

$$T_n = \sum_i \frac{-\hbar^2}{2M_i} \nabla_{n,i}^2. \tag{A.2}$$

Implementing the kinetic energy operator into Eq. A.3

$$\begin{aligned} &\langle \psi_{\beta}^{BO} \chi_{\beta j}^{BO} | H_e + \sum_i \frac{-\hbar^2}{2M_i} \nabla_{n,i}^2 + V_{nn} | \psi_{\alpha}^{BO} \chi_{\alpha k}^{BO} \rangle = E_{\alpha k}^{BO} \delta_{\alpha\beta} \delta_{jk} \\ i.e. &\langle \psi_{\beta}^{BO} \chi_{\beta j}^{BO} | H_e + V_{nn} | \psi_{\alpha}^{BO} \chi_{\alpha k}^{BO} \rangle + \langle \psi_{\beta}^{BO} \chi_{\beta j}^{BO} | \sum_i \frac{-\hbar^2}{2M_i} \nabla_{n,i}^2 | \psi_{\alpha}^{BO} \chi_{\alpha k}^{BO} \rangle = E_{\alpha k}^{BO} \delta_{\alpha\beta} \delta_{jk} \end{aligned} \tag{A.3}$$

The second term of the L.H.S can be rewritten as

$$
\begin{aligned}
&\langle\psi_\beta^{BO}\chi_{\beta j}^{BO}|\sum_i \frac{-\hbar^2}{2M_i}\vec{\nabla}_{n,i}\cdot\vec{\nabla}_{n,i}|\psi_\alpha^{BO}\chi_{\alpha k}^{BO}\rangle \\
=&\langle\psi_\beta^{BO}\chi_{\beta j}^{BO}|\sum_i \frac{-\hbar^2}{2M_i}\vec{\nabla}_{n,i}\cdot\left((\vec{\nabla}_{n,i}|\psi_\alpha^{BO}\rangle)|\chi_{\alpha k}^{BO}\rangle+|\psi_\alpha^{BO}\rangle(\vec{\nabla}_{n,i}|\chi_{\alpha k}^{BO}\rangle)\right) \\
=&\langle\psi_\beta^{BO}\chi_{\beta j}^{BO}|\sum_i \frac{-\hbar^2}{2M_i}\Bigg(|\psi_\alpha^{BO}\rangle\nabla_{n,i}^2|\chi_{\alpha k}^{BO}\rangle+\vec{\nabla}_{n,i}|\psi_\alpha^{BO}\rangle\cdot\vec{\nabla}_{n,i}|\chi_{\alpha k}^{BO}\rangle \\
&+\vec{\nabla}_{n,i}|\psi_\alpha^{BO}\rangle\cdot\vec{\nabla}_{n,i}|\chi_{\alpha k}^{BO}\rangle+\nabla_{n,i}^2|\psi_\alpha^{BO}\chi_{\alpha k}^{BO}\rangle\Bigg) \\
=&\langle\psi_\beta^{BO}\chi_{\beta j}^{BO}|\sum_i \frac{-\hbar^2}{2M_i}\Bigg(|\psi_\alpha^{BO}\rangle\nabla_{n,i}^2|\chi_{\alpha k}^{BO}\rangle+2\nabla_{n,i}|\psi_\alpha^{BO}\rangle\cdot\nabla_{n,i}|\chi_{\alpha k}^{BO}\rangle+\nabla_{n,i}^2|\psi_\alpha^{BO}\chi_{\alpha k}^{BO}\rangle\Bigg).
\end{aligned}
\tag{A.4}
$$

If we replace the second term of L.H.S. of Eq. A.3 then we arrive at the Eq. 2.15.

APPENDIX B

Derivation of the two conditions for ADT matrix

Let us revisit the Eq. 2.19

$$\Big\{U_{\alpha}^{BO} + V_{nn} + T_n - E_{\alpha k}^{BO}\Big\}|\chi_{\alpha k}^{BO}\rangle = -\sum_{\beta}\Big\{\sum_{i}\frac{-\hbar^2}{2M_i}\Big(2d_i^{\beta\alpha}\cdot\nabla_{n,i} + D_i^{\beta\alpha}\Big)\Big\}|\chi_{\beta k}^{BO}\rangle. \tag{B.1}$$

The derivative coupling and scalar coupling terms present in the R.H.S. is expressed as (see Eq. 2.16)

$$\begin{aligned} d_i^{\beta\alpha} &= \langle\psi_{\beta}^{BO}|\nabla_{n,i}|\psi_{\alpha}^{BO}\rangle \\ D_i^{\beta\alpha} &= \langle\psi_{\beta}^{BO}|\nabla_{n,i}^2|\psi_{\alpha}^{BO}\rangle \\ &= \langle\psi_{\beta}^{BO}|\nabla_{n,i}\cdot\nabla_{n,i}|\psi_{\alpha}^{BO}\rangle \end{aligned} \tag{B.2}$$

Now let us consider the gradient of the derivative coupling term i.e.

$$\begin{aligned}
\nabla_{n,i} \cdot d_i^{\beta\alpha} &= \nabla_{n,i} \cdot \langle \psi_\beta^{BO} | \nabla_{n,i} | \psi_\alpha^{BO} \rangle \\
&= \langle \nabla_{n,i} \psi_\beta^{BO} | \nabla_{n,i} | \psi_\alpha^{BO} \rangle + \langle \psi_\beta^{BO} | \nabla_{n,i} \cdot \nabla_{n,i} | \psi_\alpha^{BO} \rangle \\
&\text{As } |\psi_\gamma^{BO}\rangle, \gamma = 0, 1, ..., N, \text{ forms a complete Hilbert space,} \\
&\sum_\gamma |\psi_\gamma^{BO}\rangle\langle\psi_\gamma^{BO}| = 1 \text{ and we can insert this in the first term.} \\
&= \langle \psi_\beta^{BO} | \nabla_{n,i}^\dagger \Big(\sum_\gamma |\psi_\gamma^{BO}\rangle\langle\psi_\gamma^{BO}| \Big) \nabla_{n,i} | \psi_\alpha^{BO} \rangle + \langle \psi_\beta^{BO} | \nabla_{n,i} \cdot \nabla_{n,i} | \psi_\alpha^{BO} \rangle \\
&\text{As } \nabla_{n,i} \text{ is a anti-Hermitian operator } \nabla_{n,i}^\dagger = -\nabla_{n,i} \\
&= -\sum_\gamma \langle \psi_\beta^{BO} | \nabla_{n,i} | \psi_\gamma^{BO} \rangle \cdot \langle \psi_\gamma^{BO} | \nabla_{n,i} | \psi_\alpha^{BO} \rangle + \langle \psi_\beta^{BO} | \nabla_{n,i} \cdot \nabla_{n,i} | \psi_\alpha^{BO} \rangle \\
&= -\sum_\gamma d_i^{\beta\gamma} \cdot d_i^{\beta\gamma} + D_i^{\beta\alpha}
\end{aligned} \tag{B.3}$$

Therefore,

$$D_i^{\beta\alpha} = \sum_\gamma d_i^{\beta\gamma} \cdot d_i^{\gamma\alpha} + \nabla_{n,i} \cdot d_i^{\beta\alpha} \tag{B.4}$$

So, the Eq. B.1 can be rewritten as

$$\begin{aligned}
\Big\{ U_\alpha^{BO} + V_{nn} + T_n - E_{\alpha k}^{BO} \Big\} |\chi_{\alpha k}^{BO}\rangle = -\sum_\beta \Big\{ \sum_i \frac{-\hbar^2}{2M_i} \Big(2 d_i^{\beta\alpha} \cdot \nabla_{n,i} \\
+ \sum_\gamma d_i^{\beta\gamma} \cdot d_i^{\gamma\alpha} + \nabla_{n,i} \cdot d_i^{\beta\alpha} \Big) \Big\} |\chi_{\beta k}^{BO}\rangle.
\end{aligned} \tag{B.5}$$

In the matrix form this equation can be rewritten as

$$\begin{aligned}
&\Big\{ \mathbf{U}^{BO} + V_{nn}\mathbf{I} + \sum_i \frac{-\hbar^2}{2M_i} \Big(\nabla_{n,i}^2 + 2\mathbf{d}_i \cdot \nabla_{n,i} + \mathbf{d}_i \cdot \mathbf{d}_i + \nabla_{n,i} \cdot \mathbf{d}_i \Big) - E_{\alpha k}^{BO} \mathbf{I} \Big\} \boldsymbol{\chi}^{BO} = \mathbf{0} \\
&\Big\{ \mathbf{U}^{BO} + V_{nn}\mathbf{I} + \sum_i \frac{-\hbar^2}{2M_i} \Big(\nabla_{n,i} + \mathbf{d}_i \Big)^2 - E_{\alpha k}^{BO} \mathbf{I} \Big\} \boldsymbol{\chi}^{BO} = \mathbf{0}.
\end{aligned} \tag{B.6}$$

The diabatic and adiabatic electronic wavefunctions are related by the following equation (in matrix formalism)

$$\boldsymbol{\psi}^{DA} = \mathbf{A}\boldsymbol{\psi}^{BO}, \tag{B.7}$$

where $\mathbf{A}$ is the unitary matrix which is known as adiabatic to diabatic transformation (ADT) matrix and its elements are $a_{\alpha\beta}$. On the other hand, the nuclear wave function transforms as

$$\boldsymbol{\chi}^{DA} = \mathbf{A}^{\dagger}\boldsymbol{\chi}^{BO} \tag{B.8}$$

Now if we replace this $\boldsymbol{\chi}^{BO}$ into Eq. B.14 we get

$$\Big\{\mathbf{U}^{BO} + V_{nn}\mathbf{I} + \sum_i \frac{-\hbar^2}{2M_i}\Big(\nabla_{n,i} + \mathbf{d}_i\Big)^2 - E^{BO}_{\alpha k}\mathbf{I}\Big\}\mathbf{A}\boldsymbol{\chi}^{DA} = \mathbf{0}. \tag{B.9}$$

Let us solve first the third term

$$\begin{aligned}
&\sum_i \frac{-\hbar^2}{2M_i}\Big(\nabla_{n,i} + \mathbf{d}_i\Big)^2\mathbf{A}\boldsymbol{\chi}^{DA} \\
&= \sum_i \frac{-\hbar^2}{2M_i}\Big(\nabla_{n,i} + \mathbf{d}_i\Big)\cdot\Big(\nabla_{n,i} + \mathbf{d}_i\Big)\mathbf{A}\boldsymbol{\chi}^{DA} \\
&= \sum_i \frac{-\hbar^2}{2M_i}\Big(\nabla_{n,i} + \mathbf{d}_i\Big)\cdot\Big(\mathbf{A}\nabla_{n,i}\boldsymbol{\chi}^{DA} + (\nabla_{n,i}\mathbf{A})\boldsymbol{\chi}^{DA} + \mathbf{d}_i\mathbf{A}\boldsymbol{\chi}^{DA}\Big) \\
&= \sum_i \frac{-\hbar^2}{2M_i}\Big\{2(\nabla_{n,i}\mathbf{A})\cdot\nabla_{n,i}\boldsymbol{\chi}^{DA} + \mathbf{A}\nabla^2_{n,i}\boldsymbol{\chi}^{DA} + (\nabla^2_{n,i}\mathbf{A})\boldsymbol{\chi}^{DA} \\
&+ (\nabla_{n,i}\mathbf{d}_i)\mathbf{A}\boldsymbol{\chi}^{DA} + 2\mathbf{d}_i(\nabla_{n,i}\mathbf{A})\boldsymbol{\chi}^{DA} + 2\mathbf{d}_i\mathbf{A}(\nabla_{n,i}\boldsymbol{\chi}^{DA}) + \mathbf{d}_i^2\mathbf{A}\boldsymbol{\chi}^{DA}\Big\}
\end{aligned} \tag{B.10}$$

after rearranging the terms

$$\sum_i \frac{-\hbar^2}{2M_i}\Big\{\mathbf{A}\nabla^2_{n,i}\boldsymbol{\chi}^{DA} + 2(\nabla_{n,i}\mathbf{A} + \mathbf{d}_i\mathbf{A})\cdot\nabla_{n,i}\boldsymbol{\chi}^{DA} + \Big\{(\mathbf{d}_i + \nabla_{n,i})\cdot(\nabla_{n,i}\mathbf{A} + \mathbf{d}_i\mathbf{A})\Big\}\boldsymbol{\chi}^{DA}\Big\} \tag{B.11}$$

Now if the transformation matrix $\mathbf{A}$ satisfies the following

$$\nabla_{n,i}\mathbf{A} + \mathbf{d}_i\mathbf{A} = \mathbf{0}, \text{for all i,} \tag{B.12}$$

then

$$\sum_i \frac{-\hbar^2}{2M_i}\Big(\nabla_{n,i} + \mathbf{d}_i\Big)^2\mathbf{A}\boldsymbol{\chi}^{DA} = \sum_i \frac{-\hbar^2}{2M_i}\mathbf{A}\nabla^2_{n,i}\boldsymbol{\chi}^{DA} \tag{B.13}$$

Substituting Eq. B.13 into Eq. B.14

$$\sum_i \frac{-\hbar^2}{2M_i}\mathbf{A}\nabla^2_{n,i}\boldsymbol{\chi}^{DA} + \Big\{\mathbf{U}^{BO} + V_{nn}\mathbf{I} - E^{BO}\mathbf{I}\Big\}\mathbf{A}\boldsymbol{\chi}^{DA} = \mathbf{0}. \tag{B.14}$$

Multiplying Eq. B.14 by $\mathbf{A}^\dagger$

$$\sum_i \frac{-\hbar^2}{2M_i}\nabla^2_{n,i}\boldsymbol{\chi}^{DA} + \Big\{\mathbf{U}^{DA} - E^{BO}\mathbf{I}\Big\}\boldsymbol{\chi}^{DA} = \mathbf{0}. \tag{B.15}$$

where $\mathbf{U}^{DA}$ is defined by $\mathbf{U}^{DA} = \mathbf{A}^\dagger\mathbf{U}^{BO}\mathbf{A} + V_{nn}\mathbf{I}$ and it is the potential energy in diabatic representation. The transformation matrix $\mathbf{A}$ is calculated by condition defined in Eq. B.12.

APPENDIX C

Analytical formulation of the wave packet dynamics on the three states

Within the first order perturbation theory we have

$$\boldsymbol{\psi}(t) = -\frac{i}{\hbar}\int_0^t e^{-\frac{i}{\hbar}\mathbf{H}_0' t}\mathbf{V}_I e^{-\frac{i}{\hbar}\mathbf{H}_0' t}\boldsymbol{\psi}(0)dt \tag{C.1}$$

where $\mathbf{H}_0'$ and $\mathbf{V}_I$ are defined as[92, 160]

$$\mathbf{H}_0' = \begin{pmatrix} \hat{T}_N + V_{00} & 0 & 0 \\ 0 & \hat{T}_N + V_{11} & 0 \\ 0 & 0 & \hat{T}_N + V_{22} \end{pmatrix} = \begin{pmatrix} H_{00} & 0 & 0 \\ 0 & H_{11} & 0 \\ 0 & 0 & H_{22} \end{pmatrix} \tag{C.2}$$

and

$$\mathbf{V}_I = \begin{pmatrix} 0 & -\mu_{01}E & V_{02} \\ -\mu_{01}E & 0 & V_{12} \\ V_{02} & V_{12} & 0 \end{pmatrix}, \tag{C.3}$$

respectively. Since the unperturbed Hamiltonian, $\mathbf{H}_0'$, is a diagonal matrix, the exponential term in Eq. C.1 boils down into

$$e^{-\frac{i}{\hbar}\mathbf{H}_0' t} = \begin{pmatrix} e^{-\frac{i}{\hbar}H_{00}t} & 0 & 0 \\ 0 & e^{-\frac{i}{\hbar}H_{11}t} & 0 \\ 0 & 0 & e^{-\frac{i}{\hbar}H_{22}t} \end{pmatrix}. \tag{C.4}$$

Now the Eq. C.1 can be rewritten in matrix form as

$$\begin{pmatrix} \psi_0(t) \\ \psi_1(t) \\ \psi_2(t) \end{pmatrix} = \begin{pmatrix} -\frac{i}{\hbar}\int_0^t e^{-\frac{i}{\hbar}H_{00}t}(-\mu_{01}E)e^{-\frac{i}{\hbar}H_{11}t}\psi_1(0)dt - \frac{i}{\hbar}\int_0^t e^{-\frac{i}{\hbar}H_{00}t}V_{02}e^{-\frac{i}{\hbar}H_{22}t}\psi_2(0)dt \\ -\frac{i}{\hbar}\int_0^t e^{-\frac{i}{\hbar}H_{11}t}(-\mu_{01}E)e^{-\frac{i}{\hbar}H_{00}t}\psi_0(0)dt - \frac{i}{\hbar}\int_0^t e^{-\frac{i}{\hbar}H_{11}t}V_{12}e^{-\frac{i}{\hbar}H_{22}t}\psi_2(0)dt \\ -\frac{i}{\hbar}\int_0^t e^{-\frac{i}{\hbar}H_{22}t}V_{02}e^{-\frac{i}{\hbar}H_{00}t}\psi_0(0)dt - \frac{i}{\hbar}\int_0^t e^{-\frac{i}{\hbar}H_{22}t}V_{12}e^{-\frac{i}{\hbar}H_{11}t}\psi_1(0)dt \end{pmatrix}. \tag{C.5}$$

So the Eq. C.5 leads to three coupled equations which corresponds to the dynamics on the three electronic states under the influence of optimal laser pulse,

$$\begin{aligned} \psi_0(t) =& -\frac{i}{\hbar}\int_0^t e^{-\frac{i}{\hbar}H_{00}t}(-\mu_{01}E)e^{-\frac{i}{\hbar}H_{11}t}\psi_1(0)dt \\ & -\frac{i}{\hbar}\int_0^t e^{-\frac{i}{\hbar}H_{00}t}V_{02}e^{-\frac{i}{\hbar}H_{22}t}\psi_2(0)dt \\ \psi_1(t) =& -\frac{i}{\hbar}\int_0^t e^{-\frac{i}{\hbar}H_{11}t}(-\mu_{01}E)e^{-\frac{i}{\hbar}H_{00}t}\psi_0(0)dt \\ & -\frac{i}{\hbar}\int_0^t e^{-\frac{i}{\hbar}H_{11}t}V_{12}e^{-\frac{i}{\hbar}H_{22}t}\psi_2(0)dt \\ \psi_2(t) =& -\frac{i}{\hbar}\int_0^t e^{-\frac{i}{\hbar}H_{22}t}V_{02}e^{-\frac{i}{\hbar}H_{00}t}\psi_0(0)dt \\ & -\frac{i}{\hbar}\int_0^t e^{-\frac{i}{\hbar}H_{22}t}V_{12}e^{-\frac{i}{\hbar}H_{11}t}\psi_1(0)dt \end{aligned} \tag{C.6}$$

APPENDIX D

Pseudospectral method

The spectral quantization technique is employed for the calculation of vibrational energy eigenvalues and the corresponding eigenfunctions of an electronic state.[130] An initial gaussian wave packet is propagated for a certain amount of time on a PES. To obtain the eigenvalue spectrum, the time dependent autocorrelation function $C(t)$ is calculated at each time steps which is then Fourier transformed to generate the spectrum

$$I(E) = \int_0^\infty C(t) e^{iEt}\, dt. \tag{D.1}$$

The vibrational eigenfunctions of those corresponding eigenenergies are given by

$$\Psi_n(E) = \int_0^\infty \Psi(t) e^{iE_n t}\, dt. \tag{D.2}$$

No damping function is implemented in the calculation. For instance, a two dimensional initial guess wave packet considered is defined as

$$\Psi(t=0) = N \times \exp\left(-\frac{(R-R_0)^2}{2\sigma_R^2})\right) \times \exp\left(-\frac{(\phi-\phi_0)}{2\sigma_\phi^2}\right), \tag{D.3}$$

where N is an normalization constant. The positions of the center of the gaussian function along the two coordinates are chosen such that the guess wave packet is initially shifted ($r_0 = 4.0$ a.u. and $\theta_0 = 0.2$ rad.) from the equilibrium position of ground state. The full width at half maximum are is chosen at $\sigma_R = 0.3$ a.u. and $\sigma_\phi = 0.15$ a.u.

APPENDIX E

Supplementary material for Chapter 4

This supplementary material provides the dissociation yields through the three channels (Fig. E.1) with respect to time on the three coupled potential energy surfaces for different initial vibrational states when they are vertically excited to the $\pi\pi^*$ state. The Fig. (E.2) represents the results for the OCT calculation with the initial condition, $n_R = 3$. The Fig. (E.3) represents the potential energy surface in adiabatic representation.

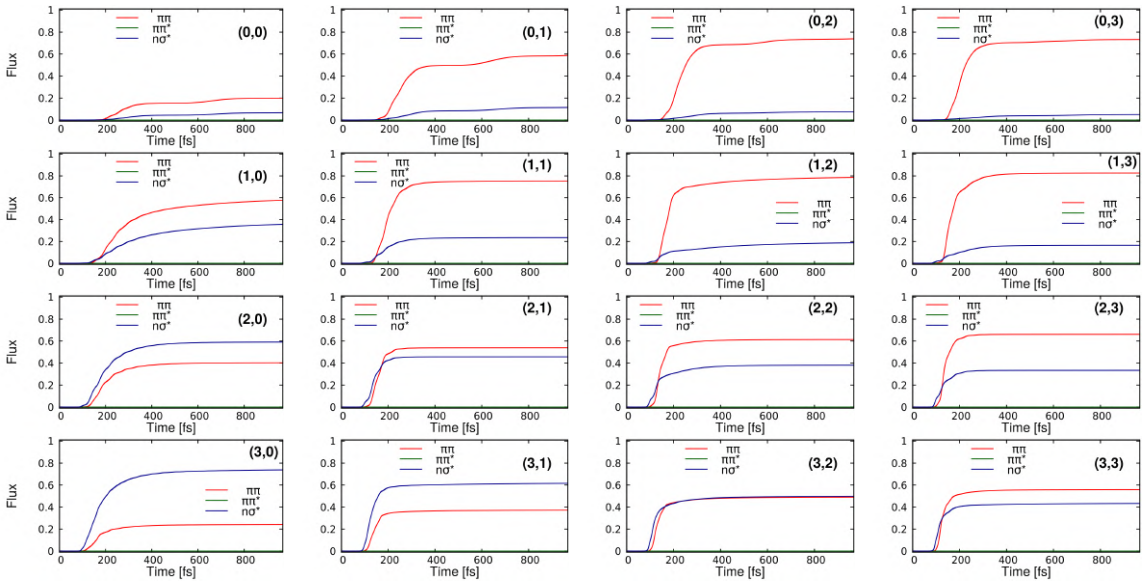

Figure E.1: Dissociation yields through three asymptotes for different initial vibrational state after the vertical transition to the $\pi\pi^*$ state in absence of laser pulse.

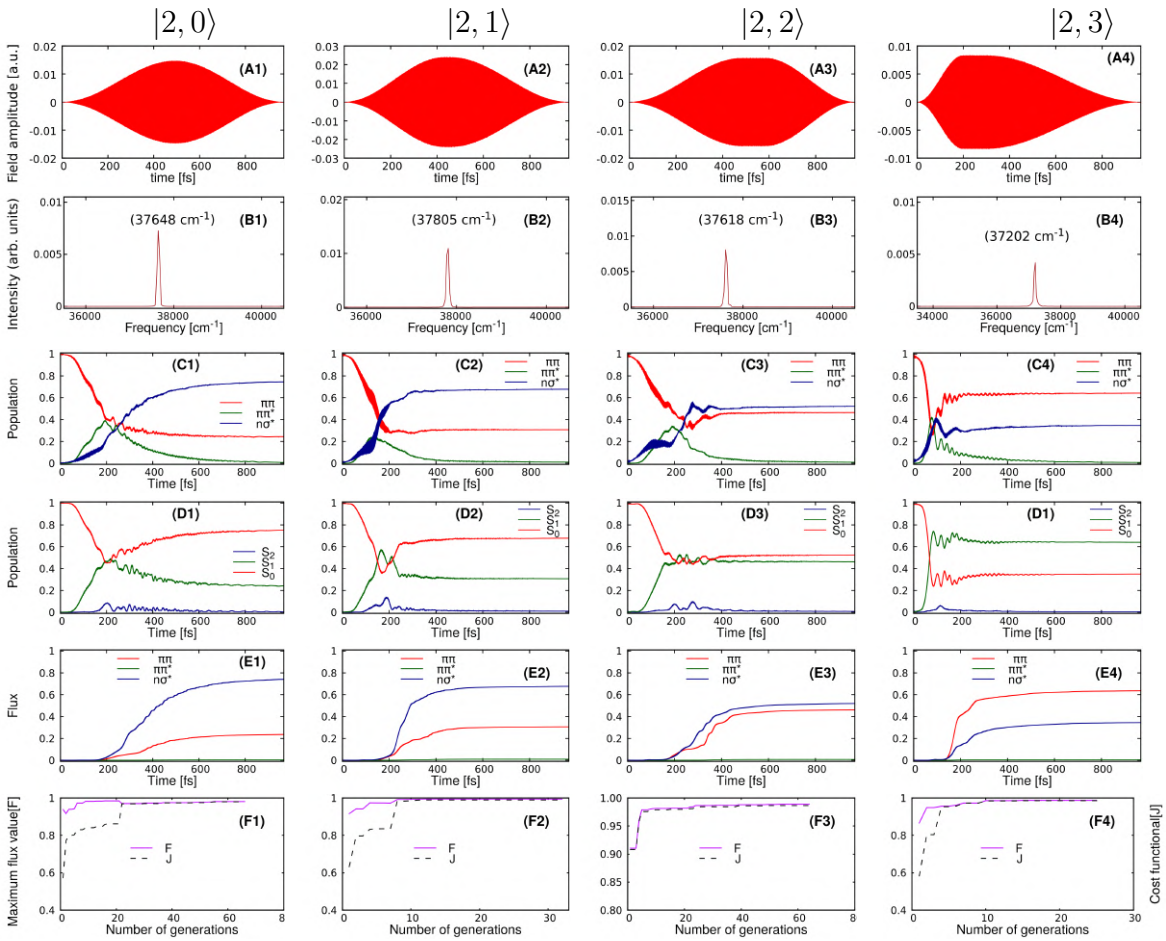

Figure E.2: Results of OCT calculations using (2,0), (2,1), (2,2) and (2,3) initial conditions. The temporal profile of optimal pulse (panels (A1,A2,A3,A4)), the frequency spectrum of these pulses (panels (B1,B2,B3,B4)), diabatic population dynamics (panels (C1,C2,C3,C4)), adiabatic population dynamics (panels (D1,D2,D3,D4)), time-integrated flux with respect to time (panels (E1,E2,E3,E4)), and values of cost functional [J], in addition, the total dissociative flux [F] at each generation (panels (F1,F2,F3,F4)) are depicted.

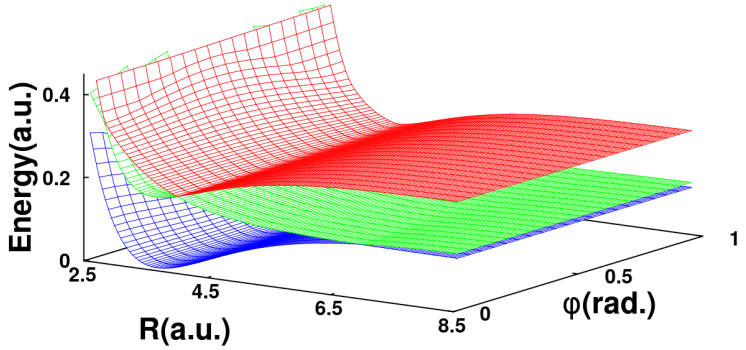

Figure E.3: Adiabatic potential energy surfaces in (R,ϕ) space. They are designated as S_0(blue), S_1(green), S_2(red).

REFERENCES

[1] R. L. Vander Wal, J. Scott, and F. Crim, "Selectively breaking the O-H bond in HOD," *J. chem. phys.*, vol. 92, no. 1, pp. 803–805, 1990.

[2] A. Sinha, M. C. Hsiao, and F. F. Crim, "Bond-selected bimolecular chemistry: H + HOD(4νOH) $\rightarrow$ OD + H_2," *J. chem. phys.*, vol. 92, no. 10, pp. 6333–6335, 1990.

[3] N. Bloembergen and A. H. Zewail, "Energy redistribution in isolated molecules and the question of mode-selective laser chemistry revisited," *J. Phys. Chem.*, vol. 88, no. 23, pp. 5459–5465, 1984.

[4] T. Elsaesser and W. Kaiser, "Vibrational and vibronic relaxation of large polyatomic molecules in liquids," *Ann. rev. phys. chem.*, vol. 42, no. 1, pp. 83–107, 1991.

[5] A. H. Zewail, "Femtochemistry: recent progress in studies of dynamics and control of reactions and their transition states," *J. Phys. Chem.*, vol. 100, no. 31, pp. 12701–12724, 1996.

[6] M. Gruebele and R. Bigwood, "Molecular vibrational energy flow: beyond the golden rule," *Int. Rev. Phys. Chem.*, vol. 17, no. 2, pp. 91–145, 1998.

[7] W. S. Warren, H. Rabitz, and M. Dahleh, "Coherent control of quantum dynamics: the dream is alive," *Science*, vol. 259, no. 5101, pp. 1581–1589, 1993.

[8] A. M. Weiner, D. E. Leaird, J. S. Patel, and J. R. Wullert, "Programmable femtosecond pulse shaping by use of a multielement liquid-crystal phase modulator," *Opt. lett.*, vol. 15, no. 6, pp. 326–328, 1990.

[9] A. M. Weiner, D. E. Leaird, J. Patel, and J. R. Wullert, "Programmable shaping of femtosecond optical pulses by use of 128-element liquid crystal phase modulator," *IEEE j. quant. elec.*, vol. 28, no. 4, pp. 908–920, 1992.

[10] P. Brumer and M. Shapiro, "Control of unimolecular reactions using coherent light," *Chem. Phys. Lett.*, vol. 126, no. 6, pp. 541–546, 1986.

[11] M. Shapiro, J. W. Hepburn, and P. Brumer, "Simplified laser control of unimolecular reactions: Simultaneous (ω1, ω3) excitation," *Chem. Phys. Lett.*, vol. 149, no. 5-6, pp. 451–454, 1988.

[12] P. Brumer and M. Shapiro, "One photon mode selective control of reactions by rapid or shaped laser pulses: An emperor without clothes?," *Chem. phys.*, vol. 139, no. 1, pp. 221–228, 1989.

[13] C. Chen, Y.-Y. Yin, and D. Elliott, "Interference between optical transitions," *Phys. rev. lett.*, vol. 64, no. 5, p. 507, 1990.

[14] S. M. Park, S.-P. Lu, and R. J. Gordon, "Coherent laser control of the resonance-enhanced multiphoton ionization of HCL," *J. chem. phys.*, vol. 94, no. 12, pp. 8622–8624, 1991.

[15] D. J. Tannor and S. A. Rice, "Control of selectivity of chemical reaction via control of wave packet evolution," *J. chem. phys.*, vol. 83, no. 10, pp. 5013–5018, 1985.

[16] D. J. Tannor, R. Kosloff, and S. A. Rice, "Coherent pulse sequence induced control of selectivity of reactions: Exact quantum mechanical calculations," *J. Chem. Phys.*, vol. 85, no. 10, pp. 5805–5820, 1986.

[17] T. Baumert, M. Grosser, R. Thalweiser, and G. Gerber, "Femtosecond time-resolved molecular multiphoton ionization: The Na_2 system," *Phys. rev. lett.*, vol. 67, no. 27, p. 3753, 1991.

[18] E. Potter, J. Herek, S. Pedersen, Q. Liu, and A. Zewail, "Femtosecond laser control of a chemical reaction," *Nature*, vol. 355, no. 6355, pp. 66–68, 1992.

[19] T. Baumert and G. Gerber, "Fundamental interactions of molecules (Na_2, Na_3) with intense femtosecond laser pulses," *Isra. j. chem.*, vol. 34, no. 1, pp. 103–114, 1994.

[20] J. Herek, A. Materny, and A. Zewail, "Femtosecond control of an elementary unimolecular reaction from the transition-state region," *Chem. phys. lett.*, vol. 228, no. 1-3, pp. 15–25, 1994.

[21] S. Shi, A. Woody, and H. Rabitz, "Optimal control of selective vibrational excitation in harmonic linear chain molecules," *J. Chem. Phys.*, vol. 88, no. 11, pp. 6870–6883, 1988.

[22] A. P. Peirce, M. A. Dahleh, and H. Rabitz, "Optimal control of quantum-mechanical systems: Existence, numerical approximation, and applications," *Phys. Rev. A*, vol. 37, no. 12, p. 4950, 1988.

[23] R. Kosloff, S. A. Rice, P. Gaspard, S. Tersigni, and D. J. Tannor, "Wavepacket dancing: Achieving chemical selectivity by shaping light pulses," *Chem. Phys.*, vol. 139, no. 1, pp. 201–220, 1989.

[24] W. Jakubetz, J. Manz, and H.-J. Schreier, "Theory of optimal laser pulses for selective transitions between molecular eigenstates," *Chem. phys. lett.*, vol. 165, no. 1, pp. 100–106, 1990.

[25] R. J. Levis, G. M. Menkir, and H. Rabitz, "Selective bond dissociation and rearrangement with optimally tailored, strong-field laser pulses," *Science*, vol. 292, no. 5517, pp. 709–713, 2001.

[26] R. Levis and H. Rabitz, "Closing the loop on bond selective chemistry using tailored strong field laser pulses," *J. Phys. Chem. A*, vol. 106, no. 27, pp. 6427–6444, 2002.

[27] A. Assion, T. Baumert, M. Bergt, T. Brixner, B. Kiefer, V. Seyfried, M. Strehle, and G. Gerber, "Control of chemical reactions by feedback-optimized phase-shaped femtosecond laser pulses," *Science*, vol. 282, no. 5390, pp. 919–922, 1998.

[28] Š. Vajda, A. Bartelt, E.-C. Kaposta, T. Leisner, C. Lupulescu, S. Minemoto, P. Rosendo-Francisco, and L. Wöste, "Feedback optimization of shaped femtosecond laser pulses for controlling the wavepacket dynamics and reactivity of mixed alkaline clusters," *Chem. Phys.*, vol. 267, no. 1-3, pp. 231–239, 2001.

[29] R. Bartels, S. Backus, E. Zeek, L. Misoguti, G. Vdovin, I. Christov, M. Murnane, and H. Kapteyn, "Shaped-pulse optimization of coherent emission of high-harmonic soft X-rays," *Nature*, vol. 406, no. 6792, pp. 164–166, 2000.

[30] J. Kunde, B. Baumann, S. Arlt, F. Morier-Genoud, U. Siegner, and U. Keller, "Adaptive feedback control of ultrafast semiconductor nonlinearities," *App. Phys. Lett.*, vol. 77, no. 7, pp. 924–926, 2000.

[31] T. Weinacht, J. Ahn, and P. H. Bucksbaum, "Controlling the shape of a quantum wavefunction," *Nature*, vol. 397, no. 6716, pp. 233–235, 1999.

[32] F. G. Omenetto, A. J. Taylor, M. D. Moores, and D. H. Reitze, "Adaptive control of femtosecond pulse propagation in optical fibers," *Opt. Lett.*, vol. 26, no. 12, pp. 938–940, 2001.

[33] D. Zeidler, S. Frey, W. Wohlleben, M. Motzkus, F. Busch, T. Chen, W. Kiefer, and A. Materny, "Optimal control of ground-state dynamics in polymers," *J. chem. phys.*, vol. 116, no. 12, pp. 5231–5235, 2002.

[34] J. L. Herek, W. Wohlleben, R. J. Cogdell, D. Zeidler, and M. Motzkus, "Quantum control of energy flow in light harvesting," *Nature*, vol. 417, no. 6888, pp. 533–535, 2002.

[35] C. J. Bardeen, V. V. Yakovlev, K. R. Wilson, S. D. Carpenter, P. M. Weber, and W. S. Warren, "Feedback quantum control of molecular electronic population transfer," *Chem. Phys. Lett.*, vol. 280, no. 1-2, pp. 151–158, 1997.

[36] T. Brixner, N. Damrauer, P. Niklaus, and G. Gerber, "Photoselective adaptive femtosecond quantum control in the liquid phase," *Nature*, vol. 414, no. 6859, pp. 57–60, 2001.

[37] B. Li, G. Turinici, V. Ramakrishna, and H. Rabitz, "Optimal dynamic discrimination of similar molecules through quantum learning control," *J. Phys. Chem. B*, vol. 106, no. 33, pp. 8125–8131, 2002.

[38] R. S. Judson and H. Rabitz, "Teaching lasers to control molecules," *Phys. Rev. Lett.*, vol. 68, no. 10, p. 1500, 1992.

[39] P. Gross, D. Neuhauser, and H. Rabitz, "Teaching lasers to control molecules in the presence of laboratory field uncertainty and measurement imprecision," *J. chem. phys.*, vol. 98, no. 6, pp. 4557–4566, 1993.

[40] J. Savolainen, "Coherent control of biomolecules," 2008.

[41] D. Yang, J. Savolainen, A. Jafarpour, D. Sprünken, and J. L. Herek, "A new paradigm for photodynamic therapy: coherent control," in *Photodynamic Therapy: Back to the Future*, vol. 7380, pp. 984–992, SPIE, 2009.

[42] D. Zeidler, S. Frey, K.-L. Kompa, and M. Motzkus, "Evolutionary algorithms and their application to optimal control studies," *Phys. Rev. A*, vol. 64, no. 2, p. 023420, 2001.

[43] B. Pearson, J. White, T. Weinacht, and P. Bucksbaum, "Coherent control using adaptive learning algorithms," *Phys. Rev. A*, vol. 63, no. 6, p. 063412, 2001.

[44] H. Rabitz, "The role of theory in the laboratory control of quantum dynamics phenomena," *Theo. Chem. Acc.*, vol. 109, no. 2, pp. 64–70, 2003.

[45] S. Golden, "Minimal adiabatic approximation of molecular energies," *Mol. Phys.*, vol. 93, no. 3, pp. 421–430, 1998.

[46] M. Born and R. Oppenheimer, "Zur quantentheorie der molekeln," *Ann. der Physik*, vol. 389 (20), pp. 457–484, 1927.

[47] J. C. Tully, "Perspective on "zur quantentheorie der molekeln" born m, oppenheimer r (1927) ann phys 84: 457," *Theo. Chem. Acc.*, vol. 103, pp. 173–176, 2000.

[48] H. J. Monkhorst, "Chemical physics without the born-oppenheimer approximation: The molecular coupled-cluster method," *Phys. Rev. A*, vol. 36, no. 4, p. 1544, 1987.

[49] S. L. Mielke, D. W. Schwenke, G. C. Schatz, B. C. Garrett, and K. A. Peterson, "Functional representation for the born-oppenheimer diagonal correction and born-huang adiabatic potential energy surfaces for isotopomers of H_3," *J. Phys. Chem. A*, vol. 113, no. 16, pp. 4479–4488, 2009.

[50] M. P. Bircher, E. Liberatore, N. J. Browning, S. Brickel, C. Hofmann, A. Patoz, O. T. Unke, T. Zimmermann, M. Chergui, P. Hamm, *et al.*, "Nonadiabatic effects in electronic and nuclear dynamics," *Struct. Dyn.*, vol. 4, no. 6, 2017.

[51] A. Davydov and D. Haar, *Quantum Mechanics: International Series in Natural Philosophy*. International series in natural philosophy, Pergamon, 2013.

[52] M. Baer, "Electronic non-adiabatic transitions derivation of the general adiabatic-diabatic transformation matrix," *Mol. Phys.*, vol. 40, no. 4, pp. 1011–1013, 1980.

[53] M. Baer, "The electronic non-adiabatic coupling term in molecular systems: A theoretical approach," *The Role of Degenerate States in Chemistry*, vol. 124, pp. 39–142, 2002.

[54] C. A. Mead and D. G. Truhlar, "Conditions for the definition of a strictly diabatic electronic basis for molecular systems," *J. Chem. Phys.*, vol. 77, no. 12, pp. 6090–6098, 1982.

[55] W. Domcke and G. Stock, "Theory of ultrafast nonadiabatic excited-state processes and their spectroscopic detection in real time," *Adv. Chem. Phys.*, vol. 100, pp. 1–169, 1997.

[56] W. Domcke, D. Yarkony, and H. Köppel, *Conical intersections: electronic structure, dynamics & spectroscopy*, vol. 15. World Scientific, 2004.

[57] Z. Lan, *Photo-induced Nonadiabatic Dynamics of Aromatic Molecules Via Conical Intersections: Electronic-structure and Time-dependent Quantum Dynamics Calculations*. PhD thesis, Technische Universität München, 2007.

[58] H. Köppel, J. Gronki, and S. Mahapatra, "Construction scheme for regularized diabatic states," *J. Chem. Phys.*, vol. 115, no. 6, pp. 2377–2388, 2001.

[59] H. Nakamura and D. G. Truhlar, "The direct calculation of diabatic states based on configurational uniformity," *J. Chem. Phys.*, vol. 115, no. 22, pp. 10353–10372, 2001.

[60] H. Nakamura and D. G. Truhlar, "Direct diabatization of electronic states by the fourfold way. ii. dynamical correlation and rearrangement processes," *J. Chem. Phys.*, vol. 117, no. 12, pp. 5576–5593, 2002.

[61] H. Nakamura and D. G. Truhlar, "Extension of the fourfold way for calculation of global diabatic potential energy surfaces of complex, multiarrangement, non-born–oppenheimer systems: Application to HNCO (S0,S1)," *J. Chem. Phys.*, vol. 118, no. 15, pp. 6816–6829, 2003.

[62] K. R. Yang, X. Xu, J. Zheng, and D. G. Truhlar, "Full-dimensional potentials and state couplings and multidimensional tunneling calculations for the photodissociation of phenol," *Chem. Sci.*, vol. 5, no. 12, pp. 4661–4680, 2014.

[63] Y. Shu, Z. Varga, S. Kanchanakungwankul, L. Zhang, and D. G. Truhlar, "Diabatic states of molecules," *J. Phys. Chem. A*, vol. 126, no. 7, pp. 992–1018, 2022.

[64] S. L. Li and D. G. Truhlar, "Full-dimensional ground-and excited-state potential energy surfaces and state couplings for photodissociation of thioanisole," *J. Chem. Phys.*, vol. 146, no. 6, p. 064301, 2017.

[65] F. Hund, "Zur deutung der molekelspektren. i," *Zeitschrift für Physik*, vol. 40, no. 10, pp. 742–764, 1927.

[66] E. Wigner and J. Von Neumann, "Uber das verhalten von eigenwerten bei adiabatischen prozessen," *Phys. Zeit*, vol. 30, pp. 467–470, 1929.

[67] E. Teller, "The crossing of potential surfaces.," *J. Phys. Chem.*, vol. 41, no. 1, pp. 109–116, 1937.

[68] G. Herzberg and H. C. Longuet-Higgins, "Intersection of potential energy surfaces in polyatomic molecules," *Discuss. Faraday Soc.*, vol. 35, pp. 77–82, 1963.

[69] H. C. Longuet-Higgins, "The intersection of potential energy surfaces in polyatomic molecules," *Proc. R. Soc. Lond. Ser. A.*, vol. 344, no. 1637, pp. 147–156, 1975.

[70] M. V. Berry, "Quantal phase factors accompanying adiabatic changes," *Proc. R. Soc. A*, vol. 392, no. 1802, pp. 45–57, 1984.

[71] I. G. Ryabinkin, L. Joubert-Doriol, and A. F. Izmaylov, "Geometric phase effects in nonadiabatic dynamics near conical intersections," *Acc. chem. res.*, vol. 50, no. 7, pp. 1785–1793, 2017.

[72] I. G. Ryabinkin and A. F. Izmaylov, "Geometric phase effects in dynamics near conical intersections: Symmetry breaking and spatial localization," *Phys. rev. lett.*, vol. 111, no. 22, p. 220406, 2013.

[73] Z. Lan, W. Domcke, V. Vallet, A. L. Sobolewski, and S. Mahapatra, "Time-dependent quantum wave-packet description of the $\pi^1\sigma^*$ photochemistry of phenol," *J. Chem. Phys.*, vol. 122, no. 22, p. 224315, 2005.

[74] S. Shi and H. Rabitz, "Quantum mechanical optimal control of physical observables in microsystems," *J. Chem. Phys.*, vol. 92, pp. 364–376, 01 1990.

[75] W. Zhu and H. Rabitz, "Uniform, rapidly convergent algorithm for quantum optimal control of objectives with a positive semidefinite hessian matrix," *Phys. Rev. A*, vol. 58, pp. 4741–4748, Dec 1998.

[76] G. G. Balint-Kurti, F. R. Manby, Q. Ren, M. Artamonov, T.-S. Ho, and H. Rabitz, "Quantum control of molecular motion including electronic polarization effects with a two-stage toolkit," *J. chem. phys.*, vol. 122, no. 8, 2005.

[77] G. G. Balint-Kurti, S. Zou, and A. Brown, "Optimal control theory for manipulating molecular processes," *Adv. chem. phys.*, vol. 138, pp. 43–94, 2008.

[78] Q. Ren, G. G. Balint-Kurti, F. R. Manby, M. Artamonov, T.-S. Ho, and H. Rabitz, "Quantum control of molecular vibrational and rotational excitations in a homonuclear diatomic molecule: A full three-dimensional treatment with polarization forces," *J. chem. phys.*, vol. 124, no. 1, 2006.

[79] W. H. Press, B. P. Flannery, S. A. Teukolsky, W. T. Vetterling, *et al.*, "Numerical recipes," 1989.

[80] S. Sharma, H. Singh, and G. G. Balint-Kurti, "Genetic algorithm optimization of laser pulses for molecular quantum state excitation," *J. Chem. Phys.*, vol. 132, no. 6, p. 064108, 2010.

[81] T. Cheng and A. Brown, "Quantum computing based on vibrational eigenstates: Pulse area theorem analysis," *J. chem. phys.*, vol. 124, no. 3, 2006.

[82] R. P. Feynman and A. R. Hibbs, *Quantum Mechanics and Path Integrals*. New York: McGraw-Hill, 1965.

[83] T. Brixner and G. Gerber, "Quantum control of gas-phase and liquid-phase femtochemistry," *ChemPhysChem*, vol. 4, no. 5, pp. 418–438, 2003.

[84] C. Asaro, P. Brumer, and M. Shapiro, "Polarization control of branching ratios in photodissociation," *Phys. Rev. Lett.*, vol. 60, no. 16, p. 1634, 1988.

[85] T. Seideman, M. Shapiro, and P. Brumer, "Coherent radiative control of unimolecular reactions: selective bond breaking with picosecond pulses," *J. Chem. Phys.*, vol. 90, no. 12, pp. 7132–7136, 1989.

[86] A. Serrano-Jiménez, L. Bañares, and A. García-Vela, "Weak-field coherent control of photodissociation in polyatomic molecules," *Phys. Chem. Chem. Phys.*, vol. 21, no. 15, pp. 7885–7893, 2019.

[87] K. Nandipati, A. K. Kanakati, H. Singh, Z. Lan, and S. Mahapatra, "Initial state-specific photodissociation dynamics of pyrrole via $^1\pi\sigma/S_0$ conical intersection initiated with optimally controlled uv-laser pulses," *Eur. Phys. J. D*, vol. 71, pp. 1–9, 2017.

[88] N. Giri and S. Mahapatra, "Optimal control of photodissociation of phenol using genetic algorithm," *J. Chem. Phys.*, vol. 156, no. 9, p. 094305, 2022.

[89] X. Liu, A. L. Sobolewski, R. Borrelli, and W. Domcke, "Computational investigation of the photoinduced homolytic dissociation of water in the pyridine-water complex," *Phys. Chem. Chem. Phys.*, vol. 15, no. 16, pp. 5957–5966, 2013.

[90] X. Liu, A. L. Sobolewski, and W. Domcke, "Photoinduced oxidation of water in the pyridine-water complex: Comparison of the singlet and triplet photochemistries," *J. Phys. Chem. A*, vol. 118, no. 36, pp. 7788–7795, 2014.

[91] N. Esteves-López, S. Coussan, C. Dedonder-Lardeux, and C. Jouvet, "Photoinduced water splitting in pyridine water clusters," *Phys. Chem. Chem. Phys.*, vol. 18, no. 36, pp. 25637–25644, 2016.

[92] J. Ehrmaier, D. Picconi, T. N. Karsili, and W. Domcke, "Photodissociation dynamics of the pyridinyl radical: Time-dependent quantum wave-packet calculations," *J. Chem. Phys.*, vol. 146, no. 12, p. 124304, 2017.

[93] T. H. Dunning Jr, "Gaussian basis sets for use in correlated molecular calculations. i. the atoms boron through neon and hydrogen," *J. Chem. Phys.*, vol. 90, no. 2, pp. 1007–1023, 1989.

[94] C. Woywod, W. Domcke, A. L. Sobolewski, and H.-J. Werner, "Characterization of the S_1-S_2 conical intersection in pyrazine using ab initio multiconfiguration self-consistent-field and multireference configuration-interaction methods," *J. Chem. Phys.*, vol. 100, no. 2, pp. 1400–1413, 1994.

[95] K. Nandipati, Z. Lan, H. Singh, and S. Mahapatra, "An alternative laser driven photodissociation mechanism of pyrrole via $\pi\sigma^{*1}/S_0$ conical intersection," *J. Chem. Phys.*, vol. 146, no. 21, p. 214304, 2017.

[96] K. Nandipati, A. K. Kanakati, H. Singh, and S. Mahapatra, "Controlled intramolecular h-transfer in malonaldehyde in the electronic ground state mediated through the conical intersection of $^1n\pi^*$ and $^1\pi\pi^*$ excited electronic states," *Phys. Chem. Chem. Phys.*, vol. 21, no. 36, pp. 20018–20030, 2019.

[97] K. Sundermann and R. de Vivie-Riedle, "Extensions to quantum optimal control algorithms and applications to special problems in state selective molecular dynamics," *J. Chem. Phys.*, vol. 110, no. 4, pp. 1896–1904, 1999.

[98] S. P. Shah and S. A. Rice, "A test of the dependence of an optimal control field on the number of molecular degrees of freedom: HCN isomerization," *J. Chem. Phys.*, vol. 113, no. 16, pp. 6536–6541, 2000.

[99] M. Feit, J. Fleck Jr, and A. Steiger, "Solution of the schrödinger equation by a spectral method," *J. Comp. Phys.*, vol. 47, no. 3, pp. 412–433, 1982.

[100] M. Feit and J. Fleck Jr, "Solution of the schrödinger equation by a spectral method ii: Vibrational energy levels of triatomic molecules," *J. Chem. Phys.*, vol. 78, no. 1, pp. 301–308, 1983.

[101] S. Mahapatra and H. Köppel, "Spectra and time-dependent dynamics of H_3 near the conical intersection in the $(2p)^1E$ ground electronic manifold," *J. Chem. Phys.*, vol. 109, no. 5, pp. 1721–1733, 1998.

[102] S. Ghosal and S. Mahapatra, "A quantum wave packet dynamical study of the electronic and spin- orbit coupling effects on the resonances in Cl(2p)+ H_2 scattering," *J. Phys. Chem. A*, vol. 109, no. 8, pp. 1530–1540, 2005.

[103] S. Mahapatra and N. Sathyamurthy, "Negative imaginary potentials in time-dependent quantum molecular scattering," *J. Chem. Soc, Faraday Transactions*, vol. 93, no. 5, pp. 773–779, 1997.

[104] H. Köuppel, W. Domcke, and L. S. Cederbaum, "Multimode molecular dynamics beyond the born-oppenheimer approximation," *Adv. Chem. Phys.*, vol. 57, no. 1, pp. 59–246, 1984.

[105] K. Krishnakumar, "Micro-genetic algorithms for stationary and non-stationary function optimization," in *Intelligent control and adaptive systems*, vol. 1196, pp. 289–296, SPIE, 1990.

[106] C. Xie, J. Ma, X. Zhu, D. R. Yarkony, D. Xie, and H. Guo, "Nonadiabatic tunneling in photodissociation of phenol," *J. Am. Chem. Soc.*, vol. 138, no. 25, pp. 7828–7831, 2016.

[107] R. N. Dixon, T. A. Oliver, and M. N. Ashfold, "Tunnelling under a conical intersection: Application to the product vibrational state distributions in the uv photodissociation of phenols," *J. Chem. Phys.*, vol. 134, no. 19, p. 194303, 2011.

[108] T. Penfold, R. Spesyvtsev, O. Kirkby, R. Minns, D. Parker, H. Fielding, and G. Worth, "Quantum dynamics study of the competing ultrafast intersystem crossing and internal conversion in the "channel 3" region of benzene," *J. Chem. Phys.*, vol. 137, no. 20, p. 204310, 2012.

[109] M. Nix, A. Devine, R. Dixon, and M. Ashfold, "Observation of geometric phase effect induced photodissociation dynamics in phenol," *Chem. Phys. Lett.*, vol. 463, no. 4-6, pp. 305–308, 2008.

[110] V. Vallet, Z. Lan, S. Mahapatra, A. L. Sobolewski, and W. Domcke, "Photochemistry of pyrrole: Time-dependent quantum wave-packet description of the dynamics at the $\pi^1\sigma^*$-S_0 conical intersections," *J. Chem. Phys.*, vol. 123, no. 14, p. 144307, 2005.

[111] R. D. Guerrero, C. A. Arango, and A. Reyes, "Analytical optimal pulse shapes obtained with the aid of genetic algorithms," *J. Chem. Phys.*, vol. 143, no. 12, p. 124108, 2015.

[112] R. Guerrero, C. Arango, and A. Reyes, "Communication: Analytical optimal pulse shapes obtained with the aid of genetic algorithms: Controlling the photoisomerization yield of retinal," *J. Chem. Phys.*, vol. 145, no. 3, p. 031101, 2016.

[113] G. M. Roberts, D. J. Hadden, L. T. Bergendahl, A. M. Wenge, S. J. Harris, T. N. Karsili, M. N. Ashfold, M. J. Paterson, and V. G. Stavros, "Exploring quantum phenomena and vibrational control in nσ^* mediated photochemistry," *Chem. Sci.*, vol. 4, no. 3, pp. 993–1001, 2013.

[114] H. S. You, S. Han, J.-H. Yoon, J. S. Lim, J. Lee, S.-Y. Kim, D.-S. Ahn, J. S. Lim, and S. K. Kim, "Structure and dynamic role of conical intersections in the $\pi\sigma^*$-mediated photodissociation reactions," *Int. Rev. Phys. Chem.*, vol. 34, no. 3, pp. 429–459, 2015.

[115] J. S. Lim and S. K. Kim, "Experimental probing of conical intersection dynamics in the photodissociation of thioanisole," *Nat. Chem.*, vol. 2, no. 8, pp. 627–632, 2010.

[116] C. Li, S. Hou, Z. Wang, and C. Xie, "Nonadiabatic heavy atom tunneling in ^{1}nσ^*-mediated photodissociation of thioanisole," *Phys. Chem. Chem. Phys.*, vol. 25, no. 28, pp. 18797–18807, 2023.

[117] K. C. Woo, D. H. Kang, and S. K. Kim, "Real-time observation of nonadiabatic bifurcation dynamics at a conical intersection," *J. Am. Chem. Soc.*, vol. 139, no. 47, pp. 17152–17158, 2017.

[118] J. S. Lim, H. S. You, S.-Y. Kim, and S. K. Kim, "Experimental observation of nonadiabatic bifurcation dynamics at resonances in the continuum," *Chem. Sci.*, vol. 10, no. 8, pp. 2404–2412, 2019.

[119] S. Han, J. S. Lim, J.-H. Yoon, J. Lee, S.-Y. Kim, and S. K. Kim, "Conical intersection seam and bound resonances embedded in continuum observed in the photodissociation of thioanisole-d_3," *J. Chem. Phys.*, vol. 140, no. 5, p. 054307, 2014.

[120] H. Lee, S.-Y. Kim, and S. K. Kim, "Multidimensional characterization of the conical intersection seam in the normal mode space," *Chem. Sci.*, vol. 11, no. 26, pp. 6856–6861, 2020.

[121] S.-Y. Kim, J. Lee, and S. K. Kim, "Conformer specific nonadiabatic reaction dynamics in the photodissociation of partially deuterated thioanisoles (C_6H_5S-CH_2D and C_6H_5S-CHD_2)," *Phys. Chem. Chem. Phys.*, vol. 19, no. 29, pp. 18902–18912, 2017.

[122] Y. Shu and D. G. Truhlar, "Improved potential energy surfaces of thioanisole and the effect of upper surface variations on the product distribution upon photodissociation," *Chem. Phys.*, vol. 515, pp. 737–743, 2018.

[123] Z. Xu, S. Hou, Z. Wang, and C. Xie, "Neural network potentials facilitating accurate complex scaling for molecular resonances: from a model to high dimensional realistic systems," *Phys. Chem. Chem. Phys.*, vol. 26, no. 32, pp. 21861–21873, 2024.

[124] U. Manthe and H. Köppel, "New method for calculating wave packet dynamics: Strongly coupled surfaces and the adiabatic basis," *J. chem. phys.*, vol. 93, no. 1, pp. 345–356, 1990.

[125] U. Manthe and H. Köppel, "Dynamics on potential energy surfaces with a conical intersection: Adiabatic, intermediate, and diabatic behavior," *J. chem. phys.*, vol. 93, no. 3, pp. 1658–1669, 1990.

[126] S. Shi and H. Rabitz, "Quantum mechanical optimal control of physical observables in microsystems," *J. chem. phys.*, vol. 92, no. 1, pp. 364–376, 1990.

[127] J. Somlói, V. A. Kazakov, and D. J. Tannor, "Controlled dissociation of I_2 via optical transitions between the X and B electronic states," *Chem. phys.*, vol. 172, no. 1, pp. 85–98, 1993.

[128] W. Zhu, J. Botina, and H. Rabitz, "Rapidly convergent iteration methods for quantum optimal control of population," *J. Chem. Phys.*, vol. 108, no. 5, pp. 1953–1963, 1998.

[129] P. Nuernberger, G. Vogt, T. Brixner, and G. Gerber, "Femtosecond quantum control of molecular dynamics in the condensed phase," *Phys. Chem. Chem. Phys.*, vol. 9, no. 20, pp. 2470–2497, 2007.

[130] R. T. Skodje, R. Sadeghi, H. Köppel, and J. L. Krause, "Spectral quantization of transition state dynamics for the three-dimensional H + H_2 reaction," *J. Chem. Phys.*, vol. 101, no. 2, pp. 1725–1729, 1994.

[131] C. Gellini, L. Moroni, and M. Muniz-Miranda, "High overtones of the C-H stretching vibrations in anisole and thioanisole," *J. Phys. Chem. A*, vol. 106, no. 46, pp. 10999–11007, 2002.

[132] R. Baer, D. M. Charutz, R. Kosloff, and M. Baer, "A study of conical intersection effects on scattering processes: The validity of adiabatic single-surface approximations within a quasi-Jahn-Teller model," *J. Chem. Phys.*, vol. 105, no. 20, pp. 9141–9152, 1996.

[133] A. Sobolewski, "On the excess-energy dependence of radiationless decay rate constants," *Chem. Phys.*, vol. 115, no. 3, pp. 469–479, 1987.

[134] M. Abe, Y. Ohtsuki, Y. Fujimura, Z. Lan, and W. Domcke, "Geometric phase effects in the coherent control of the branching ratio of photodissociation products of phenol," *J. chem. phys.*, vol. 124, no. 22, p. 224316, 2006.

[135] S. Rice and M. Zhao, *Optical Control of Molecular Dynamics*. Wiley, 2000.

[136] M. Shapiro and P. Brumer, *Principles of the Quantum Control of Molecular Processes*. Wiley, 2003.

[137] C. Brif, R. Chakrabarti, and H. Rabitz, "Control of quantum phenomena: past, present and future," *New J. Phys.*, vol. 12, no. 7, p. 075008, 2010.

[138] J. Werschnik and E. Gross, "Quantum optimal control theory," *J. Phys. B*, vol. 40, no. 18, p. R175, 2007.

[139] D. Tannor, *Introduction to Quantum Mechanics*. University Science Books, 2007.

[140] M. Shapiro and P. Brumer, "On the origin of pulse shaping control of molecular dynamics," *J. Phys. Chem. A*, vol. 105, no. 12, pp. 2897–2902, 2001.

[141] N. E. Henriksen, "Theoretical concepts in molecular photodissociation dynamics," *Adv. Chem. Phys., Vol 91*, vol. 91, pp. 433–509, 2007.

[142] J. L. Krause, R. M. Whitnell, K. R. Wilson, Y. Yan, and S. Mukamel, "Optical control of molecular dynamics: Molecular cannons, reflectrons, and wave-packet focusers," *J. Chem. Phys.*, vol. 99, no. 9, pp. 6562–6578, 1993.

[143] A. K. Tiwari, K. B. Møller, and N. E. Henriksen, "Controlling the spreading of wave packets of a dissociating molecule," *Chem. Phys. Lett.*, vol. 450, no. 1-3, pp. 6–11, 2007.

[144] C.-C. Shu and N. E. Henriksen, "Coherent control of indirect photofragmentation in the weak-field limit: Control of transient fragment distributions," *J. Chem. Phys.*, vol. 134, no. 16, 2011.

[145] C.-C. Shu and N. E. Henriksen, "Phase-only shaped laser pulses in optimal control theory: Application to indirect photofragmentation dynamics in the weak-field limit," *J. Chem. Phys.*, vol. 136, no. 4, 2012.

[146] R. Emerson and W. Arnold, "The photochemical reaction in photosynthesis," *J. Gen. Physiol.*, vol. 16, no. 2, pp. 191–205, 1932.

[147] D. Polli, P. Altoè, O. Weingart, K. M. Spillane, C. Manzoni, D. Brida, G. Tomasello, G. Orlandi, P. Kukura, R. A. Mathies, *et al.*, "Conical intersection dynamics of the primary photoisomerization event in vision," *Nature*, vol. 467, no. 7314, pp. 440–443, 2010.

[148] T. J. Kucharski, Y. Tian, S. Akbulatov, and R. Boulatov, "Chemical solutions for the closed-cycle storage of solar energy," *Energy Environ. Sci.*, vol. 4, no. 11, pp. 4449–4472, 2011.

[149] R. P. Sinha and D.-P. Häder, "UV-induced DNA damage and repair: a review," *Photochem. Photobiol. Sci.*, vol. 1, no. 4, pp. 225–236, 2002.

[150] B. Zietz, E. Gabrielsson, V. Johansson, A. M. El-Zohry, L. Sun, and L. Kloo, "Photoisomerization of the cyanoacrylic acid acceptor group-a potential problem for organic dyes in solar cells," *Phys. Chem. Chem. Phys.*, vol. 16, no. 6, pp. 2251–2255, 2014.

[151] H. Rabitz, R. de Vivie-Riedle, M. Motzkus, and K. Kompa, "Whither the future of controlling quantum phenomena?," *Science*, vol. 288, no. 5467, pp. 824–828, 2000.

[152] P. von den Hoff, S. Thallmair, M. Kowalewski, R. Siemering, and R. de Vivie-Riedle, "Optimal control theory-closing the gap between theory and experiment," *Phys. Chem. Chem. Phys.*, vol. 14, no. 42, pp. 14460–14485, 2012.

[153] J. Galego, F. J. Garcia-Vidal, and J. Feist, "Suppressing photochemical reactions with quantized light fields," *Nat. Comm.*, vol. 7, no. 1, p. 13841, 2016.

[154] M. Gudem and M. Kowalewski, "Controlling the photostability of pyrrole with optical nanocavities," *J. Phys. Chem. A*, vol. 125, no. 5, pp. 1142–1151, 2021.

[155] E. Barton Cole, P. S. Lakkaraju, D. M. Rampulla, A. J. Morris, E. Abelev, and A. B. Bocarsly, "Using a one-electron shuttle for the multielectron reduction of CO_2 to methanol: kinetic, mechanistic, and structural insights," *J. Am. Chem. Soc.*, vol. 132, no. 33, pp. 11539–11551, 2010.

[156] Y. Yan, E. L. Zeitler, J. Gu, Y. Hu, and A. B. Bocarsly, "Electrochemistry of aqueous pyridinium: exploration of a key aspect of electrocatalytic reduction of CO_2 to methanol," *J. Am. Chem. Soc.*, vol. 135, no. 38, pp. 14020–14023, 2013.

[157] J. A. Keith and E. A. Carter, "Electrochemical reactivities of pyridinium in solution: consequences for CO_2 reduction mechanisms," *Chem. Sci.*, vol. 4, no. 4, pp. 1490–1496, 2013.

[158] M. Z. Ertem, S. J. Konezny, C. M. Araujo, and V. S. Batista, "Functional role of pyridinium during aqueous electrochemical reduction of CO_2 on Pt(111)," *J. Phys. Chem. Lett.*, vol. 4, no. 5, pp. 745–748, 2013.

[159] F. Riboni, E. Selli, M. Hoffmann, and A. Colussi, "Homogeneous reduction of CO_2 by photogenerated pyridinyl radicals," *J. Phys. Chem. A*, vol. 119, no. 19, pp. 4433–4438, 2015.

[160] M. Alamgir and S. Mahapatra, "Optimal control of N-H photodissociation of pyridinyl," *J. Chem. Phys.*, vol. 160, no. 7, 2024.

[161] R. Uberna, M. Khalil, R. M. Williams, J. M. Papanikolas, and S. R. Leone, "Phase and amplitude control in the formation and detection of rotational wave packets in the $E^1\Sigma_g^+$ state of LI_2," *J. Chem. Phys.*, vol. 108, no. 22, pp. 9259–9274, 1998.

[162] B. Kohler, J. L. Krause, F. Raksi, K. R. Wilson, V. V. Yakovlev, R. M. Whitnell, and Y. Yan, "Controlling the future of matter," *Acc. Chem. Res.*, vol. 28, no. 3, pp. 133–140, 1995.

[163] J. Cao and K. R. Wilson, "A simple physical picture for quantum control of wave packet localization," *J. chem. phys.*, vol. 107, no. 5, pp. 1441–1450, 1997.

[164] R. Bhattacharya, S. Chatterjee, and S. Bhattacharyya, "Preparation and probing of coherent vibrational wave packets in the ground electronic state of HD^+," *Phys. Rev. A*, vol. 85, no. 3, p. 033424, 2012.

Publications

1. **Md Alamgir** and S. Mahapatra*, "Optimal Control of N-H Photodissociation of Pyridinyl", J. Chem. Phys. **160**, 074303 (2024).(Chapter 3 in this thesis)

2. **Md Alamgir** and S. Mahapatra*, "Control of optically dark nσ^* state mediated photodissociation of thioanisole", J. Chem. Phys. **162**, 154303 (2025).(Chapter 4 in this thesis)

3. **Md Alamgir**, Mamilwar Rani, and S. Mahapatra*, "Laser driven S-CH_3 photodissociation dynamics of thioanisole on a new potential energy surface†". (*Under Review*)

4. **Md Alamgir** and S. Mahapatra*, "Suppression of N-H photodissociation of pyridinyl radical implementing frequency chirping: Utilization of coherent superposition principle". (*manuscript under preparation*) (Chapter 5 in this thesis)

5. **Md Alamgir** and S. Mahapatra*, "Control of nonadiabatic dynamics via cavity induced conical intersection in the influence of optimal laser pulse". (*manuscript under preparation*)

6. Ajay Mohan Singh Rawat, **Md Alamgir**, Sugata Goswami and S. Mahapatra*, "A new ground electronic state potential energy surface of $HeLiH^+$: Analytical representation and investigation of the dynamics of He + LiH^+ (v=*0*, j=0) $\rightarrow$ $LiHe^+$ + H reaction", J. Chem. Phys. **161**, 124308 (2024).

7. Debu Jana, **Md Alamgir**, Samar K Das*, "Synergy of $Co(H_2O)_6{}^{2+}$ with a Polyoxometalate Leads to Aqueous Homogeneous Hydrogen Evolution: Experiments and Computations", Inorg. Chem. **63**, 13959–13971 (2024).

8. Suman Mondal, Smruti Prangya Behera, **Md Alamgir** and Viswanathan Baskar*, "In Situ Assembled Polynuclear Zinc Oxo Clusters Using Modified Schiff Bases as Ligands", ACS Omega **7**, 1090 (2022).

Conferences attended

1. Poster presentation in 'DAE Symposium on Current Trends in Theoretical Chemistry (CTTC-2020)', Sep 2021, BARC, Mumbai, India

2. Poster presentation in '17th Theoretical Chemistry Symposium (TCS-2021)', Dec 2021, IISER Kolkata, India

3. Oral presentation in '21th Annual In-House Symposium CHEMFEST-2024'.

4. Poster presentation in 'QUANTUM SYSTEMS IN CHEMISTRY, PHYSICS, AND BIOLOGY (QSCP-XXVI)', Oct 2023, Ashoka University, India

5. Poster presentation in '18th Theoretical Chemistry Symposium (TCS-2023)', Nov 2023, IIT Madras, India

Quantum Dynamics of Molecules with Laser as a Catalyst

by Md Alamgir

Submission date: 18-Jun-2025 04:51PM (UTC+0530)
Submission ID: 2701667290
File name: Md_Alamgir.pdf (6.22M)
Word count: 30995
Character count: 153136

Quantum Dynamics of Molecules with Laser as a Catalyst

ORIGINALITY REPORT

27%	7%	25%	3%
SIMILARITY INDEX	INTERNET SOURCES	PUBLICATIONS	STUDENT PAPERS

PRIMARY SOURCES

1	Mohammed Alamgir, Susanta Mahapatra. "Optimal control of N–H photodissociation of pyridinyl", The Journal of Chemical Physics, 2024 Publication	19%
2	mediatum.ub.tum.de Internet Source	1%
3	chemistry.uohyd.ac.in Internet Source	1%
4	Submitted to University of Hyderabad, Hyderabad Student Paper	1%
5	Sitansh Sharma, Harjinder Singh, Gabriel G. Balint-Kurti. "Genetic algorithm optimization of laser pulses for molecular quantum state excitation", The Journal of Chemical Physics, 2010 Publication	<1%
6	Johannes Ehrmaier, David Picconi, Tolga N. V. Karsili, Wolfgang Domcke. "Photodissociation dynamics of the pyridinyl radical: Time-dependent quantum wave-packet calculations", The Journal of Chemical Physics, 2017 Publication	<1%
7	Submitted to Indian Institute of Technology, Madras Student Paper	<1%

→ from our own paper

Susanta Mahapatra

Susanta Mahapatra
Senior Professor
School of Chemistry
University of Hyderabad
Hyderabad-500046, TS, Ind

8	K. R. Nandipati, Z. Lan, H. Singh, S. Mahapatra. "An alternative laser driven photodissociation mechanism of pyrrole via πσ*1/S0 conical intersection", The Journal of Chemical Physics, 2017 Publication	<1 %
9	Submitted to National University of Singapore Student Paper	<1 %
10	Submitted to University of Strathclyde Student Paper	<1 %
11	"Springer Handbook of Atomic, Molecular, and Optical Physics", Springer Science and Business Media LLC, 2006 Publication	<1 %
12	aip.scitation.org Internet Source	<1 %
13	Zhenggang Lan, Wolfgang Domcke, Valérie Vallet, Andrzej L. Sobolewski, Susanta Mahapatra. "Time-dependent quantum wave-packet description of the π1σ* photochemistry of phenol", The Journal of Chemical Physics, 2005 Publication	<1 %
14	d-nb.info Internet Source	<1 %
15	Valérie Vallet, Zhenggang Lan, Susanta Mahapatra, Andrzej L. Sobolewski, Wolfgang Domcke. "Photochemistry of pyrrole: Time-dependent quantum wave-packet description of the dynamics at the π1σ*-S0 conical intersections", The Journal of Chemical Physics, 2005 Publication	<1 %
16	api-depositonce.tu-berlin.de Internet Source	<1 %

17	Zhenggang Lan. "Time-dependent quantum wave-packet description of the [sup 1]πσ[sup", The Journal of Chemical Physics, 2005 Publication	<1 %
18	S. Mahapatra, N. Sathyamurthy. "Resonances in He + H2+→HeH+ + H reaction in three-dimensions: Energy resolved total reaction probabilities by the time-dependent wave packet method", The Journal of Chemical Physics, 1997 Publication	<1 %
19	Xie, Changjian, Jianyi Ma, Xiaolei Zhu, David R. Yarkony, Daiqian Xie, and Hua Guo. "Nonadiabatic Tunneling in Photodissociation of Phenol", Journal of the American Chemical Society Publication	<1 %
20	Submitted to University of Wollongong Student Paper	<1 %
21	Submitted to Queen's University of Belfast Student Paper	<1 %
22	Submitted to University of Newcastle Student Paper	<1 %
23	home.iitk.ac.in Internet Source	<1 %
24	Yinan Shu, Donald G. Truhlar. "Improved potential energy surfaces of thioanisole and the effect of upper surface variations on the product distribution upon photodissociation", Chemical Physics, 2018 Publication	<1 %
25	vdoc.pub Internet Source	<1 %

26	Vander Wal, R. L., J. L. Scott, and F. F. Crim. "Selectively breaking the Oâ€“H bond in HOD", The Journal of Chemical Physics, 1990. Publication	<1 %
27	core.ac.uk Internet Source	<1 %
28	pubs.rsc.org Internet Source	<1 %
29	Marcos Dantus, Vadim V. Lozovoy. "Experimental Coherent Laser Control of Physicochemical Processes", Chemical Reviews, 2004 Publication	<1 %
30	Thomas J. Penfold, Etienne Gindensperger, Chantal Daniel, Christel M. Marian. "Spin-Vibronic Mechanism for Intersystem Crossing", Chemical Reviews, 2018 Publication	<1 %
31	Bijit Mukherjee, Sandip Ghosh, Satrajit Adhikari. "Beyond Born-Oppenheimer treatment on spectroscopic and scattering processes", Journal of Physics: Conference Series, 2018 Publication	<1 %
32	Submitted to The University of Manchester Student Paper	<1 %
33	"Elucidating the Fundamental Interactions of Very Small ParticlesUltrafast Science", Developments in Surface Contamination and Cleaning, 2008 Publication	<1 %
34	Guang-Shuang-Mu Lin, Changjian Xie, Daiqian Xie. " Nonadiabatic Effect in Photodissociation Dynamics of Thiophenol via the ππ* State ", The Journal of Physical Chemistry A, 2018	<1 %

	Publication	
35	refubium.fu-berlin.de Internet Source	<1 %
36	Roman F. Nalewajski. "Perspectives in Electronic Structure Theory", Springer Science and Business Media LLC, 2012 Publication	<1 %
37	dspace.uevora.pt Internet Source	<1 %
38	idoc.pub Internet Source	<1 %
39	lirias.kuleuven.be Internet Source	<1 %
40	Submitted to De Montfort University Student Paper	<1 %
41	K. R. Nandipati, Arun Kumar Kanakati, H. Singh, S. Mahapatra. " Controlled intramolecular H-transfer in malonaldehyde in the electronic ground state mediated through the conical intersection of nπ* and ππ* excited electronic states ", Physical Chemistry Chemical Physics, 2019 Publication	<1 %
42	Vlasta Bonačić-Koutecký. "Complex systems in the gas phase", Chemical physics, 2007 Publication	<1 %
43	Submitted to Atilim University Student Paper	<1 %
44	Langhojer, Florian. "New techniques in liquid-phase ultrafast spectroscopy", Universität Würzburg, 2012. Publication	<1 %
45	Li Fei. "Atomic population oscillations between two coupled Bose–Einstein	<1 %

condensates with time-dependent nonlinear interaction", Chinese Physics, 03/2007
Publication

46	Mark E. Thompson. "Electrophosphorescent Materials and Devices", Jenny Stanford Publishing, 2023 Publication	<1%
47	journal-spqeo.org.ua Internet Source	<1%

Exclude quotes	On	Exclude matches	< 14 words
Exclude bibliography	On		